Formation and Stability of Spheromak/Field Reversed Configuration (FRC) Hybrids in SSX-FRC

Andrew Fefferman
Swarthmore College
Department of Physics and Astronomy

March 31, 2003

Abstract

Axisymmetric plasma configurations which might be used for fusion reactors include tokamaks, spheromaks and field reversed configurations (FRC). The FRC has some advantages over tokamaks and spheromaks, including a high $\beta \equiv \frac{2\mu_0 P}{B^2}$. However, compared to tokamaks and spheromaks, relatively little is known about high β configurations like FRC's. This paper is based on a study of a high β spheromak/FRC hybrid configuration in SSX-FRC. The author constructed magnetic probes to measure all three components of the magnetic field vector at 96 locations throughout the hybrid. Measuring the structure of the magnetic field embedded in the plasma is a good way of characterizing the hybrid equilibrium and diagnosing its stability. The magnetics measurements are compared with theory and numerical simulations of axisymmetric toroidal equilibria. In brief, it was found that the hybrid configuration is stable for several characteristic times before tilting. The tilt instability was not observed in studies of counterhelicity spheromak merging by Ono *et al* [12, 13]. Furthermore, the anti-parallel toroidal fields of the counterhelicity spheromaks in SSX-FRC never completely annihilate, in contrast with the results of Ono *et al* [12, 13]. However, the persistence of the toroidal field structure is consistent with the simulation results by Omelchenko [32, 33]. The hybrid configuration is not consistent with the general axisymmetric plasma equilibrium (the Grad-Shafranov equilibrium) due to currents that flow across flux surfaces. Controlling the extent to which the spheromaks reconnect with midplane field coils external to the plasma does not have a significant effect on the stability of the plasma configuration.

Contents

List of Figures

1 Introduction

In the quest to develop a practical fusion energy source, several different magnetic confinement plasma configurations have been explored. The conventional configuration is the tokamak (Fig. 1), which is a toroidal plasma linked by coils that produce a toroidal magnetic field (also called toroidal magnetic field coils or B_ϕ coils). The tokamak is characterized by a low β which is the ratio of kinetic pressure to magnetic pressure,

$$\beta \equiv \frac{2\mu_0 P}{B^2}. \tag{1}$$

Beta is a parameter that characterizes the efficiency of the magnetic confinement of the plasma. Ideally, beta would be unity so that the magnetic pressure just balances the kinetic plasma pressure and excessive resources are not expended on maintaining a high magnetic field to confine the plasma. The tokamak has attained the most impressive plasma parameters of all the fusion configurations, but tokamaks may be excessively expensive for a practical fusion reactor. One alternative concept is the spheromak (Fig. 2), which is also a low beta toroidal configuration ($\beta \approx 0.01$ to 0.2) [2]. The spheromak has both toroidal and poloidal magnetic fields, which are defined in Fig. 2. The spheromak in Fig. 2 is left-handed due to the geometric relationship between the toroidal and poloidal magnetic fields. Unlike the tokamak, the spheromak is simply connected: there is no solid structure linking the spheromak torus. The spheromak has some advantages over the tokamak, but it is still characterized by a low beta. Another alternative concept is the FRC (Fig. 3), which is a simply connected toroidal configuration with a high beta ($\beta \approx 1$). The lack of a toroidal field component in the FRC contributes to its high value for β. FRC's are attractive candidates for a practical fusion configuration, but little is known about them compared to tokamaks and FRC's. Specifically, the stability of FRC's is uncertain, especially in the MHD regime [44].

An MHD hybrid plasma configuration that shares some characteristics of spheromaks and some characteristics of FRC's has been created in SSX-FRC by merging two counterhelicity spheromaks. Counter-helicity means that the magnetic field lines of the two spheromaks have opposite handedness. The mathematical definition of helicity is given in a later section in Eq. 119. The study was motivated by results of a numerical simulation by Omelchenko [32, 33] that suggested that oppositely directed bundles of toroidal field could add to the stability of a hybrid. In SSX-FRC, one would expect that the two counterhelicity spheromaks would merge and the antiparallel toroidal flux of the two spheromaks would annihilate completely. Therefore, a "reconnection control coil" is used to magnetically limit the extent to which the two counterhelicity spheromaks reconnect, thereby determining the amount of anti-parallel toroidal magnetic field remaining in the hybrid configuration. The effect of anti-parallel toroidal field on the stability of the hybrid can thus be ascertained. In contrast with previous experimental studies of plasmas created by the merger of two counterhelicity spheromaks undertaken by Ono et al, the final plasma configuration is uninhibited by a central conductor so that the tilt instability of the hybrid can be investigated [12, 13].

The investigation of the spheromak/FRC hybrid on SSX-FRC is a program involving experimental measurements using several different diagnostics, including magnetic probes, soft x-ray detectors, a mach probe, and an interferometer. This paper is based on measurements of all components of the magnetic field vector at 96 locations throughout the hybrid. Measuring the structure of the magnetic field embedded in the plasma is a good way of characterizing the hybrid equilibrium and diagnosing its stability. The magnetics measurements are compared with theory and numerical simulations of axisymmetric toroidal equilibria. In brief, it was found that merging two counterhelicity spheromaks results in a hybrid configuration without a toroidal magnetic field in the central region (consistent with an FRC), but with oppositely directed toroidal magnetic fields at either end

Figure 1: The tokamak (above) is the fusion plasma device which has attained the most impressive plasma parameters. Figure taken from Contemporary Physics Education Project (CPEP) "Fusion" poster.

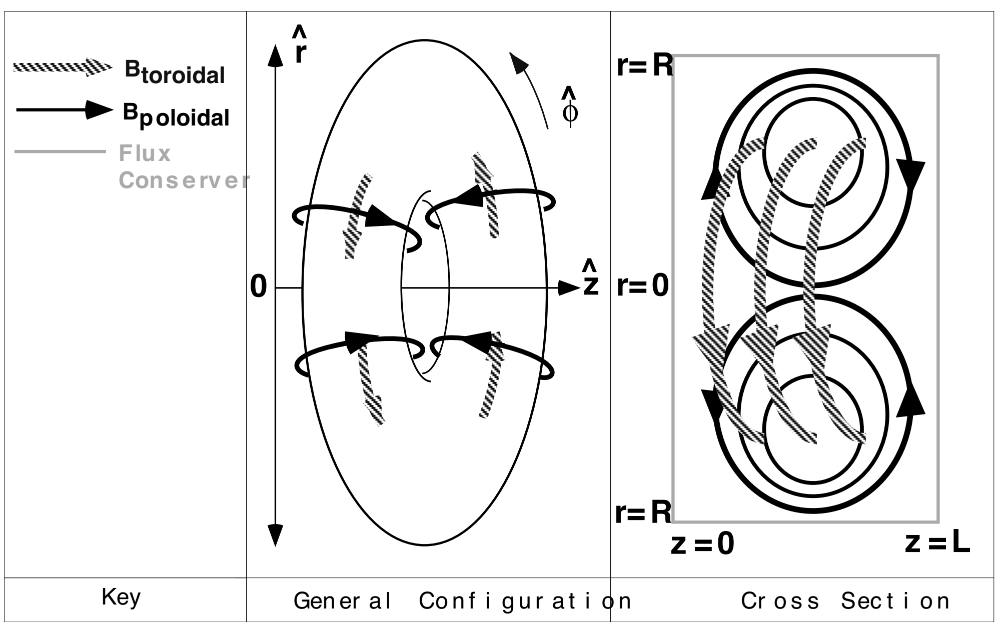

Figure 2: The spheromak is a low beta compact torus plasma configuration. It has both toroidal and poloidal magnetic field components.

of the hybrid (consistent with the spheromak origins of the hybrid). The hybrid configuration is not consistent with the general axisymmetric plasma equilibrium (the Grad-Shafranov equilibrium) because radial currents flowing across flux surfaces at the midplane are implied by the anti-parallel toroidal fields. The hybrid configuration is stable for several characteristic times before tilting (the tilt instability is discussed in the section on MHD instabilities.) The tilted hybrid is consistent with a tilted CT. Controlling the extent to which the spheromaks reconnect with the reconnection control coils does not have a significant effect on the stability of the plasma configuration.

The paper is organized as follows. The plasmas produced in SSX-FRC, as well as most potential fusion plasmas, are in the magnetohydrodynamic (MHD) regime. Therefore, the paper begins with a discussion of the principles of MHD. It continues with a discussion of the simplest one- and two-dimensional MHD equilibria. The specific equilibria involved in SSX-FRC (spheromaks and FRC's) are then discussed. MHD equilibria are prone to different kinds of instabilities. Since part of the purpose of this experiment was to characterize the stability of the configuration generated by merging two counter-helicity spheromaks, the kink and tilt MHD instabilities are discussed. Following this exposition of background information, the SSX-FRC experiment itself is discussed. Discussions of theoretical motivation, experimental setup and results are included. Finally, a conclusion and summary of the paper is presented.

2 Magnetohydrodynamics (MHD)

The plasmas produced in SSX-FRC and fusion plasmas are magnetohydrodynamic (MHD) plasmas. This means that such plasmas can be approximated as single fluids without losing too much of the physics. In principle, one could track the trajectory of each of the myriad particles in a plasma. However, this would be an impossible task due to the sheer number of particles and the self-consistent nature of the problem. The problem is self-consistent in that electromagnetic fields determine particle trajectories and the trajectories of the particles in turn create the fields, along with any externally imposed fields. Therefore, one must resort to an approximation when dealing with real plasmas, and the MHD approximation is the crudest of the fluid approximations, although it works surprisingly well.

Some intuition can be gained from considering single particle motion. The trajectory of a charged particle in an electromagnetic field is relatively easy to compute from the Lorentz force law

$$\vec{F} = q(\vec{E} + \vec{v} \times \vec{B}) \tag{2}$$

and (assuming non-relativistic velocities) Newton's second law

$$\vec{F} = m\vec{a}. \tag{3}$$

For instance, a charged particle moving in a region of uniform magnetic field simply executes a helical orbit about a magnetic field line since the force due to the magnetic field is perpendicular to both the field and the velocity of the particle (Fig. 4.)

Although the motion of charged particles in electromagnetic fields is well-understood, the single particle model is not sufficient to describe a plasma since we have neglected the interaction between the particles and the character of the bulk plasma, which includes features such as a diamagnetic current. A more realistic, yet still approximate, model of a plasma is magnetohydrodynamics (MHD). In this model, the plasma is treated as a conducting fluid, individual particle motion is neglected, and the plasma is neutral. In ideal MHD, there is no resistivity.

Fusion plasmas discussed in the previous section have a relatively high density (10^{13}–$10^{15} cm^{-3}$), so they can be modeled as fluids according to MHD. As in the case of ordinary fluids (hydrodynamics) there is a force per unit volume on a plasma given by $-\nabla p$. In a magnetically confined

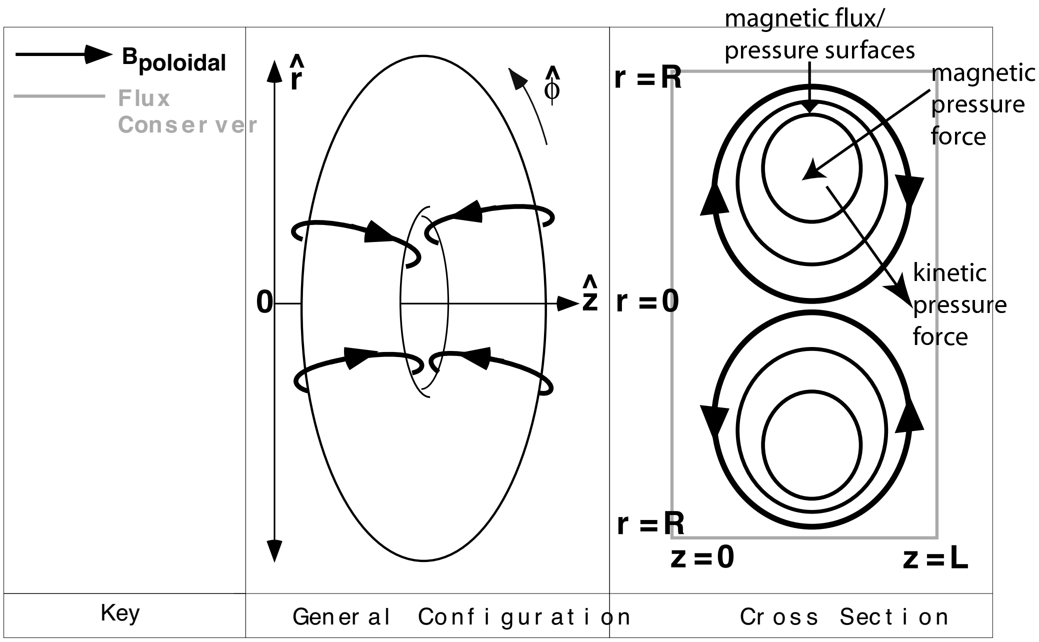

Figure 3: The FRC is a high beta compact torus plasma configuration. It has no toroidal magnetic field component.

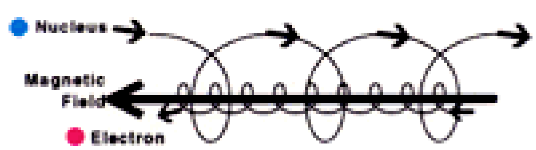

Figure 4: A charged particle executes a helical orbit about a magnetic field line. Figure taken from the Princeton Plasma Physics Laboratory web site.

plasma such as a tokamak plasma, the temperature and density are higher in the center of the toroidal plasma. Since pressure is proportional to temperature and density (in the ideal gas approximation) the pressure of a tokamak plasma decreases as distance from the center of the torus increases. Therefore, there is an outward force on the plasma due to the inward gradient in pressure. "Pressure surfaces" are surfaces of constant pressure, which, by definition, are perpendicular to the pressure gradient. In the case of the tokamak plasma, these surfaces are nested toroidal surfaces. The poloidal magnetic flux is defined by

$$\psi \equiv \int_0^r 2\pi r B_z dr \tag{4}$$

Surfaces of constant flux, or "flux surfaces" are the contours of the poloidal magnetic flux function. These contours are identical to pressure surfaces. The pressure and flux contours as well as the forces due to magnetic and plasma pressure gradients are labeled in Fig. 3.

The magnetic field of a magnetically confined plasma can be described with field lines and flux surfaces. Field lines are everywhere parallel to the magnetic field. They are given by the solution to

$$\frac{d\vec{r}}{dl} = \frac{\vec{B}}{|\vec{B}|}. \tag{5}$$

where dl is a differential element of length along the magnetic field line. The equation of motion for a plasma is determined by Newton's second law:

$$\vec{F} = m\vec{a}. \tag{6}$$

In the MHD approximation Eq. 6 becomes

$$-\nabla p + \vec{J} \times \vec{B} = \rho \frac{d\vec{v}}{dt}. \tag{7}$$

Here $\vec{v}$ is the local velocity of the magnetofluid. Since the plasma is a continuous system, the quantities $\vec{F}$ and m in Eq. 6 are interpreted as densities in Eq. 7. In plasma equilibrium, there is no magnetofluid flow, which implies that $\frac{d\vec{v}}{dt} = 0$. Therefore, Eq. 7 becomes

$$\nabla p = \vec{J} \times \vec{B}. \tag{8}$$

Dotting both sides with $\vec{B}$ yields

$$\vec{B} \cdot \nabla p = \vec{B} \cdot \vec{J} \times \vec{B} = 0. \tag{9}$$

since $\vec{J} \times \vec{B} \perp \vec{B}$. Therefore, magnetic field lines are perpendicular to the gradient in pressure and parallel to pressure surfaces. Magnetic field lines are said to lie in pressure surfaces or, equivalently, magnetic flux surfaces.

It can also be shown that in an ideal (resistanceless) MHD plasma, magnetic flux is conserved and magnetic field lines are "frozen in" to the plasma. First an expression for the current density in a conducting fluid is needed. In a frame of reference moving with the plasma,

$$\vec{J'} = \sigma \vec{E'}. \tag{10}$$

Special relativity indicates that

$$\vec{E'} = \vec{E} + \vec{v} \times \vec{B} \tag{11}$$

$$\vec{J'} = \vec{J} + O(\frac{v}{c}^2). \tag{12}$$

Therefore,

$$\vec{J} \approx \sigma(\vec{E} + \vec{v} \times \vec{B}). \tag{13}$$

In a resistanceless plasma, $\sigma \to \infty$ so to keep $\vec{J}$ finite

$$\vec{E} + \vec{v} \times \vec{B} = 0. \tag{14}$$

Substituting this equation into Faraday's law

$$\frac{\partial \vec{B}}{\partial t} = -\nabla \times \vec{E} \tag{15}$$

yields

$$\frac{\partial \vec{B}}{\partial t} = \nabla \times (\vec{v} \times \vec{B}) \tag{16}$$

which is the magnetic induction equation for an ideal MHD plasma [10].

The magnetic induction equation can be used to prove flux conservation. The following derivation is after Sturrock, 1994 [41]. Consider a contour c embedded in a plasma so that each point on the contour moves with the plasma's velocity $v(\vec{x}, t)$ (Fig. 5). After a time δt, c maps onto c'. The magnetic flux through the surface S bounded by c is given by

$$\phi(S, t) = \int_S dS \vec{B}(\vec{x}, t) \cdot \hat{n}. \tag{17}$$

The flux through the surface S' bounded by c' is given by

$$\phi(S', t') = \int_{S'} dS \vec{B}(\vec{x}, t') \cdot \hat{n} \approx \int_{S'} dS \vec{B}(\vec{x}, t) \cdot \hat{n} + \int_S dS \frac{\partial \vec{B}}{\partial t} \delta t \cdot \hat{n}. \tag{18}$$

The error introduced by integrating the second term in the previous equation over S rather than S' is second order in δt and therefore negligible. The magnetic flux through the surface S_a that connects c and c' is given by

$$\phi(S_a, t) = \oint_c (d\vec{l} \times \vec{V} \delta t) \cdot \vec{B}. \tag{19}$$

Since all magnetic fields are divergenceless, the surface chosen in Eq. (17) to evaluate the flux linked by c was not unique. It is also true that

$$\phi(S, t) = \phi(S', t) + \phi(S_a, t) \tag{20}$$

$$= \int_{S'} dS \vec{B}(\vec{x}, t) \cdot \hat{n} + \oint_c (d\vec{l} \times \vec{v} \delta t) \cdot \vec{B}. \tag{21}$$

Subtracting (18) from (21) yields

$$\phi(S', t') - \phi(S, t) = \int_S dS \frac{\partial \vec{B}}{\partial t} \delta t \cdot \hat{n} - \oint_c (d\vec{l} \times \vec{V} \delta t) \cdot \vec{B}. \tag{22}$$

Taking the limit as δt goes to zero yields

$$\frac{\partial \phi}{\partial t} = \int_S dS \frac{\partial \vec{B}}{\partial t} \cdot \hat{n} - \oint_c (d\vec{l} \times \vec{V}) \cdot \vec{B}. \tag{23}$$

Applying the vector identity $(\vec{A}\times\vec{B})\cdot\vec{C} = (\vec{B}\times\vec{C})\cdot\vec{A}$ and Stokes' theorem to the previous equation yields

$$\frac{\partial\phi}{\partial t} = \int_S dS(\frac{\partial\vec{B}}{\partial t} - \nabla\times(\vec{v}\times\vec{B}))\cdot\hat{n} = 0. \tag{24}$$

where we have used the magnetic induction equation (16). Eq. 24 indicates that flux is conserved in an ideal MHD plasma.

Flux conservation can be used to show that magnetic field lines are frozen into the plasma. Consider the tube surrounding a field line shown in Fig. 6a. The tube is arbitrarily close to the field line so that no other field lines pierce the tube. Fig. 6b shows the tube surrounding the field line after a time lapse. The tube moves with the plasma just as the contour c in the previous discussion did. There is initially no flux through the walls of the tube so there cannot be any flux through the walls at subsequent times. The finite flux through the ends of the tubes is also conserved. Therefore, the field lines are frozen into the plasma flow and vice versa in the ideal MHD model. The field lines also cannot be broken in the MHD model. Note that if the plasma is compressed at the ends of the tubes, the area of the ends of the tubes decreases, so the strength of the magnetic field normal to the ends must increase to conserve the flux.

MHD applies only to plasmas that can be considered to be continuous fluids, which means that the ion cyclotron radius, or Larmor radius, must be much less than the characteristic length of the plasma. The applicability of MHD to a plasma is determined by

$$s = \text{number of gyroradii between field null and separatrix} \tag{25}$$

or by

$$\bar{s} \equiv \int_R^{r_s} \frac{rdr}{r_s\rho_i}, \tag{26}$$

if more quantitative precision is desired. R and r_s are the magnetic null and the separatrix radius at the midplane, and ρ_i is the local thermal ion Larmor radius [3]. A net-power fusion plasma requires an s value of at least a few tens. Therefore, fusion plasmas are well characterized by MHD.

3 1-D MHD Equilibrium: Bennett Pinch

The first step towards magnetically confining a hot plasma entails finding stable equilibrium states of plasmas. A simple (unstable) equilibrium state of a plasma is called the Bennett Pinch [4], or z-pinch, where z is the direction of the current. It is useful to consider this equilibrium state because it is a simplified version of the two-dimensional axisymmetric equilibrium considered below. The hybrid plasma configuration created in SSX-FRC is largely axisymmetric. Consider an infinite cylinder of plasma with physical quantities that varies only in the radial direction. The configuration is sketched in Fig. 7. The current density $J_z(r)$ is solely in the $\hat{z}$ direction, and the resulting magnetic field $B_\phi(r)$ is solely in the $\hat{\phi}$ direction. The total current necessary to confine the cylinder of plasma given a particular mean plasma pressure can be determined independent of the details of the radial pressure profile. One can also determine the pressure and magnetic field profiles for a given current density profile. The Bennett Pinch derivation follows that of J. D. Jackson [3].

The Bennett Pinch is a static equilibrium state, so there are no plasma flows and $\frac{d\vec{v}}{dt} = 0$. Therefore, from Eq. 7, the MHD equation of motion becomes

$$-\nabla p + \vec{J}\times\vec{B} = 0 \tag{27}$$

The $-\nabla p$ term in the MHD equation of motion is present in the ordinary hydrodynamic equation of motion. The $\vec{J}\times\vec{B}$ term is added in the MHD equation of motion because plasmas are responsive

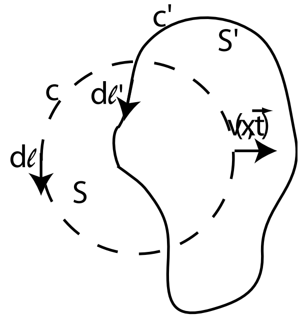

Figure 5: Each point on the dotted contour C moves at the plasma fluid velocity. It is deformed into contour C'. The flux through the contour is conserved.

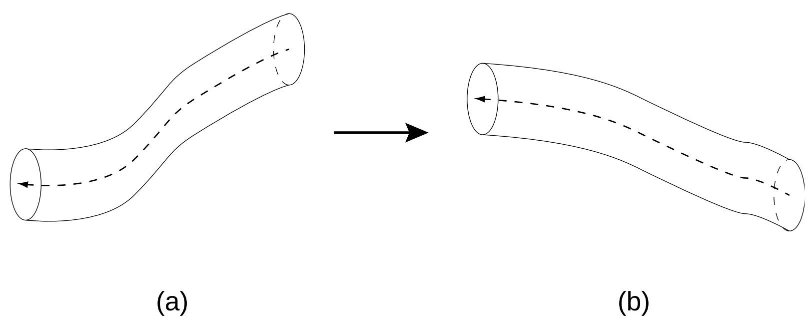

Figure 6: Panel (a) displays a portion of a magnetic field line (dotted line) and a surrounding tube that moves with the plasma fluid. Panel (b) displays the same field line and tube a short time later. The field lines are frozen into the plasma flow.

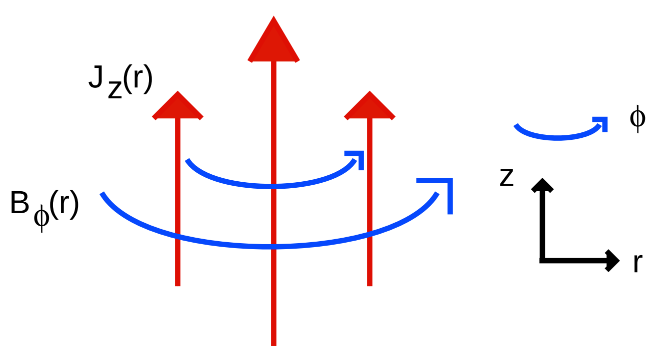

Figure 7: The Bennett Pinch. The current density, J_z, is purely in the axial or $\hat{z}$ direction. The magnetic field, B_ϕ, is purely in the azimuthal or $\hat{\phi}$ direction. Physical quantities vary only in the radial or $\hat{r}$ direction.

to electric and magnetic fields. There is no $\sigma\vec{E}$ term, where σ is the charge density, since a quasi neutral plasma is assumed. The plasma is at an equilibrium because the outward force due to the concentration of plasma in the column is balanced by the inward force of the axial current moving across the azimuthal magnetic field.

It is the inward pressure gradient that is responsible for the outward force, and the $\vec{J}\times\vec{B}$ force can be recast as a magnetic pressure gradient plus a curvature term. This is accomplished by first writing the current density in terms of the magnetic field. Ampere's law in differential form is

$$\mu_0\vec{J} = \nabla\times\vec{B}. \tag{28}$$

Substituting equation 28 into 27 yields

$$-\nabla p + \frac{1}{\mu_0}(\nabla\times\vec{B})\times\vec{B} = 0. \tag{29}$$

The vector identity

$$\nabla(\vec{F}\cdot\vec{G}) = \vec{F}\times(\nabla\times\vec{G}) + \vec{G}\times(\nabla\times\vec{F}) + (\vec{F}\cdot\nabla)\vec{G} + (\vec{G}\cdot\nabla)\vec{F} \tag{30}$$

may be used to rewrite Eq. 29. Substituting $\vec{B}$ for $\vec{F}$ and $\vec{G}$ in Eq. 30 yields

$$\nabla(\vec{B}^2) = 2\vec{B}\times(\nabla\times\vec{B}) + 2(\vec{B}\cdot\nabla)\vec{B}. \tag{31}$$

Rearranging Eq. 31 yields

$$(\nabla\times\vec{B})\times\vec{B} = (\vec{B}\cdot\nabla)\vec{B} - \frac{1}{2}\nabla(\vec{B}^2). \tag{32}$$

Substituting Eq. 32 into Eq. 29 yields

$$\frac{1}{\mu_0}(\vec{B}\cdot\nabla)\vec{B} - \nabla\frac{\vec{B}^2}{2\mu_0} - \nabla p = 0. \tag{33}$$

The terms involving $\vec{B}$ in Eq. 33 came from the $\vec{J}\times\vec{B}$ term in Eq. 27. The first term is the force due to changes in each component of the magnetic field in the direction of the field at a particular point. The second term is the gradient of the magnetic energy density, or the magnetic pressure. The third term is the gradient of kinetic pressure. These gradients are oppositely directed in the the case of the Bennett Pinch. Furthermore there is curvature in the azimuthal magnetic field, reflected in the first term, which further helps offset the outward force of the kinetic pressure.

In the case of the Bennett Pinch the magnetic field has only an azimuthal component and the magnetic field only varies in the radial direction so

$$\frac{1}{\mu_0}(\vec{B}\cdot\nabla)\vec{B} = -\frac{1}{\mu_0}\frac{B_\phi^2}{r}\hat{r}. \tag{34}$$

Since physical quantities in the Bennett Pinch configuration can vary only radially, only radial force balance is considered in Eq. 33. Using Eqs. 34, Eq. 33 becomes

$$-\frac{1}{\mu_0}\frac{B_\phi^2}{r} - \frac{d}{dr}(\frac{B_\phi^2}{2\mu_0}) - \frac{dp}{dr} = 0. \tag{35}$$

The MHD equation of motion (Eq. 7), which is a vector differential equation, has now been reduced to a scalar differential equation for the cylindrical geometry at hand. However, the total current required to confine a plasma of a particular mean pressure is of interest, and the differential equation is still not in an easily integrable form. Upon rearranging Eq. 35 and multiplying both sides by r^2, Eq. 35 becomes

$$r^2\frac{dp}{dr} = -\frac{1}{\mu_0}rB_\phi^2 - r^2\frac{d}{dr}(\frac{B_\phi^2}{2\mu_0}). \tag{36}$$

By substituting the identity

$$r^2\frac{d}{dr}(\frac{B_\phi^2}{2\mu_0}) = \frac{d}{dr}(r^2\frac{B_\phi^2}{2\mu_0}) - \frac{1}{\mu_0}rB_\phi^2, \tag{37}$$

Eq. 36 becomes

$$\frac{dp}{dr} = \frac{-1}{2\mu_0}\frac{1}{r^2}\frac{d}{dr}(r^2B_\phi^2). \tag{38}$$

Eq. 38 is now in a readily integrable form. Integrating both sides of Eq. 38 with respect to r yields

$$p(r) = p_0 - \frac{1}{2\mu_0}\int_0^r \frac{1}{r'^2}\frac{d}{dr'}(r'^2B^2)dr'. \tag{39}$$

, where p_0 is the plasma pressure at $r = 0$. Since the cylinder of plasma is confined, nearly all of the plasma is contained in the volume $r \leq R$, where R is the radius of the cylinder of plasma. The pressure at the boundary of the cylinder, $p(R)$, must vanish. This boundary condition allows us to solve for p_0:

$$p(R) = 0 = p_0 - \frac{1}{2\mu_0}\int_0^R \frac{1}{r'^2}\frac{d}{dr'}(r'^2B^2)dr'. \tag{40}$$

Rearranging Eq. 40 yields

$$p_0 = \frac{1}{2\mu_0}\int_0^R \frac{1}{r'^2}\frac{d}{dr'}(r'^2B^2)dr'. \tag{41}$$

Substituting Eq. 41 into Eq. 39 yields

$$p(r) = \frac{1}{2\mu_0}\int_r^R \frac{1}{r'^2}\frac{d}{dr'}(r'^2B^2)dr'. \tag{42}$$

As mentioned above, it is possible to find an expression for the current required to confine a plasma with a particular mean pressure. In the case of the Bennett Pinch, in which physical quantities vary only in the radial direction, mean pressure is

$$< p >= \frac{1}{\pi R^2}\int_0^R 2\pi r p(r)dr. \tag{43}$$

Integrating Eq. 43 by parts yields

$$< p >= \frac{2}{R^2}\left[\left(\frac{r^2}{2}p(r)\right)_0^R - \int_0^R r\frac{dp}{dr}dr\right]. \tag{44}$$

The integrated term in Eq. 44 vanishes because $p(R) = 0$. Substituting the expression for $\frac{dp}{dr}$ from Eq. 38 into Eq. 44 yields an expression for the mean pressure as a function of the total axial current:

$$< p >= \frac{\mu_0 I^2}{8\pi^2 R^2}. \tag{45}$$

The projected density and mean temperature for a magnetic fusion reactor are 10^{21} m^{-3} and 10^8 K respectively. Using the approximation $p = nkT$, the projected mean pressure for a reactor is

1.4×10^6Pa $\approx$ 14atm. Plugging these values into Eq. 45 yields $\frac{I}{R} = 9 \times 10^6 \frac{A}{m}$. Therefore, $9 \times 10^6 \frac{A}{m}$ times the radius of the Bennett Pinch plasma gives the current required for plasma equilibrium. Recall, however, that the equilibrium is unstable.

As mentioned above, one can find the magnetic field and pressure profiles corresponding to a particular current density profile. First suppose a constant axial current density. The magnetic field is given by Ampere's law in integral form:

$$\oint \vec{B} \cdot dl = \mu_0 I_{enclosed}. \tag{46}$$

Applying Ampere's law to the Bennett Pinch with constant current density yields

$$B_\phi = \frac{\mu_0 J_z r}{2}, r < R. \tag{47}$$

$$B_\phi = \frac{\mu_0 J_z R^2}{2r}, r > R. \tag{48}$$

For a constant current density, Eq. 42 becomes

$$p(r) = \frac{\mu_0 I(R)^2}{4\pi^2 R^2}[1 - \frac{r^2}{R^2}]. \tag{49}$$

The current density, magnetic field and pressure profiles are sketched in Fig. 8. For a constant current density, the pressure has a parabolic dependence on current and the axial pressure is twice the mean pressure (Eq. 45.)

Now suppose that all of the current is concentrated in a very thin layer at $r = R$. Such a current density profile can be modeled by a delta function:

$$J_z(r) = J_0 \delta(r - R) r \tag{50}$$

The magnetic field profile, can be obtained by Ampere's law in integral form, Eq. 46. Ampere's law requires the current enclosed by a ring in the $r - \phi$ plane centered on the axis of the cylinder, which can be obtained by integrating the current density:

$$I_{enc} = 2\pi J_0 \left\{ \begin{array}{c} 0, r < R \\ R^2, r > R \end{array} \right. . \tag{51}$$

Applying Ampere's law yields for the magnetic field

$$B_\phi = \left\{ \begin{array}{c} 0, r < R \\ \frac{\mu_0 J_0 R^2}{r}, r > R \end{array} \right. \tag{52}$$

The current density, magnetic field and pressure profiles are sketched in Fig. 9. In practice, the thin current layer would have a finite thickness and the current in the layer would have a finite magnitude, so using a delta function to model the current tube is an idealization. Therefore, the delta functions are smoothed in Fig. 9.

4 2-D MHD Equilibria: Grad-Shafranov Equilibrium

Grad-Shafranov Equilibrium (GSE) is a generalization of the same pressure balance analysis of the Bennett pinch to a wide class of plasma configurations. The plasma configuration created by merging two counter-helicity spheromaks in SSX-FRC is largely axisymmetric. The subsequent

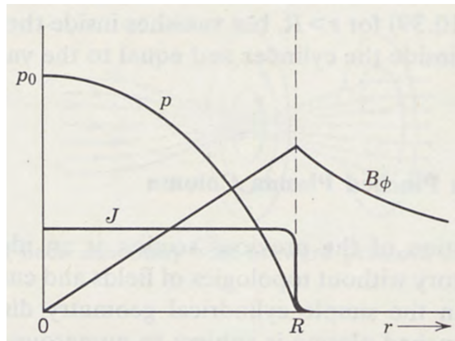

Figure 8: Radial profiles of current density, azimuthal magnetic field, and pressure for a Bennett pinch with constant current density. Figure taken from J. D. Jackson (1975).

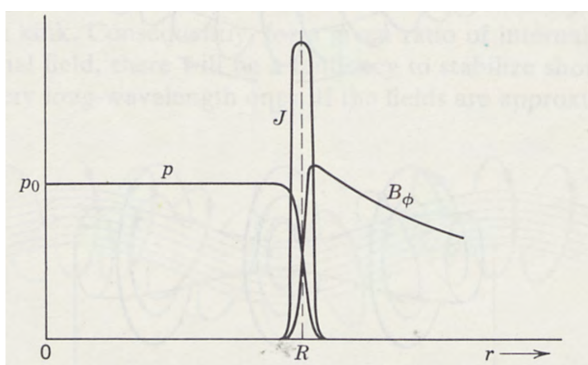

Figure 9: Radial profiles of current density, azimuthal magnetic field, and pressure for a Bennett pinch with a thin current layer at the plasma boundary. Figure taken from J. D. Jackson (1975).

derivation was undertaken because the experimental results were compared with solutions to the GSE using a GSE solver written in Matlab by J.A. Leuer. One of the few analytic solutions to the GSE is also presented below. Like the Bennett Pinch, GSE is axisymmetric, which means physical quantities cannot vary in ϕ, the azimuthal angle. However, GSE contrasts with the Bennett Pinch in that physical quantities can vary in z as well as in r. Therefore, GSE applies to such plasma configurations as spheromaks and tokamaks. One can derive a differential equation relating pressure, poloidal flux, and axial current for GSE. This differential equation is non-linear in poloidal flux and cannot be solved analytically in general. A simple analytical solution, the Solov'ev solution, shall be given along with numerical solutions for the boundary conditions of the SSX experiment. The following GSE derivation is based on that of P. Bellan [1].

As with the Bennett Pinch, we again assume the MHD approximation and specify static equilibrium for GSE. Therefore, the starting point for the derivation is again Eq. 27. It is restated below:

$$\nabla p = \vec{J} \times \vec{B}. \tag{53}$$

The magnetic field of the Grad-Shafranov Equilibrium can be written in a convenient form by separating it into toroidal and poloidal components. The analysis that follows is quite involved, but it is worthwhile because is allows us to recast Eq. 53, which is a vector differential equation, into a scalar differential equation. Arbitrary sample toroidal and poloidal field lines are shown in Fig. 10. The toroidal component can be obtained from Ampere's law in integral form, Eq. 46. Since the plasma is axisymmetric (i.e. the physical quantities have no ϕ dependence),

$$\vec{B}_t = B_\phi \hat{\phi} = \frac{\mu_0 I_z}{2\pi r} \hat{\phi}, \tag{54}$$

where I_z is the current enclosed by a circle of radius r centered on the z axis and in the r-ϕ plane. Making the substitution $\nabla\phi = \frac{\hat{\phi}}{r}$, Eq. 54 becomes:

$$\vec{B}_t = B_\phi \hat{\phi} = \frac{\mu_0 I_z}{2\pi} \nabla\phi. \tag{55}$$

Now an expression for the poloidal magnetic field must be obtained. One of Maxwell's equations states that

$$\nabla \cdot \vec{B} = 0. \tag{56}$$

For the axisymmetric plasma at hand, the divergence of the toroidal component of the magnetic field is also zero:

$$\nabla \cdot B_\phi \hat{\phi} = B_\phi (\nabla \cdot \hat{\phi}) + \hat{\phi} \cdot (\nabla B_\phi) = 0, \tag{57}$$

since $\nabla \cdot \hat{\phi} = 0$ and $\hat{\phi} \cdot \nabla B_\phi = \frac{1}{r}\frac{dB_\phi}{d\phi} = 0$. It follows from Eqs. 56 and 57 that the divergence of the poloidal component of the magnetic field is also zero:

$$\nabla \cdot \vec{B}_p = \nabla \cdot (B_r \hat{r} + B_z \hat{z}) = \nabla \cdot \vec{B} - \nabla \cdot B_\phi \hat{\phi} = 0, \tag{58}$$

For all scalar functions α and β, it is true that

$$\nabla \cdot (\nabla\alpha \times \nabla\beta) = 0. \tag{59}$$

Therefore, equating Eqs. 58 and 59 yields

$$\nabla \cdot (\nabla\alpha \times \nabla\beta) = \nabla \cdot \vec{B}_p. \tag{60}$$

or

$$\nabla\alpha \times \nabla\beta = \vec{B}_p + \nabla \times \vec{Q}, \tag{61}$$

where we have added the curl of an arbitrary vector. We choose $\nabla \times \vec{Q} = 0$; although this is not mathematically rigorous, it leads to the correct result. Since α and β are arbitrary functions, let

$$\nabla\beta = \nabla\phi = \frac{\hat{\phi}}{r}. \tag{62}$$

The choice $\nabla\beta = \nabla\phi$ guarantees that $\vec{B}_p$ is purely poloidal since the cross product generates a vector perpendicular to $\hat{\phi}$, the toroidal unit vector. Now let's determine the other function in the cross product, α, by computing the poloidal flux:

$$\int \vec{B}_p \cdot d\vec{S}_z \equiv \psi(r,z) \tag{63}$$

$$\psi(r,z) = \int_0^r [\nabla\alpha \times \nabla\phi] \cdot \hat{z} 2\pi r' dr' \tag{64}$$

$$= 2\pi \int_0^r \nabla\alpha \cdot (\nabla\phi \times \hat{z}) r' dr' \tag{65}$$

$$= 2\pi \int_0^r \nabla\alpha \cdot (\frac{\hat{\phi}}{r'} \times \hat{z}) r' dr' \tag{66}$$

$$= 2\pi \int_0^r \nabla\alpha \cdot \hat{r} dr' \tag{67}$$

$$= 2\pi \int_0^r \frac{d\alpha}{dr'} dr' \tag{68}$$

$$= 2\pi[\alpha(r,z) - \alpha(0,z)] \tag{69}$$

Therefore,

$$\nabla\alpha = \frac{1}{2\pi}\nabla\psi. \tag{70}$$

Inserting Eqs. 62 and 70 into Eq. 61 yields

$$\vec{B}_p = \frac{1}{2\pi}[\nabla\psi \times \nabla\phi]. \tag{71}$$

Adding together Eqs. 55 and 71 yields for the most general form for an axisymmetric magnetic field:

$$\vec{B} = \frac{1}{2\pi}[\nabla\psi \times \nabla\phi + \mu_0 I_z \nabla\phi] \tag{72}$$

Now the current density of the Grad-Shafranov equilibrium remains to be determined. The current density can be determined from the magnetic field by Ampere's law:

$$\vec{J} = \frac{1}{\mu_0}\nabla \times \vec{B} = \frac{1}{\mu_0}(\nabla \times \vec{B}_t) + \frac{1}{\mu_0}(\nabla \times \vec{B}_p). \tag{73}$$

The curl of the toroidal magnetic field generates the poloidal current density and the curl of the poloidal magnetic field generates the toroidal current density:

$$\frac{1}{\mu_0}\nabla \times \vec{B}_t = \vec{J}_p \tag{74}$$

and

$$\frac{1}{\mu_0}\nabla \times \vec{B}_p = \vec{J}_t \tag{75}$$

The proof is as follows: the curl of a purely toroidal vector is always poloidal since there is only one toroidal direction and the curl always generates a vector perpendicular to the original vector. However, the curl of a poloidal vector is not always toroidal. For an arbitrary poloidal vector, $\vec{F}$:

$$\nabla \times \vec{F} = \nabla \times (F_r\hat{r} + F_z\hat{z}) = \frac{1}{r}\frac{\partial F_z}{\partial \phi}\hat{r} + (\frac{\partial F_r}{\partial z} - \frac{\partial F_z}{\partial r})\hat{\phi} + \frac{1}{r}\frac{\partial F_r}{\partial \phi}\hat{z} \tag{76}$$

Thus the curl of a poloidal vector may have poloidal ($\hat{r}$ or $\hat{z}$) components. However, the Grad-Shafranov equilibrium (GSE) is axisymmetric, which means that no physical quantity varies in the toroidal direction. In the case of GSE,

$$\nabla \times \vec{F} = \nabla \times (F_r\hat{r} + F_z\hat{z}) = (\frac{\partial F_r}{\partial z} - \frac{\partial F_z}{\partial r})\hat{\phi} \tag{77}$$

Now the toroidal and poloidal current densities can be determined in terms of the poloidal flux and the axial current density by simply taking the curl of the poloidal and toroidal magnetic fields. From Eq. 55

$$\nabla \times \vec{B}_t = \frac{\mu_0}{2\pi}\nabla \times I_z\nabla\phi. \tag{78}$$

Using the vector identity $\nabla \times (f\vec{A}) = f\nabla \times \vec{A} + \nabla f \times \vec{A}$ and noting that the curl of a gradient is zero yields

$$\nabla \times \vec{B}_t = \frac{\mu_0}{2\pi}(\nabla I_z \times \nabla\phi). \tag{79}$$

$\nabla \times \vec{B}_t$ is demonstrably poloidal since it is proportional to a cross-product involving $\nabla\phi = \frac{\hat{\phi}}{r}$. The next step is to determine the curl of the poloidal magnetic field. From Eq. 71,

$$\begin{aligned}\nabla \times \vec{B}_p &= \frac{1}{2\pi}\nabla \times [\nabla\psi \times \nabla\phi] \\ &= \frac{1}{2\pi}\nabla \times [-\frac{1}{r}\frac{\partial\psi}{\partial z}\hat{r} + \frac{1}{r}\frac{\partial\psi}{\partial r}\hat{z}] \\ &= \frac{1}{2\pi}[-\frac{1}{r}\frac{\partial^2\psi}{\partial z^2} - \frac{\partial}{\partial r}(\frac{1}{r}\frac{\partial\psi}{\partial r})]\hat{\phi} \\ &= \frac{-r^2}{2\pi}\nabla \cdot (\frac{1}{r^2}\nabla\psi)\nabla\phi\end{aligned} \tag{80}$$

From Ampere's law and Eqs. 79 and 80,

$$\vec{J}_p = \frac{1}{2\pi}(\nabla I_z \times \nabla\phi) \tag{81}$$

$$\vec{J}_t = \frac{-r^2}{2\pi\mu_0}\nabla \cdot (\frac{1}{r^2}\nabla\psi)\nabla\phi \tag{82}$$

Now we have the magnetic field and current density of the GSE in terms of their poloidal and toroidal components. These can then be substituted into the original differential equation of motion. From Eq. 53,

$$\nabla P = (\vec{J}_t \times \vec{B}_t) + (\vec{J}_t \times \vec{B}_p) + (\vec{J}_p \times \vec{B}_t) + (\vec{J}_p \times \vec{B}_p). \tag{83}$$

We have found that

$$\vec{B}_t = \frac{\mu_0 I_z}{2\pi}\nabla\phi \tag{84}$$

$$\vec{B}_p = \frac{1}{2\pi}(\nabla\psi \times \nabla\phi) \tag{85}$$

$$\vec{J}_t = \frac{-r^2}{2\pi\mu_0}\nabla \cdot (\frac{1}{r^2}\nabla\psi)\nabla\phi \tag{86}$$

$$\vec{J}_p = \frac{1}{2\pi}(\nabla I_z \times \nabla\phi). \tag{87}$$

Eq. 83 simplifies somewhat. First note that the $(\vec{J}_t \times \vec{B}_t)$ term vanishes since $\vec{J}_t$ points in the same direction as $\vec{B}_t$. Also, ∇P cannot have a toroidal component because pressure cannot vary in the toroidal direction by axisymmetry. But since $\vec{J}_p \times \vec{B}_p$ generates a vector in the toroidal direction, it must vanish:

$$\vec{J}_p \times \vec{B}_p = 0. \tag{88}$$

Therefore, we are left with

$$\nabla P = (\vec{J}_p \times \vec{B}_t) + (\vec{J}_t \times \vec{B}_p). \tag{89}$$

Eq. 88 allows further simplifications of the differential equation of motion. Substituting into Eq. 88 yields

$$(\nabla I_z \times \nabla\phi) \times (\nabla\psi \times \nabla\phi) = 0. \tag{90}$$

From Eq. 90, it can be shown that $\nabla I_z \cdot \nabla\psi = 0$. It is already clear that ∇I_z is in the same plane as $\nabla\psi$ since neither gradient can have a component in the toroidal direction by axisymmetry. Applying the vector identity

$$(\vec{A} \times \vec{B}) \times (\vec{C} \times \vec{D}) = (\vec{A} \times \vec{B} \cdot \vec{C})\vec{D} - (\vec{A} \times \vec{B} \cdot \vec{D})\vec{C} \tag{91}$$

to Eq. 90 yields

$$\nabla I_z \times \nabla\phi \cdot \nabla\psi = 0. \tag{92}$$

Let $\nabla I_z \times \nabla\phi \equiv \vec{A}$ so that

$$\vec{A} \cdot \nabla\psi = 0. \tag{93}$$

$\vec{A}$ is in the same plane as ∇I_z and $\nabla\psi$ since $\nabla\phi$ is in the cross product defining $\vec{A}$. From the cross product defining $\vec{A}$ it is also clear that $\vec{A} \cdot \nabla I_z = 0$. Since $\vec{A} \cdot \nabla\psi = 0$ also, ∇I_z is parallel to $\nabla\psi$. The relationships among these vectors are conveyed in Fig. 11. The fact that ∇I_z is parallel to $\nabla\psi$ implies that at any point the value of ∇I_z is related to the value of $\nabla\psi$ by a scalar. Therefore

$$\nabla I_z = f(\psi)\nabla\psi. \tag{94}$$

$f(\psi)$ can be identified as $I_z'(\psi)$, the derivative of I_z with respect to ψ, by the chain rule:

$$\nabla I_z = I_z'(\psi)\nabla\psi. \tag{95}$$

Substituting this equation into the expression for the poloidal current density yields

$$\vec{J}_p = \frac{I_z'}{2\pi}(\nabla\psi \times \nabla\phi). \tag{96}$$

Substituting the currents and fields into Eq. 89 yields

$$\nabla P = \frac{I_z'}{2\pi}(\nabla\psi \times \nabla\phi) \times \frac{\mu_0 I_z}{2\pi}\nabla\phi + \frac{-r^2}{2\pi\mu_0}\nabla \cdot (\frac{1}{r^2}\nabla\psi)\nabla\phi \times \frac{1}{2\pi}(\nabla\psi \times \nabla\phi). \tag{97}$$

Rearranging and using

$$\nabla\phi \times (\nabla\psi \times \nabla\phi) = \nabla\psi(\nabla\phi \cdot \nabla\phi) \tag{98}$$

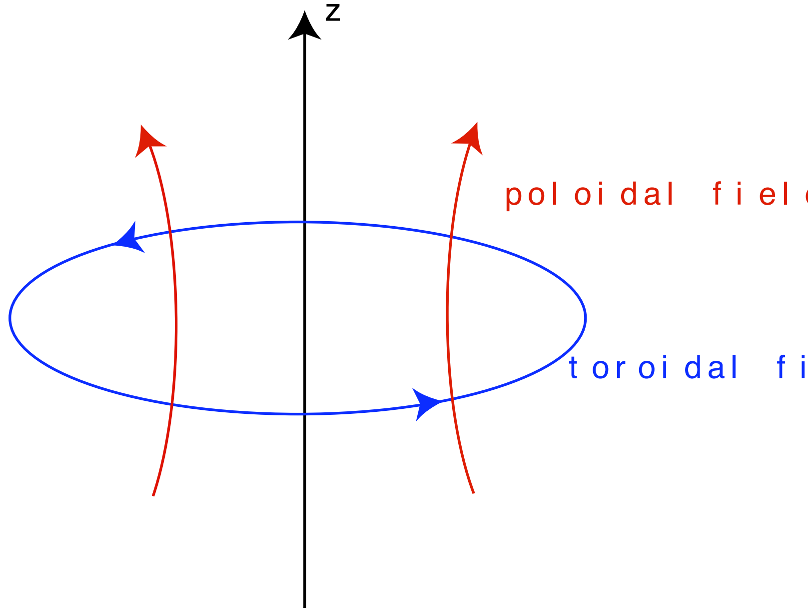

Figure 10: Arbitrary toroidal and poloidal field lines.

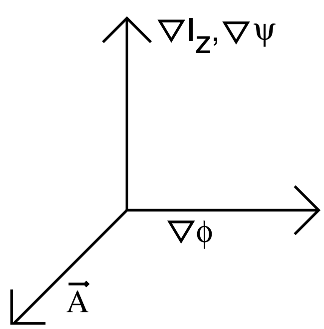

Figure 11: It can be deduced that ∇I_z is parallel to $\nabla\psi$.

yields

$$\nabla P = -[\frac{\mu_0 I_z' I_z}{(2\pi r)^2} + \frac{1}{(2\pi)^2\mu_0}\nabla\cdot(\frac{1}{r^2}\nabla\psi)]\nabla\psi. \tag{99}$$

∇P is also parallel to $\nabla\psi$, so

$$\nabla P = P'(\psi)\nabla\psi. \tag{100}$$

Substituting this expression for ∇p into Eq. 99 yields a common factor of $\nabla\psi$ on both sides of the equation. The common factor can be canceled to yield a *scalar* differential equation:

$$\nabla\cdot(\frac{1}{r^2}\nabla\psi) + 4\pi^2\mu_0 P' + \frac{\mu_0^2}{r^2} I_z I_z' = 0. \tag{101}$$

This is the Grad-Shafranov equation. It involves three independent quantities: ψ, $P(\psi)$ and $I_z(\psi)$. Two of these must be specified to determine the third.

4.1 Solov'ev Solution

Now a simple analytical solution to the Grad-Shafranov equation, the Solov'ev solution, is presented. Suppose the pressure is a linear function of the poloidal flux

$$P = P_0 + \lambda\psi. \tag{102}$$

and the axial current is constant

$$I_z(\psi) = I_{z0} \tag{103}$$

$$I_z'(\psi) = 0. \tag{104}$$

The current density profile is a delta function centered on $r = 0$. The solution to the Grad-Shafranov equation, given these pressure and current functions, is

$$\psi(r,z) = \psi_0 \frac{r^2}{r_0^4}[2r_0^2 - r^2 - 4\alpha^2 z^2]. \tag{105}$$

Rearranging yields

$$\psi(r,z) = \psi_0(\frac{r}{r_0})^2[2 - (\frac{r}{r_0})^2 - 4\alpha^2(\frac{z}{r_0})^2]. \tag{106}$$

Substituting $r = r_0$ and $z = 0$ into the above equation yields $\psi(r,z) = \psi_0$, which indicates that r_0 is the radial coordinate of the magnetic axis. Now we define the normalized position variables $r_n \equiv \frac{r}{r_0}$ and $z_n \equiv \frac{z}{r_0}$ so the expression for ψ becomes

$$\psi(r,z) = \psi_0 r_n^2[2 - r_n^2 - 4\alpha^2 z_n^2)]. \tag{107}$$

A contour plot of $\psi(r_n, z_n)$ is shown in Fig. 12. The constants were assigned the values $\alpha = 1$ and $\psi_0 = 1$. Notice that the negative contours go to infinity (open contours) and the positive contours are closed. The dark contour corresponds to the separatrix, which is the contour separating closed and open contours. It is determined by setting $\psi(r_n, z_n) = 0$. In the Solov'ev solution, the separatrix is an ellipse with an eccentricity given by

$$\epsilon = \frac{\sqrt{2 - \frac{1}{2\alpha^2}}}{\sqrt{2}} \tag{108}$$

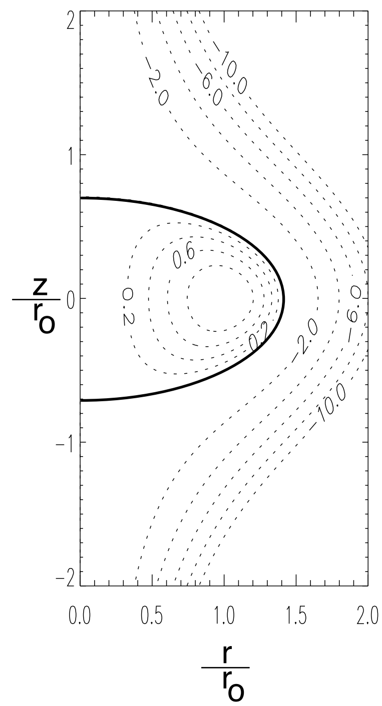

Figure 12: Contour plot of $\psi(r, z)$ for the Solov'ev solution to the Grad-Shafranov equation. r_0 is the radius of the magnetic null or magnetic axis, and the solid contour corresponds to $\psi = 0$ or the separatrix.

so that α determines the eccentricity of the separatrix. As mentioned above, the magnetic field lines lie in the flux surfaces. Since the charged plasma particles follow the magnetic field lines in helical orbits (assuming a collisionless plasma) each parcel of plasma is confined to a flux surface (within one Larmor radius.) Therefore, the poloidal magnetic field and the toroidal current are responsible for confinement of the plasma.

Substituting the Solov'ev solution back into the Grad-Shafranov equation determines λ:

$$\lambda = \frac{\psi_0}{r_0^4}\frac{2(1+\alpha^2)}{\pi^2\mu_0}. \tag{109}$$

Substituting this expression for λ back into the expression for P yields

$$P = P_0 + \frac{\psi_0}{r_0^4}\frac{2(1+\alpha^2)}{\pi^2\mu_0}\psi. \tag{110}$$

Since the plasma is confined in the GSE, the pressure at the edge of the plasma vanishes. Let the poloidal flux at the edge be defined as ψ_{edge} so that P_0 can be defined in terms of ψ_{edge}. The above equation becomes

$$P(\psi) = \frac{2\psi_0}{\pi^2 r_0^4\mu_0}(1+\alpha^2)[\psi - \psi_{edge}]. \tag{111}$$

4.2 Spheromaks

Spheromaks are important in SSX-FRC because the spheromak/FRC hybrid is formed from the merger of two counter-helicity spheromaks. Counter-helicity means that the magnetic field lines of the two spheromaks have opposite handedness. Spheromaks are also important in SSX-FRC because the spheromak/FRC hybrid has some spheromak-like properties, and the tilted hybrid resembles a spheromak even more (i.e. no observed anti-parallel flux bundles.) Therefore, it is beneficial to summarize some of the properties of spheromaks.

Spheromaks are compact torus (i.e. simply connected) plasma equilibria with comparable toroidal and poloidal magnetic fields. An isolated axisymmetric cylindrical spheromak in its lowest energy state and bounded by a cylindrical flux conserver is considered here because the spheromaks that merge to form the hybrid in SSX-FRC are well described by this model [15]. The Grad-Shafranov equation describes this spheromak since it is axisymmetric. Let us assume that the electromagnetic force is much greater than the pressure force so that the ∇p term is negligible and the equation of motion for the equilibrium becomes

$$\vec{J} \times \vec{B} = 0. \tag{112}$$

Using Ampere's law yields

$$(\frac{\nabla \times \vec{B}}{\mu_0}) \times \vec{B} = 0, \tag{113}$$

which implies that $\nabla \times \vec{B}$ and $\vec{B}$ are parallel and the magnetic field is an eigenvector of the curl operator with eigenvalue λ:

$$\nabla \times \vec{B} = \lambda \vec{B}. \tag{114}$$

The minimum energy state is of interest here, and λ is proportional to the ratio of energy to helicity, so the least possible value of λ is chosen when solving Eq. 114. The solution is

$$B_r = B_0\frac{k_z}{k_r}J_1(k_r r)\cos(k_z z) \tag{115}$$

$$B_t = B_0\lambda J_1(k_r r)\sin(k_z z) \tag{116}$$

$$B_z = B_0 J_0(k_r r)\sin(k_z z) \tag{117}$$

where

$$k_z = \frac{\pi}{L}, k_r \approx \frac{3.8317}{R}, \lambda = \sqrt{\frac{k_z^2}{k_r^2} + 1} \tag{118}$$

and R and L are the radius and length of the flux conserver respectively. This solution is the force-free Taylor state. The Taylor state is the lowest magnetic energy state that the plasma can reach subject to the constraint of helicity conservation. The helicity, K, is defined as [2]

$$K = \int_V \vec{A} \cdot \vec{B} d^3 r. \tag{119}$$

In fact, helicity is not absolutely conserved, but it can be considered conserved on the time scale of magnetic energy decay. The poloidal flux function is given by

$$\psi = B_0 \frac{r}{k_r} J_1(k_r r) sin(k_z z). \tag{120}$$

The radial location of the magnetic null and peak flux can be found by maximizing Eq. 120 or finding the root of the expression for B_z within the range of the flux conserver. The magnetic null is at

$$R \approx 0.63 r_s \tag{121}$$

Substituting Ampere's law into Eq. 114 yields

$$\vec{J} = \frac{\lambda}{\mu_0} \vec{B}, \tag{122}$$

which indicates that $\vec{J}$ is proportional and parallel to $\vec{B}$. Integrating both sides of the above equation over area yields

$$I_z = \frac{\lambda}{\mu_0} \psi. \tag{123}$$

λ was chosen to be minimum and is therefore constant, so I_z is a linear function of ψ and the state is said to have a flat current profile. Eq. 123 satisfies the zero-pressure Grad-Shafranov equation, which is (from Eq. 101)

$$r^2 \nabla \cdot (\frac{1}{r^2} \nabla \psi) + \mu_0^2 I_z I_z' = 0. \tag{124}$$

Substituting Eq. 123 into Eq. 124 yields a differential equation in ψ:

$$r^2 \nabla \cdot (\frac{1}{r^2} \nabla \psi) + \lambda^2 \psi = 0. \tag{125}$$

Now consider the case where λ is not constant and the plasma is not in a Taylor state. These states have been used to model spheromaks in decay, formation or sustainment [23, 22]. If λ is an increasing function of ψ, then there is extra current density at the flux center and the flux peak moves outwards due to the interaction between oppositely directed currents at opposite sides of the torus. If λ is a decreasing function of ψ, then there is extra current density at the edge and the flux peak moves inwards due to an increase in magnetic pressure between the edge of the spheromak and the flux conserver.

The simplicity of spheromaks makes them attractive fusion reactor concepts. Spheromak magnetic fields are created with internal currents, so there is less need for expensive magnetic coils for spheromaks compared to tokamaks. Spheromaks are several orders of magnitude behind tokamaks in terms of temperature and energy confinement time, but fewer resources have been devoted to spheromak research than to tokamak research. Once more attention is given to the fusion potential of spheromaks, the promise of spheromaks may be confirmed, or it is possible that a fatal flaw in the spheromak concept will be discovered. For instance, spheromaks have been created with a value for β (the ratio of kinetic energy density to magnetic energy density) that is greater than that predicted by MHD (as mentioned in Bellan, p. 265 [2]). Since a high kinetic energy density is needed for a fusion plasma, and a high magnetic energy density adds to the complexity and cost of a fusion reactor, it is desirable to find a plasma equilibrium state with a high β. However, as temperature and confinement time are increased, and MHD begins to better describe the plasma, the anomalously high β value may decrease [2].

4.3 The Field Reversed Configuration

The hybrid plasma configuration created by merging two counter-helicity spheromaks in SSX-FRC shares some of the characteristics of the field reversed configuration (FRC). Field reversed configurations, like spheromaks, are axisymmetric compact toroidal (CT) plasma configurations. However, unlike spheromaks, the ideal FRC has no toroidal magnetic field component and is confined solely by poloidal magnetic fields. The lack of a toroidal field means that the FRC has no helicity (where helicity is defined by Eq. 119) and that it has a high β (β is defined in Eq. 1). The high β makes the FRC attractive as a fusion reactor. Spheromaks have $\beta \approx 0.1$ whereas a typical FRC has $\beta \approx 1.0$.

FRC's have no toroidal field coils, which allows for free plasma exhaust so that plasma energy can be readily converted to electric energy through direct conversion. Also, FRC's are potential advanced D/3-He fusion reactors due to their high β [38]. The D/3-He fusion reaction is given by

$$D + 3\text{−He} \rightarrow 4\text{−He}\ (3.67MeV) + p\ (14.67MeV). \tag{126}$$

The cross section of this reaction is lower than that of the D/T fusion reaction, but the higher $\beta \propto n$ may compensate for this discrepancy. The advantage of D/3-He fusion is that all of the products of the reaction are charged so that thermal energy could be converted directly into electrical energy. Furthermore, there are no uncharged products of the D/3-He reaction, which means that the products can be magnetically confined. In contrast, the energetic neutrons produced in D/T fusion are not confined by magnetic fields. Instead, the neutrons exit the plasma and activate the atoms in the chamber wall. Enthusiasm for FRC's as fusion reactors is tempered by concerns about their stability, and more research is needed to ascertain their stability. The vulnerability of FRC's to the tilt instability is elaborated on in the subsequent section on stability.

The name "field reversed configuration" has historical significance. FRC's were originally made by quickly reversing the axial magnetic field in a theta pinch confinement scheme (see Fig. 13) [44]. In this method, a long cylindrical chamber surrounded by a solenoid is used. First gas inside the chamber is ionized and a solenoidal magnetic field is frozen into the resulting plasma. Next the applied field is quickly reversed. However, the reversed field cannot penetrate the highly conductive plasma very well. The result is radial compression and reconnection of the field lines at the ends of the cylinder. After axial contraction, the plasma settles into an FRC equilibrium.

It is useful to classify FRC's as best described by an MHD model or a kinetic model in which finite larmor radius effects are important. Such a classification will be important when discussing stability in later sections. The condition for an MHD FRC is

$$s = \text{number of gyroradii between field null and separatrix} \gg 1. \tag{127}$$

The theta-pinch formation method produces a relatively low flux, high temperature FRC. Since $s \propto \frac{1}{\text{ion gyroradius}} \propto \frac{B}{T^{1/2}}$, it is difficult to create high s, MHD plasmas using this technique. The

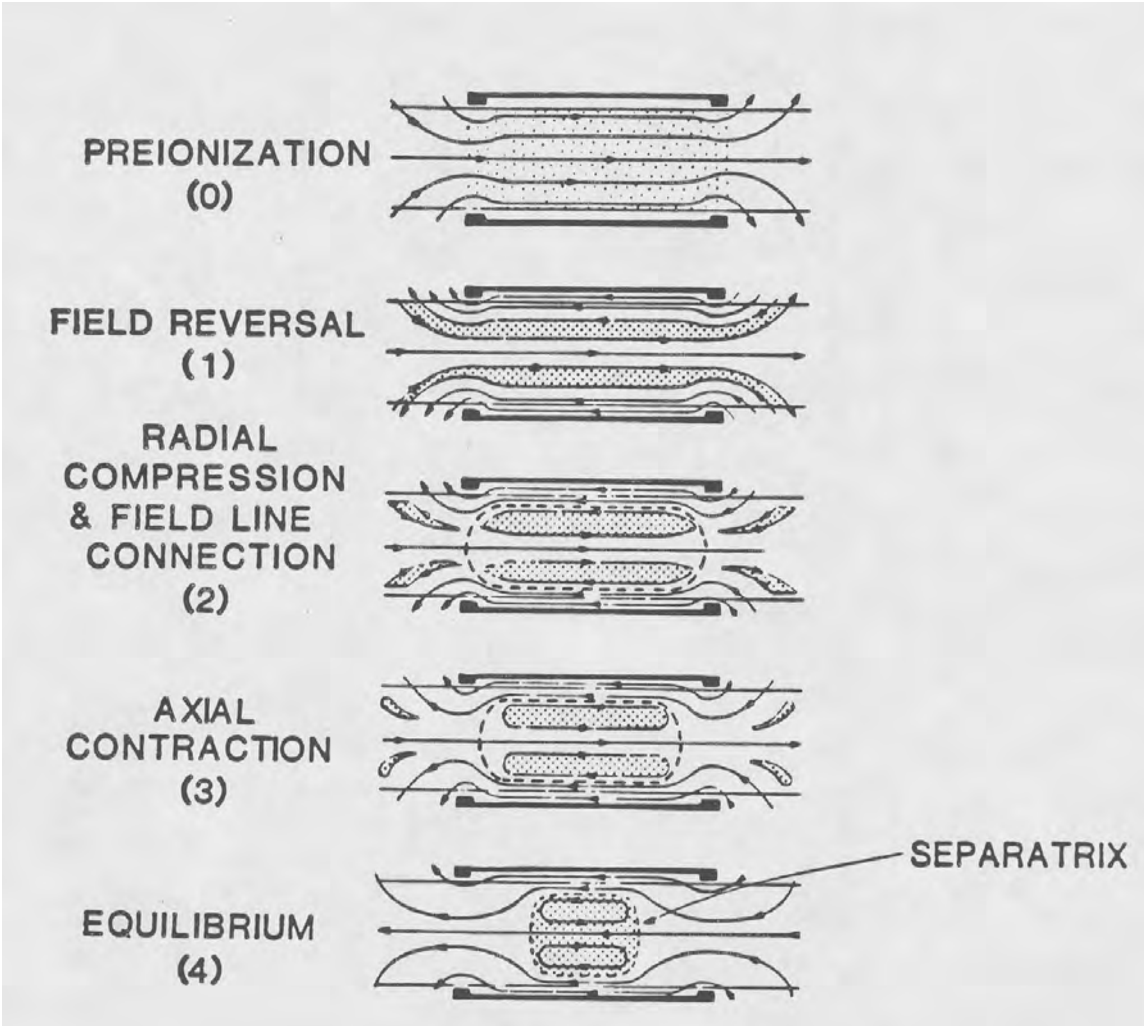

Figure 13: The formation process for the FRC using a theta-pinch. Figure taken from Tuszewski [44].

theta pinch technique for creating FRC's also results in axially elongated, or prolate, FRC's. The elongation of an FRC is defined by $E = \frac{Z_s}{R_s}$ where Z_s is the separatrix half length and R_s is the separatrix radius, and prolate FRC's are defined as those with $E \geq 2$ [3].

It is possible to find the radial location of the peak poloidal flux or, equivalently, the radial location of the field null of an elongated FRC regardless of the pressure profile. For a plasma equilibrium in general, force balance is given by Eq. 33:

$$\frac{1}{\mu_0}(\vec{B} \cdot \nabla)\vec{B} - \nabla \frac{B^2}{2\mu_0} - \nabla p = 0. \tag{128}$$

In the case of an ideal FRC, we assume straight field lines in the $\hat{z}$ direction near the midplane, so that the first term in Eq. 128, which corresponds to changes in the magnetic field in the direction of the magnetic field, vanishes and $B^2 \rightarrow B_z^2$. We also consider only radial force balance, so Eq. 128 becomes

$$\frac{1}{2\mu_0}\frac{\partial B_z^2}{\partial r} + \frac{\partial p}{\partial r} = 0. \tag{129}$$

Integrating the above equation yields

$$\frac{B_z^2}{2\mu_0} + p = p_M \tag{130}$$

where p_M is the maximum pressure. Rearranging Eq. 130 yields

$$B_z = \pm\sqrt{2\mu_0(p_M - p(\psi))} \equiv \pm f(\psi) \tag{131}$$

where it is assumed that p is only a function of poloidal flux. Suppose that the z-axis is oriented along the geometric axis of the FRC and the positive z direction is that of the magnetic field on the geometric axis. With this orientation of the coordinate axes, the axial field of the FRC is given by

$$B_z = \sqrt{2\mu_0(p_M - p(\psi))} = f(\psi), r < R \tag{132}$$

$$B_z = -\sqrt{2\mu_0(p_M - p(\psi))} = -f(\psi), R < r < r_s \tag{133}$$

where R is the field null radius and r_s is the separatrix radius. Now the relation

$$\frac{d\psi}{B_z} = rdr \tag{134}$$

follows from the definition of poloidal flux. Substituting the expression for B_z from Eq. 131 into the above equation yields

$$\frac{d\psi}{f(\psi)} = rdr, r < R \tag{135}$$

and

$$\frac{d\psi}{-f(\psi)} = rdr, R < r < r_s. \tag{136}$$

Integrating the first equation over the valid range yields

$$\int_{\psi(0)}^{\psi(R)} \frac{d\psi}{f(\psi)} = \int_0^R rdr. \tag{137}$$

By the definition of the flux function, $\psi(0) = 0$ and $\psi(R) = \psi_M$ where ψ_M is the maximum flux. Therefore

$$\int_0^{\psi_M} \frac{d\psi}{f(\psi)} = \frac{R^2}{2}. \tag{138}$$

Similarly,

$$-\int_{\psi(R)}^{\psi(r_s)} \frac{d\psi}{f(\psi)} = \int_R^{r_s} rdr, \tag{139}$$

and since $\psi(r_s) = 0$,

$$\int_0^{\psi_M} \frac{d\psi}{f(\psi)} = \frac{r_s^2}{2} - \frac{R^2}{2}. \tag{140}$$

Equating the two expressions for $\int_0^{\psi_M} \frac{d\psi}{f(\psi)}$, Eqs. 138 and 140, yields

$$R = \frac{r_s}{\sqrt{2}} \approx 0.71 r_s. \tag{141}$$

The location of the field null/flux peak for the FRC given by the above equation is to be contrasted with that of the spheromak in Eq. 121. The difference between the values for R in the spheromak and the FRC becomes important in the analysis of the hybrid created in SSX-FRC since the hybrid has some spheromak characteristics and some FRC characteristics.

An alternative method for producing FRC's is merging counter-helicity spheromaks together. It was pioneered by Ono on the TS-3 device at the University of Tokyo [12, 13]. In this method, two counter-helicity spheromaks with opposing toroidal magnetic fields collide axially. The result depends on the total helicity of the two spheromak system. If the helicity is above a threshold value, which is close to zero, the merged spheromaks relax to a new spheromak. If the helicity is below a threshold value, the merged spheromaks relax to an FRC. Since the FRC has not toroidal magnetic field, the current density and field are not parallel, which means that the FRC is not a Taylor state (which was discussed in the section of spheromaks.) The relaxation to an FRC is a novel process distinct from the Taylor relaxation. In TS-3, the β value for the merging spheromaks increases from 0.1 before merging to 0.7-1.0 within 15 μs. The most important aspect of this FRC formation process is that magnetic flux is high and temperature is low relative to theta-pinch FRC's. The resulting FRC has a large s and is within the MHD regime.

Counter-helicity spheromaks are also merged in SSX-FRC, but somewhat different results are obtained in SSX-FRC than in TS-3. Most notably, the FRC's in TS-3 have nearly zero toroidal magnetic field whereas there is always some residual, anti-parallel toroidal field in SSX-FRC. Furthermore, the FRC's in TS-3 are not tilt unstable. This is perhaps due to the use of a central conducting rod that runs down the axis of TS-3.

5 MHD Instabilities

Part of the motivation for undertaking this study was to determine the stability of a fully MHD FRC-like configuration. It was suspected that the most severe instability would be the tilt instability. This section on MHD instabilities elaborates on the kink instability, which is present in the Bennett pinch configuration discussed above, as well as the tilt instability, which is the toroidal analog of the kink instability.

As mentioned above, the Bennett pinch is an infinite cylindrical plasma with an axial current and an azimuthal magnetic field. In this discussion we consider the Bennett pinch with all of the current concentrated at the surface so that $\nabla P = 0$ inside the plasma as shown in Fig. 9. If a small perturbative kink is applied to the cylinder, as in Fig. 14, the azimuthal field bunches together on top and spreads out on the bottom. The result is increased magnetic pressure on top and decreased magnetic pressure on the bottom. Since the gradient in magnetic pressure results in an oppositely directed force, the kink becomes more severe. The positive feedback results in an unstable plasma. It is possible to stabilize the Bennett pinch against the kink by adding an axial

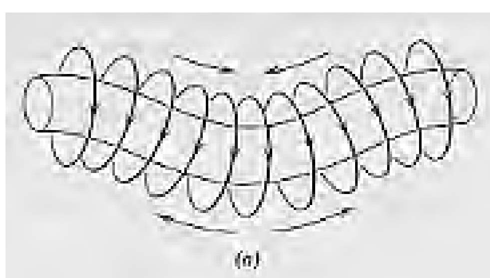

Figure 14: A small perturbative kink is applied to the unstable Bennett pinch plasma equilibrium. The kink becomes increasingly severe. Figure taken from J. D. Jackson (1975).

magnetic field. With an axial field, a kink in the plasma column would result in an increase in the magnetic tension in the axial field as shown in Fig. 15. The tension in the axial field is reflected in the $(\vec{B} \cdot \nabla)\vec{B}$ term in the MHD equation of motion. Note that a long wavelength kink would result in less tension than a short wavelength kink. The Bennett pinch is stable if $\lambda < 14R$, where λ is the wavelength of disturbance and R is the radius of the plasma [21].

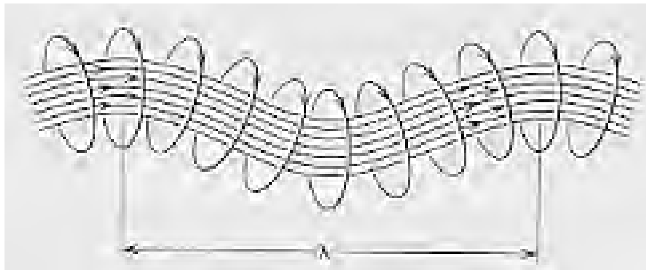

Figure 15: An axial magnetic field adds stability to the Bennett pinch. Figure taken from J. D. Jackson (1975).

The presence of a close fitting conducting boundary also has a stabilizing effect on the Bennett pinch. As argued above, flux is conserved in a perfectly conducting medium, whether it be an ideal MHD plasma or a perfectly conducting boundary. Therefore, if a column of plasma begins to kink, the existence of a close fitting conducting boundary causes the azimuthal field that is external to the plasma to bunch up near the boundary as shown in Fig. 16. There is an increase in magnetic pressure due to the bunching of the field lines near the conductor that offsets the decrease in magnetic pressure on the outer side of the kink.

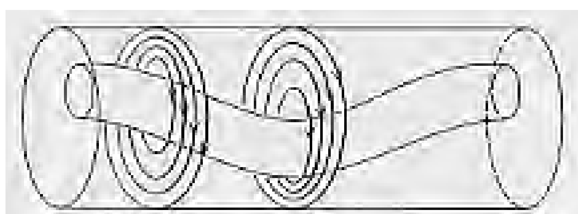

Figure 16: An close fitting conducting boundary adds stability to the Bennett pinch. Figure taken from J. D. Jackson (1975).

FRC's with elongation above a threshold value are susceptible to the tilt instability in the MHD approximation. The FRC's generated using the theta pinch method are typically highly elongated, so one would expect that they are unstable if they are MHD plasmas. A simple argument for the value of this threshold is as follows. The poloidal flux is given by

$$\psi = \int_0^r B_z(2\pi r dr) \tag{142}$$

where B_z is the axial component of the magnetic field and r is the radius of a surface of integration as shown in Figure 17. The top panel in Figure 17 shows an untilted FRC. The maximum flux occurs at approximately $r = \frac{R}{2}$. The mean poloidal (axial) field for the untilted FRC is given by

$$\bar{B}_1 = \frac{\psi(\frac{R}{2})}{\pi(\frac{R}{2})^2}. \tag{143}$$

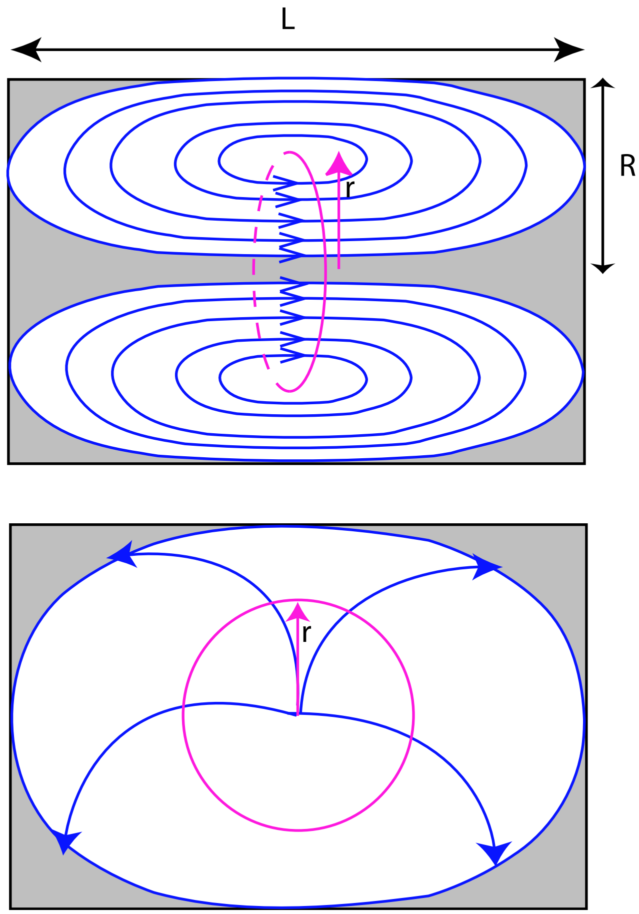

Figure 17: The top panel shows an untilted FRC. The pink circle of radius r is a surface of integration for calculating poloidal flux. The bottom panel shows a tilted FRC. The boundary of the flux surface moves with the plasma, resulting in a larger r.

The mean magnetic energy density for the untilted FRC is given by

$$\bar{W}_1 = \frac{\bar{B}_1^2}{2\mu_0}. \tag{144}$$

Now consider the tilted FRC shown in the bottom panel of Figure 17. The integration surface with $r = \frac{R}{2}$ shown in the top panel moves with the plasma when it tilts and the flux through the surface is conserved since the FRC is composed of an MHD plasma. However, the integration surface in the tilted FRC now has different dimensions as shown in Figure 17. The mean field in the tilted FRC is given by

$$\bar{B}_2 = \frac{\psi}{\pi(\frac{R}{2})(\frac{L}{4})}. \tag{145}$$

The mean magnetic energy density for the tilted FRC is given by

$$\bar{W}_2 = \frac{\bar{B}_2^2}{2\mu_0}. \tag{146}$$

The ratio of the magnetic energies for the tilted and untilted FRC's is given by

$$\frac{W_2}{W_1} = (\frac{2R}{L})^2. \tag{147}$$

Therefore, if $2R < L$ then the FRC is tilt unstable. This criterion is equivalent to $E < 1$ since the elongation E is defined as the separatrix half length divided by the separatrix radius. This is an approximate result. A more sophisticated computation has been used to determine that the elongation threshold for a spheromak is [5]

$$E = 0.83. \tag{148}$$

One would expect that the elongation threshold for spheromaks is somewhat different from that of FRC's due to the existence of toroidal field and the associated magnetic energy density in spheromaks.

Many experimental studies show that elongated FRC's are stable [44]. As noted above, the theta pinch formation method produces a relatively low flux, high temperature FRC characterized by a low value of s. The theta pinch FRC may be stable due to finite larmor radius effects not included in the MHD approximation. On the other hand, the hybrid configuration created in SSX is well into the MHD regime and is still tilt unstable, allowing us to test the stability of this FRC-like hybrid in the MHD regime.

Fourier analysis will be employed in a subsequent section in order to analyze the SSX-FRC data, so a discussion of the tilt instability in the context of Fourier analysis is worthwhile. The tilt instability has toroidal mode number $m = 1$, where the dependence of the magnetic field on angle is given by

$$\vec{B}_i \propto \cos(m\phi + \delta)\hat{i} \tag{149}$$

where $\vec{B}_i$ is the i^{th} component of the magnetic field. The right side of Figure 18 shows the change in the magnetic field for the points along a ring inside the field null of the untilted FRC shown in the top panel of Figure 17 as it begins to tilt towards the state shown in the bottom panel. Since the orientation of the basis vectors in cylindrical coordinates depend on position, it is not possible to define the orientation of the coordinate axes on the right side of Fig. 18 absolutely. Hence, the left side of Figure 18 defines the orientation of the coordinates axes on the right side of Fig. 18 at various values of ϕ, where $\phi = 0$ along the ray at the center of the FRC and coming out of the page in Fig. 17. The unperturbed field is purely in the axial direction at the points along the ring inside the field null. Therefore, there is no ϕ dependence of the magnetic field and the toroidal mode number of the unperturbed field is zero. Comparing the perturbed field on the right side of Figure 18 with the basis vectors on the left side, it is apparent that there is still no ϕ dependence of the field in the z direction. However, there is a sinusoidal dependence on ϕ for the fields in the r and ϕ directions. The direction of the field goes through one oscillation as ϕ goes from 0 to 2π, so the toroidal mode number of the tilt instability is $m = 1$.

6 Swarthmore Spheromak Experiment-Field Reversed Configuration (SSX-FRC)

6.1 Theoretical Motivation

As mentioned in the section on MHD, fusion plasmas must be MHD plasmas, which are characterized by a large value of s. FRC reactors that use D-T fuel might require $s \approx 20 - 40$ [44]. However, FRC's created using the theta-pinch technique are typically characterized by $s \leq 2$. Such small s FRC's are better described by finite Larmor radius (FLR) theory rather than MHD and have stability properties that contrast with those of MHD plasmas. According to MHD, FRC's with $E > 2$ are highly unstable, as shown in the stability section. However, according to FLR, elongation adds to the stability of an FRC, and the stability criterion is $\frac{s}{E} \leq \frac{1}{4}$ [42]. Observation of the tilt instability in FRC's was not reported until 1991, when Tuszewski *et al* found that FRC's are grossly stable when $\frac{s}{E} < 0.2 - 0.3$ but show MHD-like tilt instabilities when $\frac{s}{E} \approx 1$ [42]. However, the observation of the tilt was inferred from external magnetic probes and comparison with simulations. Internal measurements of the magnetic field were lacking because of the necessarily high temperature of theta-pinch FRC's. Furthermore, the reported dependence of tilt amplitude on $\frac{s}{E}$ was still based on modest $s(\approx 1 - 5)$.

Oblate FRC's ($E < 1$) have different stability properties than prolate FRC's. The $n = 1$ internal tilt mode in prolate FRC's becomes an external mode in oblate FRC's and can be stabilized by a close-fitting flux conserver [3]. Oblate FRC's were studied with an array of internal magnetic probes in the TS-3 spheromak merging device in Japan [46, 12, 13]. However, conclusive results on the stability of oblate FRC's were hampered by the existence of a central conducting rod along the axis of the merging spheromaks.

Simulated FRC's in both the kinetic ($s \approx 3$) and MHD ($s \approx 12$) regimes were studied by Omelchenko. These simulations suggest that the anomalous stability of FRC's is in fact due to spontaneously generated, oppositely directed toroidal flux and/or the associated poloidal ion flows rather than finite Larmor radius effects [32]. The SSX-FRC study was designed to test the hypothesis that anti-parallel bundles of toroidal flux produce stability in MHD FRC's. SSX-FRC uses the spheromak merging technique of FRC formation pioneered by Ono *et al*, and the resulting spheromak is well into the MHD regime with $s > 10$. The amount of anti-parallel toroidal flux is varied by limiting the extent to which the counter-helicity spheromaks are allowed to merge. As a result, the FRC's in SSX-FRC may be more properly called spheromak/FRC hybrids since the midplane region resembles an FRC whereas the end regions resemble spheromaks. The dimensions of the flux conserver in SSX-FRC were deliberately chosen so that the hybrid is elongated enough to be MHD tilt unstable ($E_{SSX} = 1.56 > E_{thresh} = 0.83$.) The elongation threshold for a spheromak was given in Eq. 148. Besides the high s value of the SSX-FRC plasma, the plasma parameters for SSX-FRC and the Omelchenko simulation are somewhat different:

	Omelchenko Simulation ($s = 12$ case)	SSX-FRC
Peak Density	$0.8 \times 10^{16} cm^{-3}$	$10^{15} cm^{-3}$
Ion Temperature	100 eV	30 eV
Separatrix Radius	11.5 cm	20 cm
Separatrix Length	44 cm	60 cm
O-point radius	8.5 cm	12-14 cm
Alfv‘en velocity	$1.2 \times 10^{7} cm/s$	$6 \times 10^{6} cm/s$
s	12	> 10

6.2 Experimental Setup

Previously, studies of spheromak equilibria [16] and magnetic reconnection [24, 6, 8, 7] were conducted on SSX. The experimental setup was then modified for the SSX-FRC studies. The various components of the SSX-FRC experimental setup are shown in Fig. 30. The plasma dynamics occur inside a 24 inch radius vacuum chamber, which is shown in Fig. 31. Inside the vacuum chamber is a flux conserver with a radius of 8 in and a length of 25 in including a 1 in gap between the two halves of the flux conserver. The relative positions of the flux conserver, vacuum chamber and magnetic probe assemblies are shown in Fig. 28. The lab has four Northstar Research pulsed power supplies, and one power supply is currently connected to each of the two plasma guns. Each power supply has a capacitance of 500 μF and is typically charged to 5 kV. The power supplies each deliver their 6 kJ of stored electrical energy over approximately 20 μs. A separate system supplies power to the stuffing flux coils.

The first step in the creation of the hybrid is the formation of two counterhelicity spheromaks using the coaxial magnetized plasma guns. The spheromak formation sequence is illustrated schematically in Fig. 19. At t=-23.71 ms, the stuffing flux coils are energized. The LC time of this circuit is long enough so that the stuffing flux is approximately constant over the life time of the plasma dynamics, which last for a few hundred microseconds. The polarity of the stuffing flux from each coil is chosen to make either co- or counter-helicity spheromaks (in this paper only counter-helicity spheromaks are considered.) The particular time at which the stuffing flux is triggered was chosen to optimize the level of stuffing flux during the plasma dynamics. The stuffing flux is concentrated by a slug of high permittivity metal at the center of the plasma gun.

At t=-730 μs, approximately half a cubic centimeter of hydrogen at atmospheric pressure (or a maximum of 10^{18} ions or electrons per spheromak) is injected into the annular gap between the inner and outer coaxial cylindrical electrodes (Fig. 19a). High voltage capacitors charged to approximately 5 kV are connected to the electrodes at t=0 (Fig. 19b). The high voltage ionizes the hydrogen and a current flows through the resulting plasma. The plasma current creates an azimuthal magnetic field called the "gun field." The $\vec{J} \times \vec{B}$ interaction between the plasma current and the gun field results in acceleration of the plasma toward the exit of the plasma gun. The plasma encounters the stuffing field at the end of the plasma gun, and because of the frozen-in flux constraint (see MHD section), the plasma cannot move through the stuffing field. The $\vec{J} \times \vec{B}$ force on the plasma causes it to distend the stuffing field (Fig. 19c). When the magnetic pressure from the gun field exceeds the magnetic tension in the stuffing field, the plasma breaks away from the plasma gun and the stuffing field reconnects at the edge of the plasma gun to form a spheromak (Fig. 19d). Because of the frozen-in flux constraint, the spheromak has inherited a toroidal field from the gun field and a poloidal field from the stuffing field. After formation, the spheromak is not in equilibrium. The initial decay state of the spheromaks in SSX can be approximated by the Taylor state (i.e. force free state with constant λ) [16].

The evolution of the two spheromaks to a hybrid with a particular amount of residual toroidal

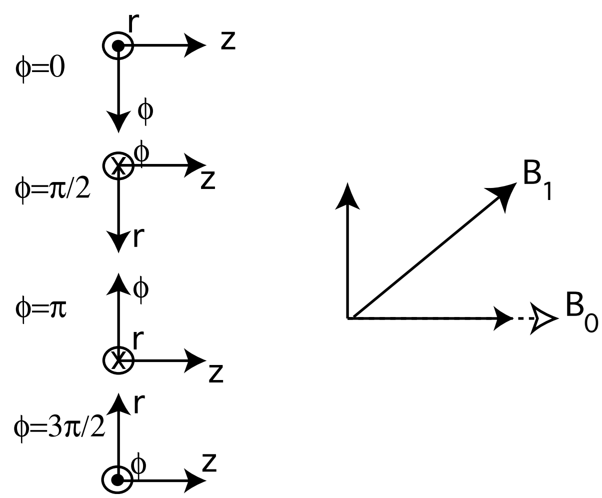

Figure 18: The left panel above shows the directions of the cylindrical basis vectors at intervals of $\frac{\pi}{2}$ in ϕ. The right panel shows the unperturbed axial field B_0 and the perturbed field B_1.

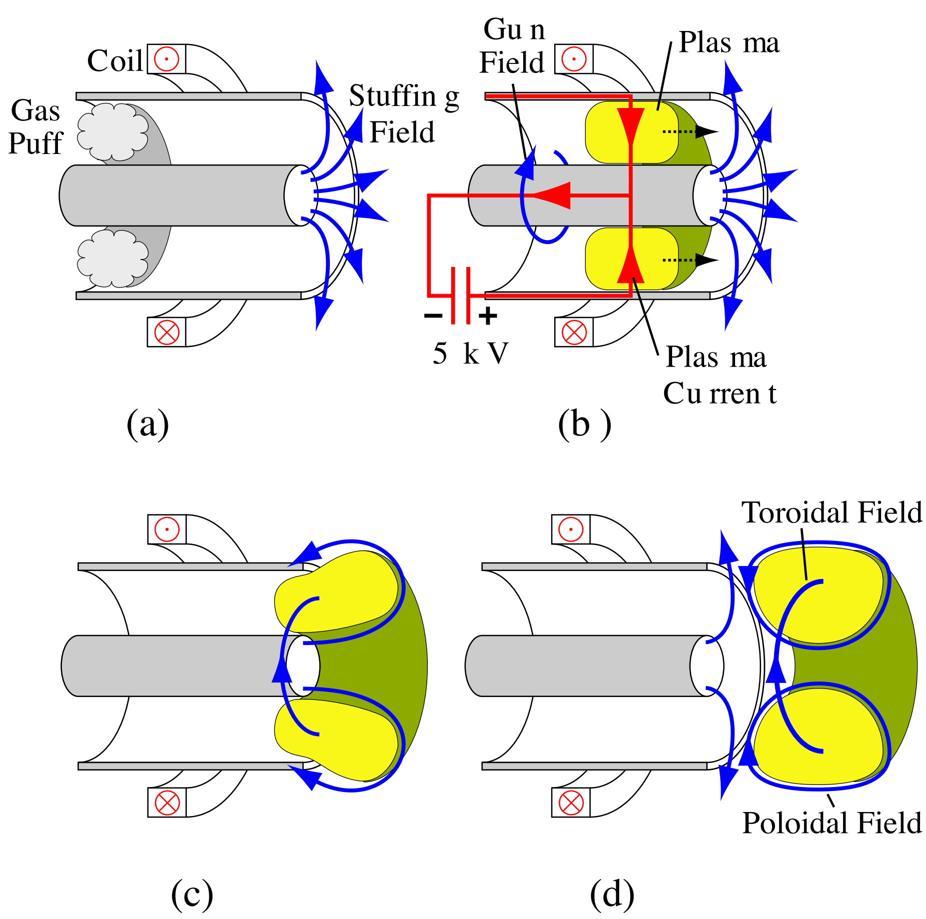

Figure 19: Formation of a spheromak using a magnetized coaxial plasma gun. See text for details.

field is shown in Fig. 20. The spheromaks are counter-helicity and the toroidal component of the magnetic field of one spheromak is anti-parallel to the toroidal component of the magnetic field of the other spheromak. Furthermore, the poloidal fields of the two spheromaks are antiparallel in the midplane region as the spheromaks begin to merge. Since both components of the magnetic field of the two spheromaks are antiparallel, some amount of the magnetic field of each spheromak annihilates with that of the other spheromak. The merging of the two spheromaks is aided by the attractive interaction between the parallel toroidal currents that generate the spheromak magnetic fields. The merging of the two spheromaks is hindered by the external field of midplane reconnection control coils (RCC's). The principles and structure of the RCC's are elaborated on below.

6.3 Magnetic Probes

The magnetic field dynamics in SSX-FRC were measured with an array of magnetic probes distributed throughout the plasma. The probes were wound by the author during the months preceding Summer 2002, during which FRC magnetics data was first taken. Such probes measure the change in magnetic field with respect to some reference time. A schematic of a magnetic probe is shown in Fig. 21. The probe is simply a coil of thin wire with several turns. The operating principle is based on Faraday's law:

$$\oint \vec{E} \cdot d\vec{l} = -\dot{\phi}. \tag{150}$$

Integrating along the path of the wire in the magnetic probe yields

$$V_{ab}(t) = -\dot{\phi}, \tag{151}$$

where V_{ab} is the EMF between the two leads of the magnetic probe.

The magnetic probes were designed to be small enough so that in the experiment the gradient in the magnetic field across the area linked by the probe is small. Therefore, the flux can be approximated as the magnetic field normal to the area linked by the coil times the area of the coil, and Eq. 151 becomes

$$V_{ab}(t) = -\dot{B}_n AN, \tag{152}$$

where B_n is the magnetic field normal the coil area, A is the area of the coil and is the number of turns in the coil. Integrating the previous equation yields

$$B_n(t) = B_n(0) - \frac{\int_0^t V_{ba}(t)dt}{AN}. \tag{153}$$

Orienting three of these magnetic probes in three perpendicular directions yields the entire magnetic field vector at the location of the probe, as long as the magnetic field does not change much over the extent of the triple probe.

For the SSX-FRC experiment, 12 inch long, $\frac{3}{16}$ inch diameter Delrin rods were used as probe forms for the magnetic probes. Eight sets of three orthogonal magnetic probes were wound onto each rod. Each probe in a set of three was oriented in one of three mutually perpendicular directions: r, θ and z (see Fig. 22). In designing magnetic probes, one must obtain a balance between spatial resolution, which decreases with the extent of the probe, and signal magnitude, which increases with the diameter and number of turns of the coil. Thin (# 34) magnet wire was used to fit a large number of turns into a small area. The area linked by the circular r coils and the rectangular θ and z coils differed due to the design of the Delrin rods. Since, as can be seen from Eq. 152, a decrease in area can be compensated for by an increase in number of turns, the number of turns in

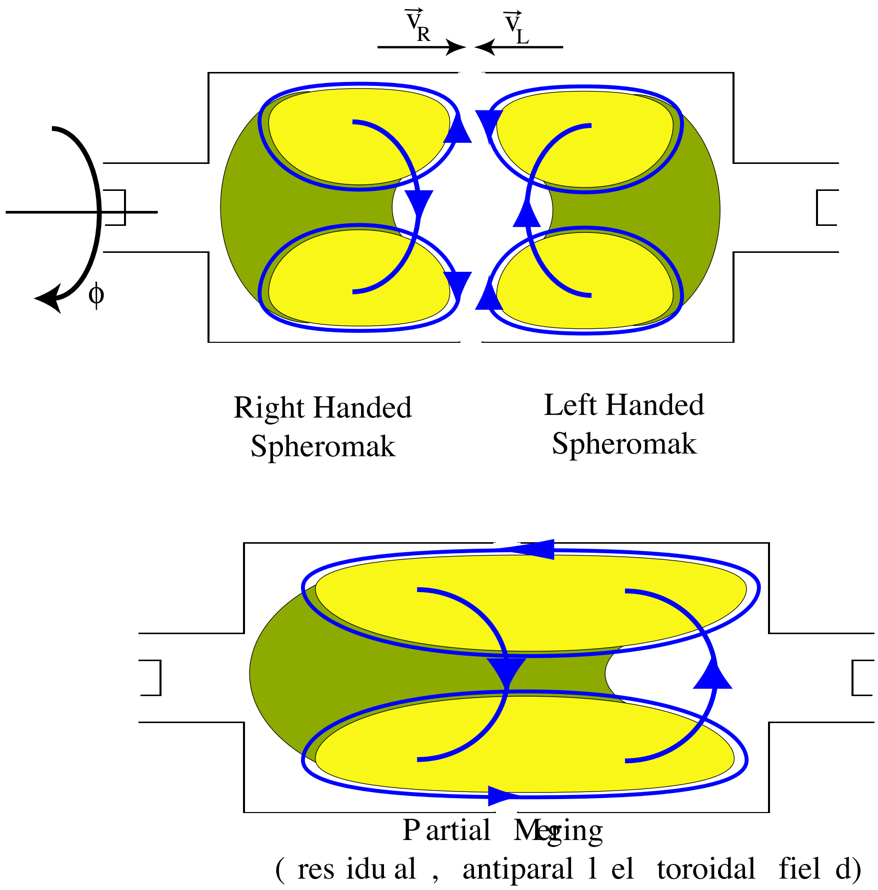

Figure 20: Two counter-helicity spheromaks are merged to create a hybrid with a particular amount of residual anti-parallel toroidal field.

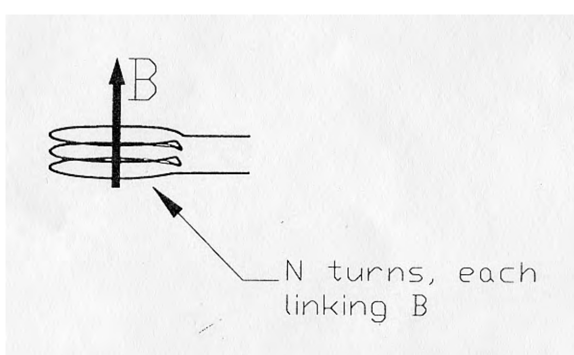

Figure 21: A magnetic probe. The voltage induced across the leads of the coil is equal to the negative change in flux through each turn of the coil. Figure taken from Bellan (2000).

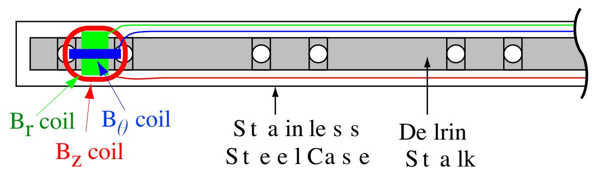

Figure 22: A schematic of a portion of a magnetic probe stalk in its housing.

the circular and square coils were chosen to yield a nearly equal signal for a given rate of change in the magnetic field. The properties of the magnetic coils are summarized in the table below:

Orientation	Shape	Single turn area	Num of Turns	Total area
theta, z	rectangular	0.070 sq in	6	0.420 sq in
r	circular	0.028 sq in	15	0.414 sq in

Photos of the probe stalks are shown in Figs. 23 and 24. Note that the pair of leads extending from each probe is twisted. The leads are twisted to eliminate any extraneous induction due to flux linked by the leads. After all 24 probes were wound on the Delrin rod and the leads were twisted, the ends of the magwire were stripped of their enamel and the ends were soldered into 50 pin connectors, as shown in Fig. 25. Each probe stalk was then wrapped with Teflon tape in order to hold the probe leads in place and provide protection to the leads when sliding the probe stalk into its housing. The Teflon tape also decreases the friction when sliding the probe stalk into its housing. A photo of a Teflon wrapped probe stalk is shown in Fig. 26. As shown in Fig. 27, a fiducial pin was inserted into the Delrin rod parallel to the θ probes in order to roughly align the probes when inserting them into their housings. Departures from perfect alignment were accounted for in a calibration procedure, discussed below.

Stainless steel probe housings were fabricated for the probe stalks. To fabricate each housing, a $\frac{1}{4}$ inch diameter stainless steel tube with a 0.006 inch thick wall was welded onto a conflat flange assembly (see Figs. 28 and 29). Twenty complete probe assemblies were built. The SSX-FRC vacuum chamber can accommodate all twenty in the configuration shown in Fig. 30. Probe stalks were installed in three planes along the axis of the cylindrical vacuum chamber. The end planes can have eight probe stalks each, whereas the center plane can have only four due to the large ports in the vacuum chamber located at 90 degree angles from one another. For this paper, data is based on four probes at each of the three planes.

6.4 Data Acquisition

Once the probes were inserted into the vacuum chamber, fifty channel cables were connected to the fifty pin connectors on the probe housing and to a circuit board in the screen room (see Fig. 31). Each of the fifty channels consists of an individually shielded twisted pair. Only 48 channels were used since there are 24 probe coils on each probe stalk. Recall that the voltage induced across the probe leads is equal to the negative time derivative of the flux linked by the probe (Eq. 151). Active integrators were employed to integrate the signal from each probe to obtain the magnetic field at each point in time. The signals from eight probes are multiplexed together at 10 MHz and the multiplexed signals are fed to a bank of ten eight-channel digitizers operating at 10 MHz [26]. Since the signal of each probe is sampled every eight cycles of the digitizer, the effective time resolution of the magnetics is 0.8 μs. After a run of the experiment, the multiplexed data is downloaded along with other diagnostics data from oscilloscopes to a Mac G3 running a LabView vi. The magnetics data is de-multiplexed and the calibration matrix is applied using an IDL code. Approximately 10% of the magnetic probes shorted to the housing because of the tight fit when

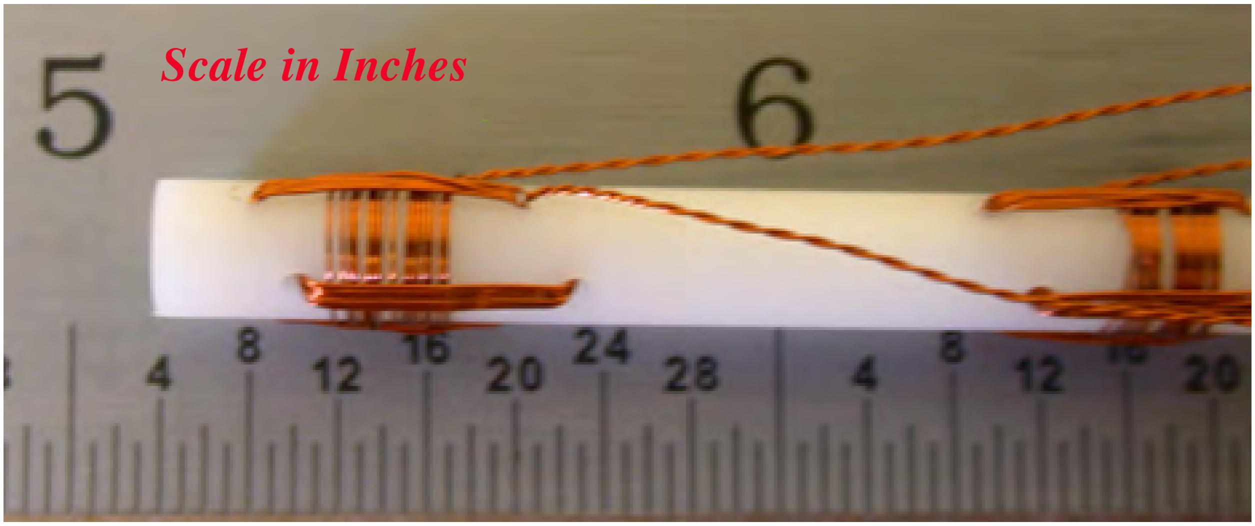

Figure 23: Close up of a triple probe wound onto a Delrin rod. Although the design of the probes drew on previous experience with magnetics instrumentation in SSX, these probes were fabricated specifically for the SSX-FRC experiment.

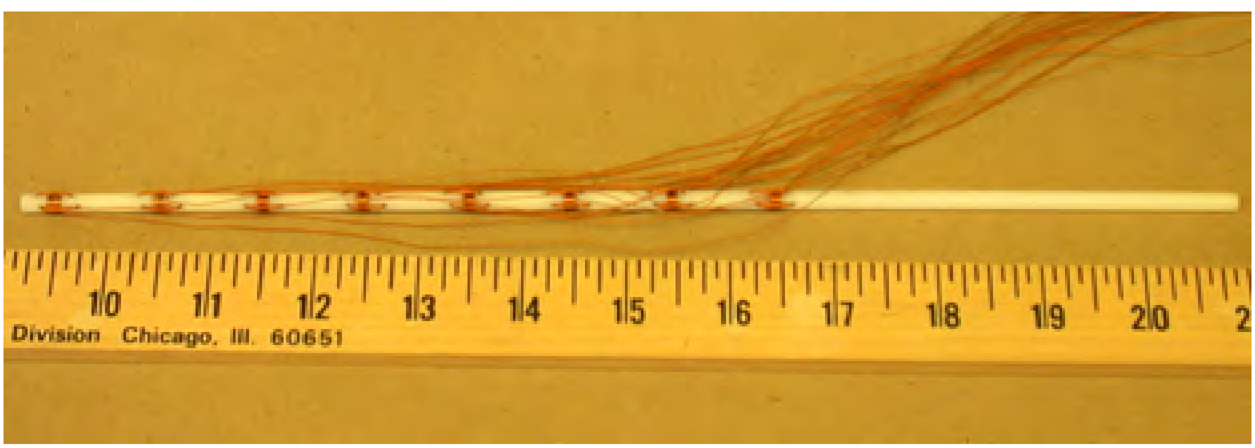

Figure 24: A wide angle view of eight triple probes wound onto a Delrin rod.

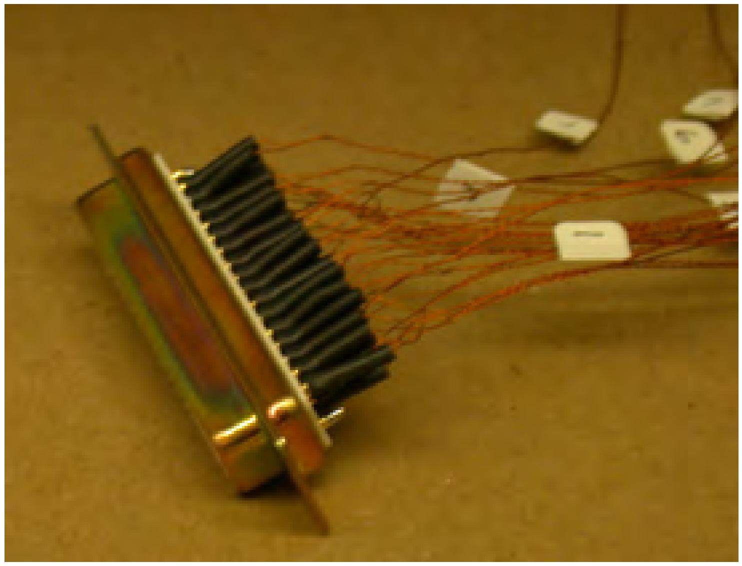

Figure 25: Magnetic probe leads from a probe stalk attached to a 50 pin connector.

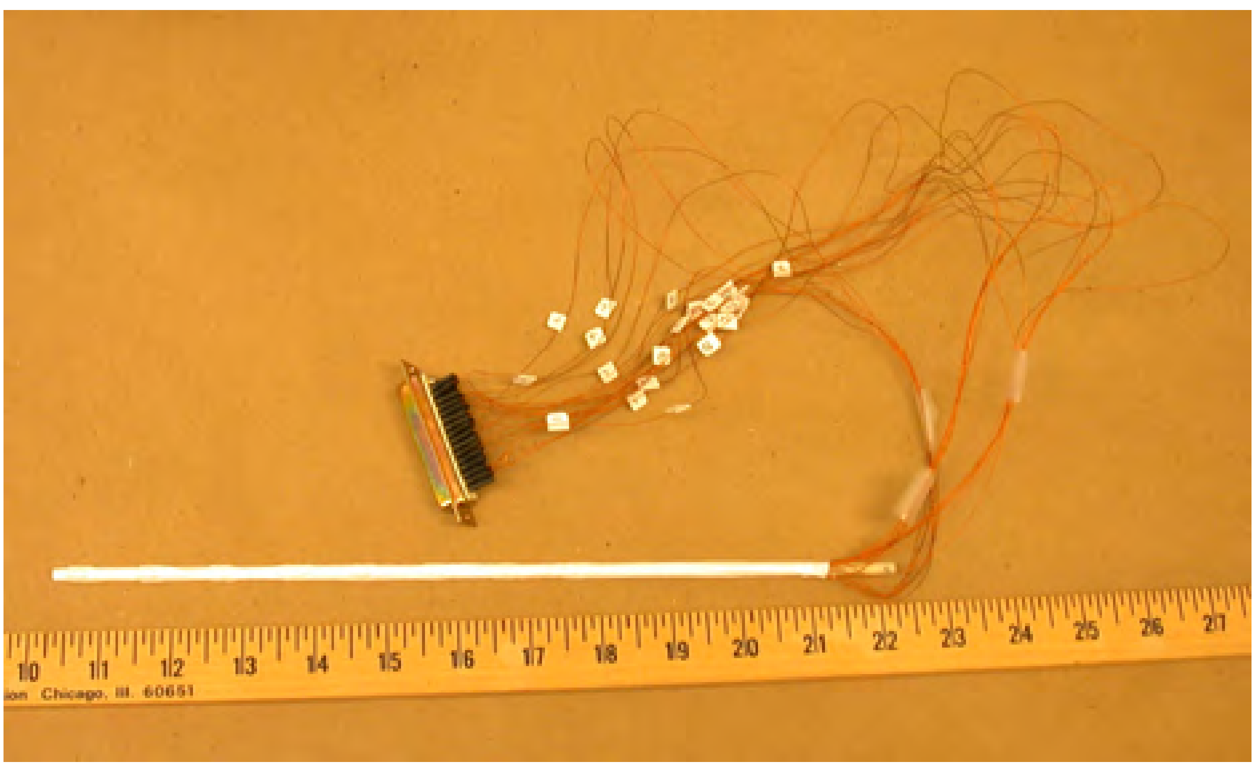

Figure 26: Photo of a probe stalk wrapped with Teflon tape for protection.

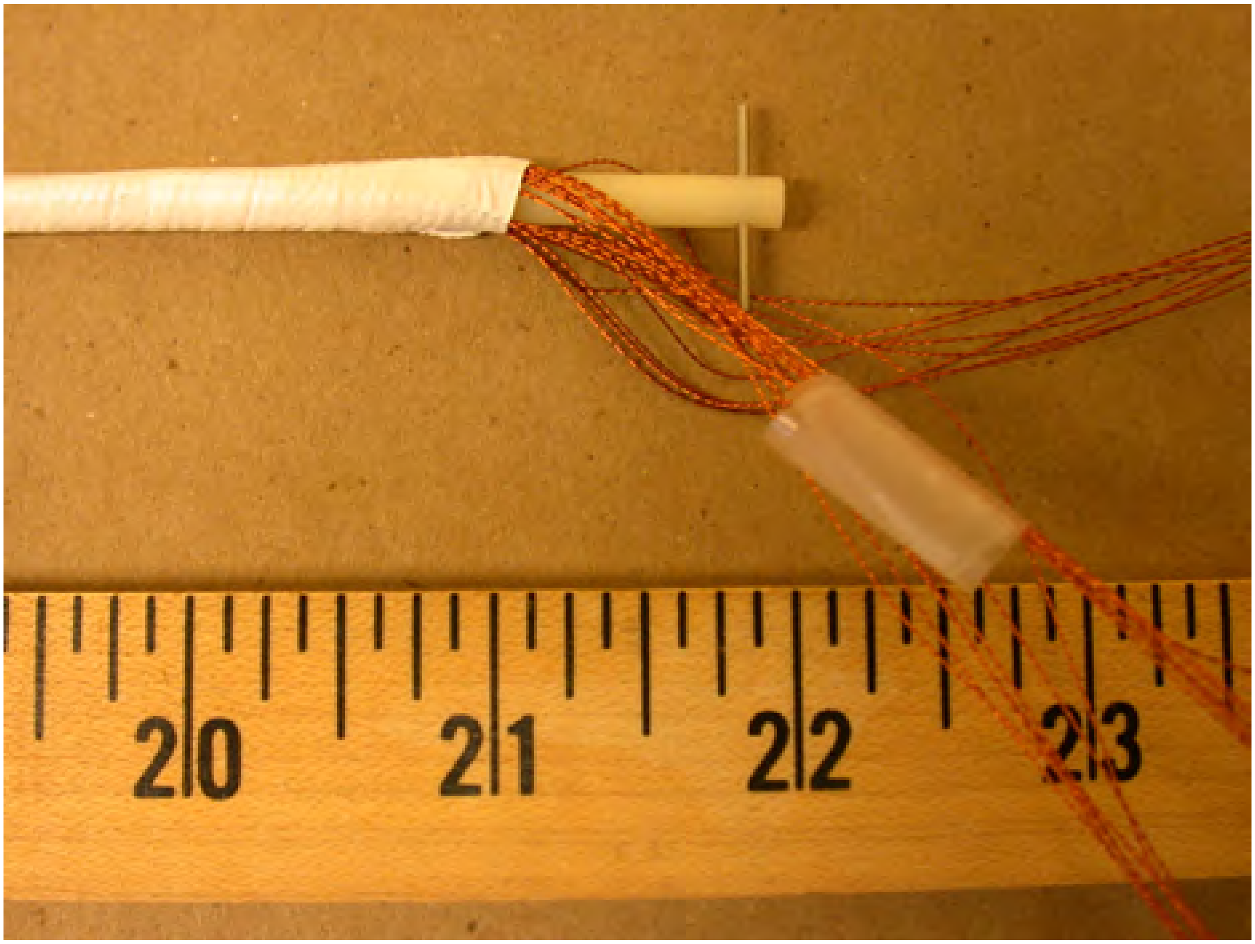

Figure 27: A fiducial pin was inserted into the probes for rough alignment when inserting the probes into their housing.

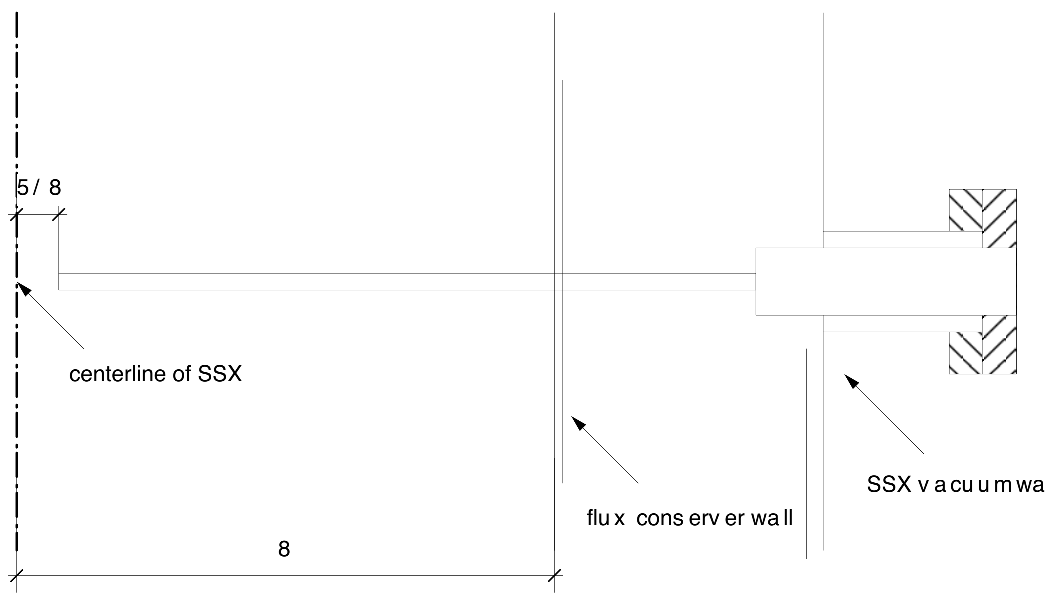

Figure 28: Schematic of a stainless steel magnetic probe housing.

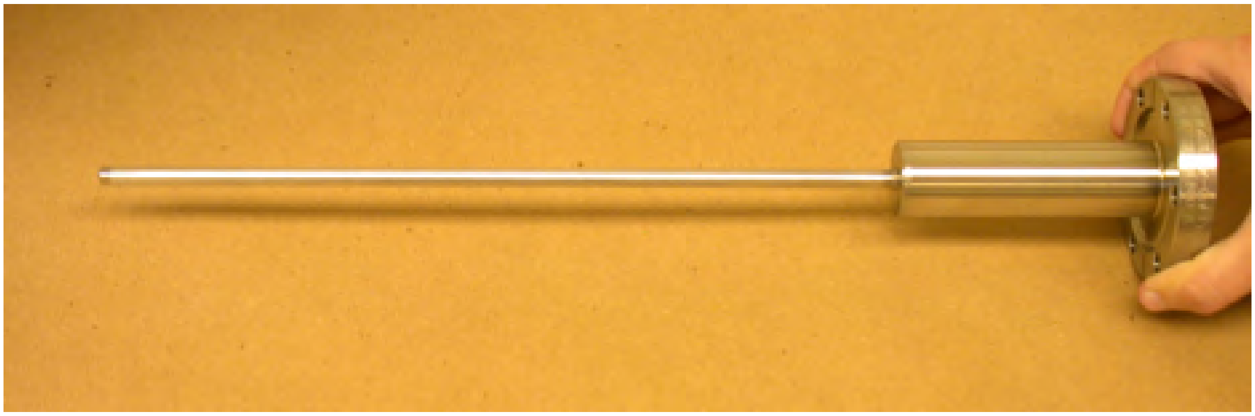

Figure 29: Photo of a stainless steel magnetic probe housing.

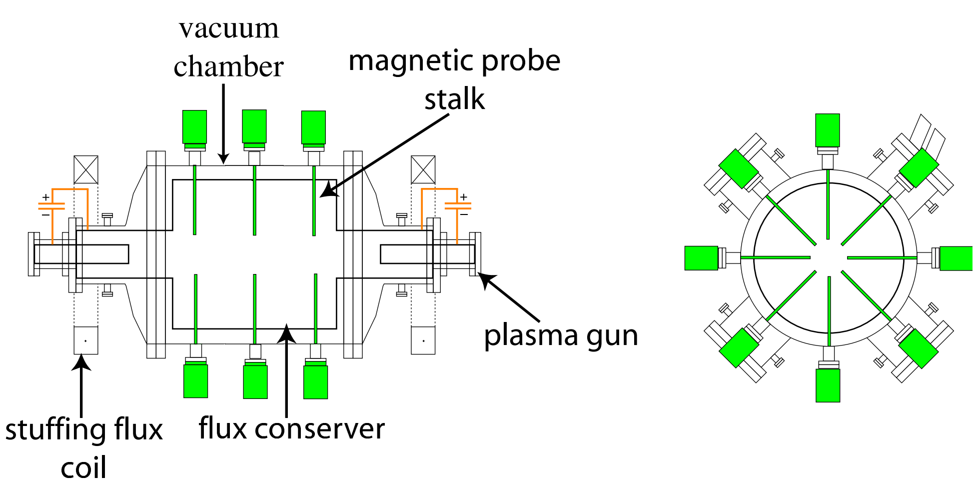

Figure 30: Schematic showing the placement of twenty probe assemblies, each with 24 magnetic probes.

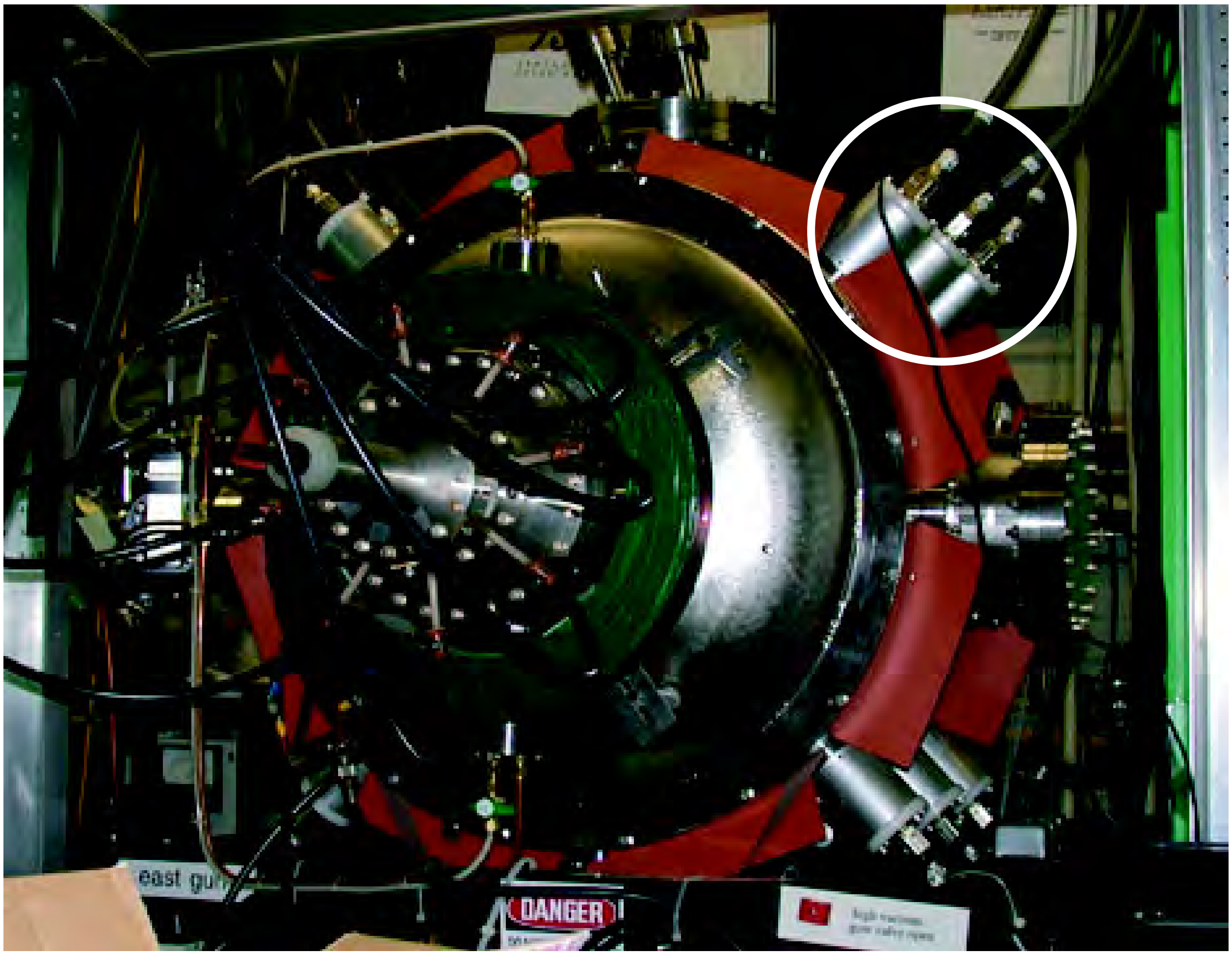

Figure 31: Photo showing the placement of twelve of the magnetic probe assemblies and the grey cables transmitting the magnetics data from the probe housing to the screen room. Three of the probe assemblies are circled in white.

inserting the probe stalk in the housing. The magnetic field was interpolated using an IDL code to obtain approximate values of the magnetic field at the locations of the shorted probes.

6.5 Reconnection Control Coils

The Reconnection Control Coils (RCC's) were a major addition to the Swarthmore Spheromak Experiment. A large part of the work involved in building the RCC's was done by the author. Before the RCC's were installed, the reconnection of the spheromaks was limited using copper plates at the midplane. At first, only two chevrons were cut out of the plates and local reconnection was studied. Then all of the plates were cut out except for a narrow annulus near the boundary. Eddy currents induced in the annulus were thought to limit reconnection in much the same way as the RCC's do in the present configuration.

The RCC's are a pair of pulsed electromagnets external to the plasma that were installed near the midplane of the SSX vacuum chamber. The repulsion between the RCC current and the toroidal current in the FRC limits the extent to which the two spheromaks merge, thereby increasing the amount of residual toroidal field in the spheromak/FRC hybrid. The mutual repulsion between the currents also adds good curvature to the hybrid. The concave shape of the plasma boundary near the midplane is called "good" because thermal motion of the plasma particles parallel to the magnetic field lines along the boundary results in a centrifugal force that is directed towards the axis of the flux conserver. Schematics of the reconnection control coils (RCC's) are shown in Figs. 32 and 33. A circular trough was built out of $\frac{1}{8}$ inch thick stainless steel to house the RCCs. (Fig. 34). The stainless steel of the housing is thin enough that the soak time for the magnetic flux through the stainless steel walls is short compared to the rate of change of the magnetic flux of the RCC. The walls of the trough were covered with several strips of insulating Kapton tape. (Fig. 35) Kapton has a high heat tolerance, which was important since the fourth wall of the RCC housing was welded onto the housing with the copper coil *in situ*.

The RCC was constrained to the center of the trough by periodically placed Teflon strips affixed to the sides of the trough with double stick Kapton tape (Fig. 36). Before a long strip of $\frac{1}{32}$ inch thick copper was wound into the trough, a "U" shaped piece of copper was soldered onto the end of the copper strip and covered with Kapton tape (Fig. 37). The "U" shaped piece was then placed in a groove in the stainless steel trough and the subsequent turns of the copper strip were laid over it (Fig. 38). As the copper was wound into the trough, 0.003 inch thick Kapton tape was applied to one side of the copper strip for electrical insulation (Fig. 39). A photo of the fully wound copper coil is shown in Fig. 40. As is shown in Fig. 38, the ends of the "U" shaped piece extended above the stainless steel housing. The ends of the "U" were bent down and a black Teflon coated wire was crimped and soldered onto each end of the "U" (Fig. 41). A white Teflon coated wire was soldered to the other end of copper strip. These three wires are for current input and output. After all 50 turns were wound into the trough, ceramic matting with a very high heat resistance was inserted in the gaps between the sides of the copper turns and the trough wall (Fig. 42). Additional ceramic matting was laid on top of the copper coil (Fig. 43). A photo of one of the two finished RCC's is shown in Fig. 44.

The completed RCC's were cleaned and installed in the SSX vacuum chamber as shown in Figs. 45 and 46. A photo of the capacitor bank and accompanying circuit used to pulse the RCC's is shown in Fig. 47. The circuit is similar to the one used to ionize the gas that becomes a spheromak. The schematic for the RCC power supply circuit is shown in Fig. 48.

In order to accurately determine the resistance and inductance of the circuit, the current waveform of the RCC's was measured using a 1 mΩ shunt resistor. The current waveform for the case when the flux conservers are not in place is plotted in Fig. 49. The early part of this current waveform was then fit to an analytical expression for the current in an LRC circuit. The measurement was made without the flux conservers in place to remove the complication of flux exclusion by the highly conductive flux conservers. The data and the analytical function with optimized parameters are plotted in Fig. 50. It was found that the resistance of the RCC circuit is 0.2 Ω and the inductance is 6.5 mH. These values are accurate to within 10 percent. The capacitance could not be accurately measured by fitting the current waveform. However, the capacitances of each of the capacitors visible in the photo in Fig. 47 are known to be 10 mF. Since the capacitors are all in parallel, they add to a total capacitance of 0.5 F.

The vacuum magnetic field within the flux conserver volume due to the RCC's was calculated numerically using the law of Biot-Savart and approximating the RCC's as having an infinitesimal area. The vacuum magnetic field due to the RCC's is shown in Fig. 51 for arbitrary current. The magnitude of the vacuum field scales linearly with current. The highly conductive flux conservers exclude the magnetic field from the plasma region for a characteristic time $\tau_{conserver}$. One of the components of the magnetic field was measured with a Hall probe at a location near the RCC's as shown in Fig. 45. The measurement was made with and without the flux conservers. The current and magnetic field waveforms are shown in Figs. 52 and 53. The magnetic field is nearly proportional to the current in the case without the flux conservers (Fig. 52). On the other hand, an offset between the current and the magnetic field is visible in the case with the flux conservers (Fig. 53) as expected. The plasma dynamics in SSX-FRC take place on the time scale of a few hundred microseconds whereas the RCC pulse lasts for about half a second. Therefore, the RCC field does not change significantly during the plasma dynamics and can be approximated as constant. Furthermore, the plasma formation is timed to take place several $\tau_{conserver}$ intervals after the start of the RCC pulse so that the magnetic field can penetrate the flux conservers.

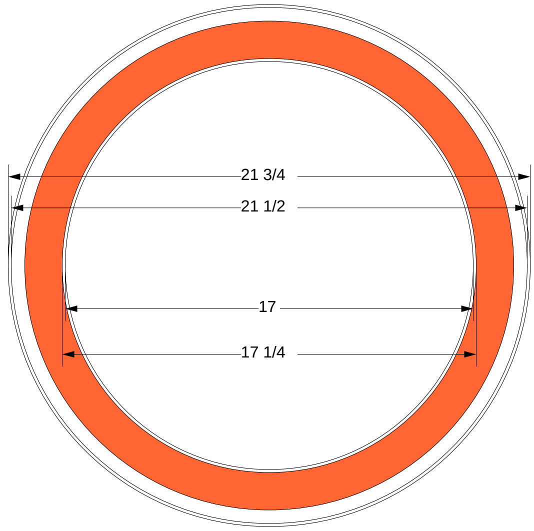

Figure 32: Side view of one of the reconnection control coils. 50 turns of a $\frac{1}{32}$ inch thick copper strip were wound in a stainless steel trough.

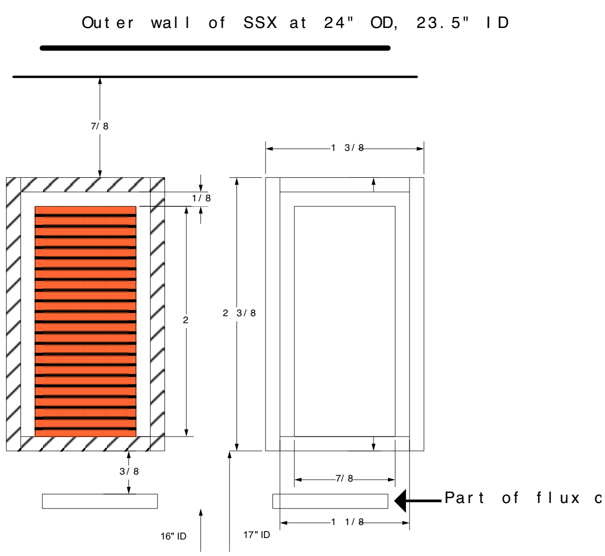

Figure 33: Partial cross section of SSX-FRC with reconnection control coils installed. The figure shows the relative placement of the two RCCs, the flux conservers, and the wall of the vacuum chamber. The placement of the RCCs along the axis of the chamber can be modified.

Figure 34: Photo of the circular trough built to house the reconnection control coils.

Figure 35: Photo of the inside of the stainless steel reconnection control housing covered with insulating Kapton tape. A Teflon positioning strip is also visible.

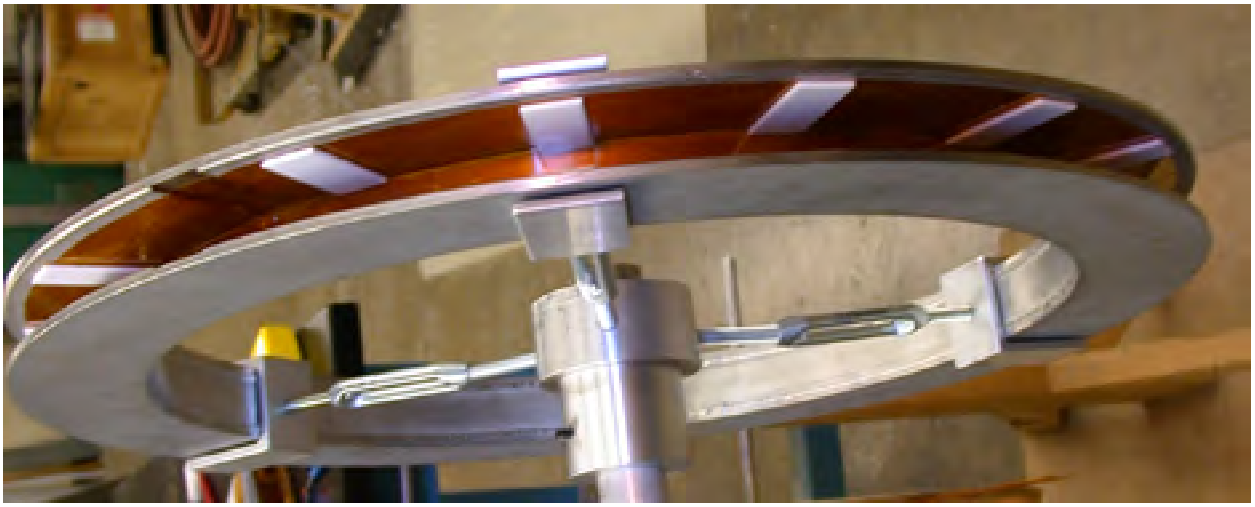

Figure 36: Photo of the inside of the stainless steel reconnection control housing with periodically placed Teflon strips.

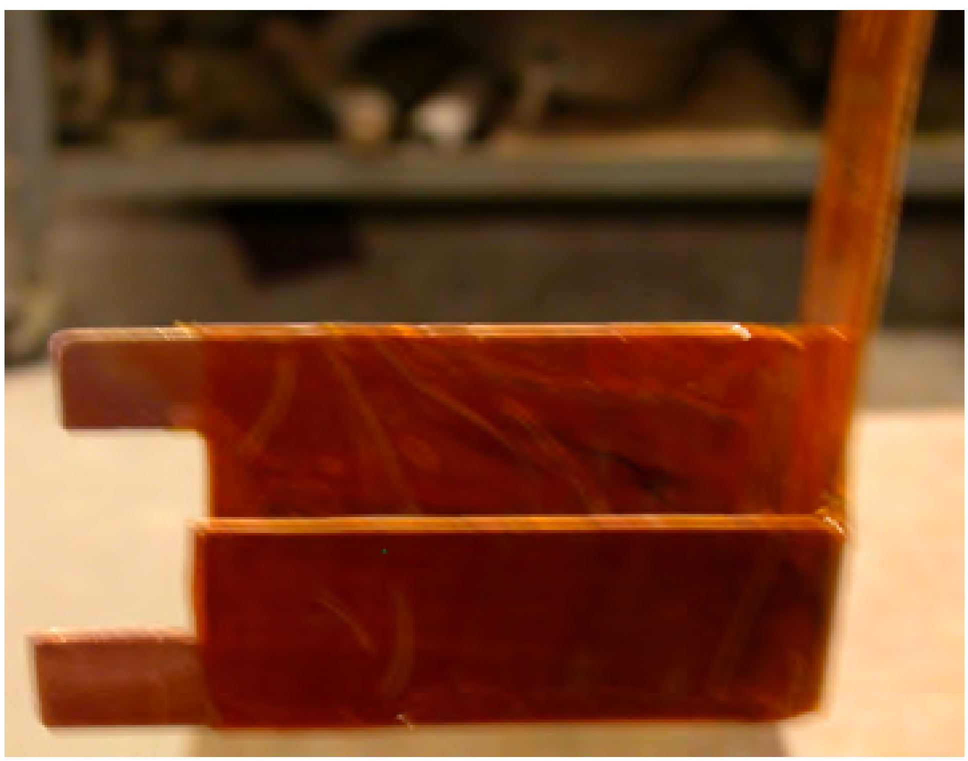

Figure 37: Photo of the “U” shaped piece soldered onto the end of the copper strip.

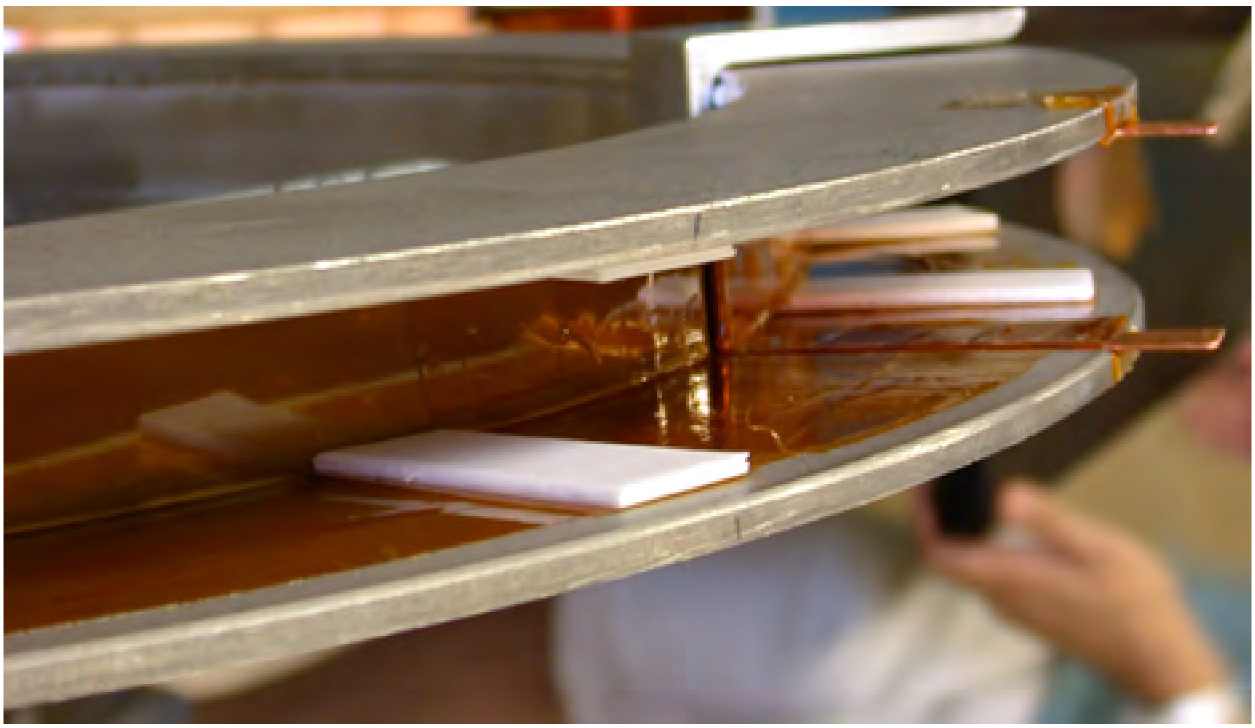

Figure 38: Photo of the “U” shaped piece soldered onto the end of the copper strip in place in the trough.

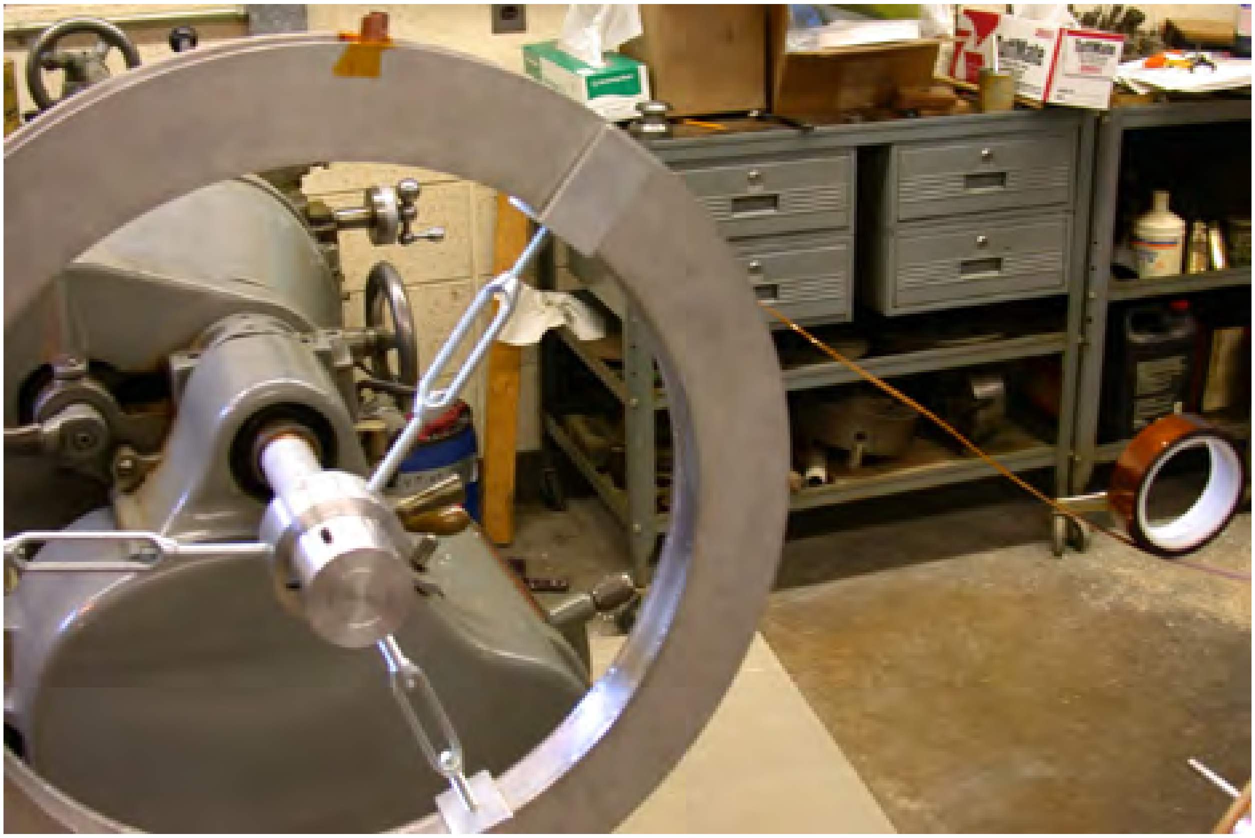

Figure 39: As the copper was wound into the trough, 0.003 inch thick Kapton tape was applied to one side of the copper strip for electrical insulation.

Figure 40: A fully wound reconnection control coil.

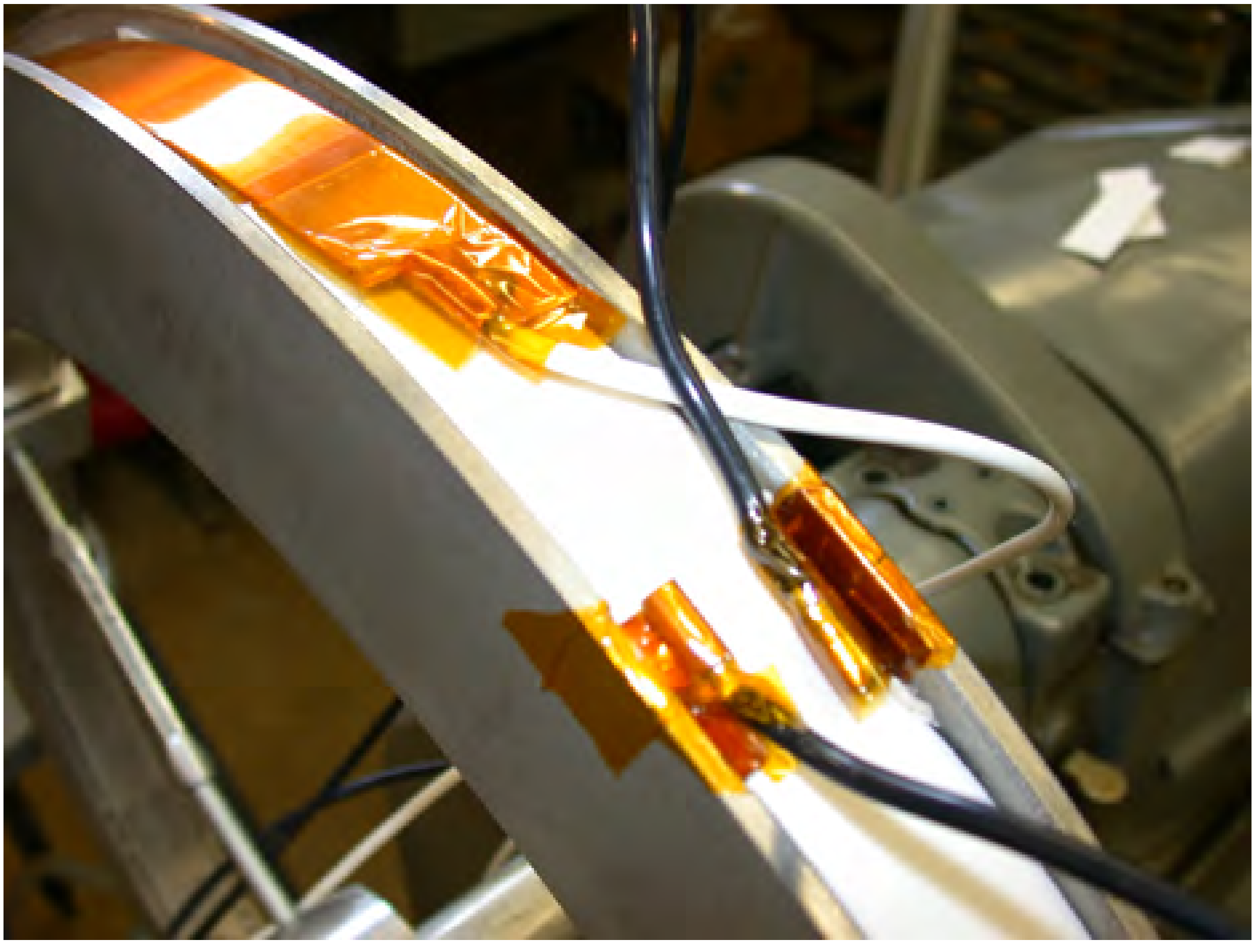

Figure 41: Wires were crimped and soldered onto the ends of the copper coil for current input and output.

Figure 42: Insulating ceramic matting was inserted on the sides of the copper coil.

Figure 43: Insulating ceramic matting was laid on top of the copper coil.

Figure 44: A photo of one of two finished reconnection control coils.

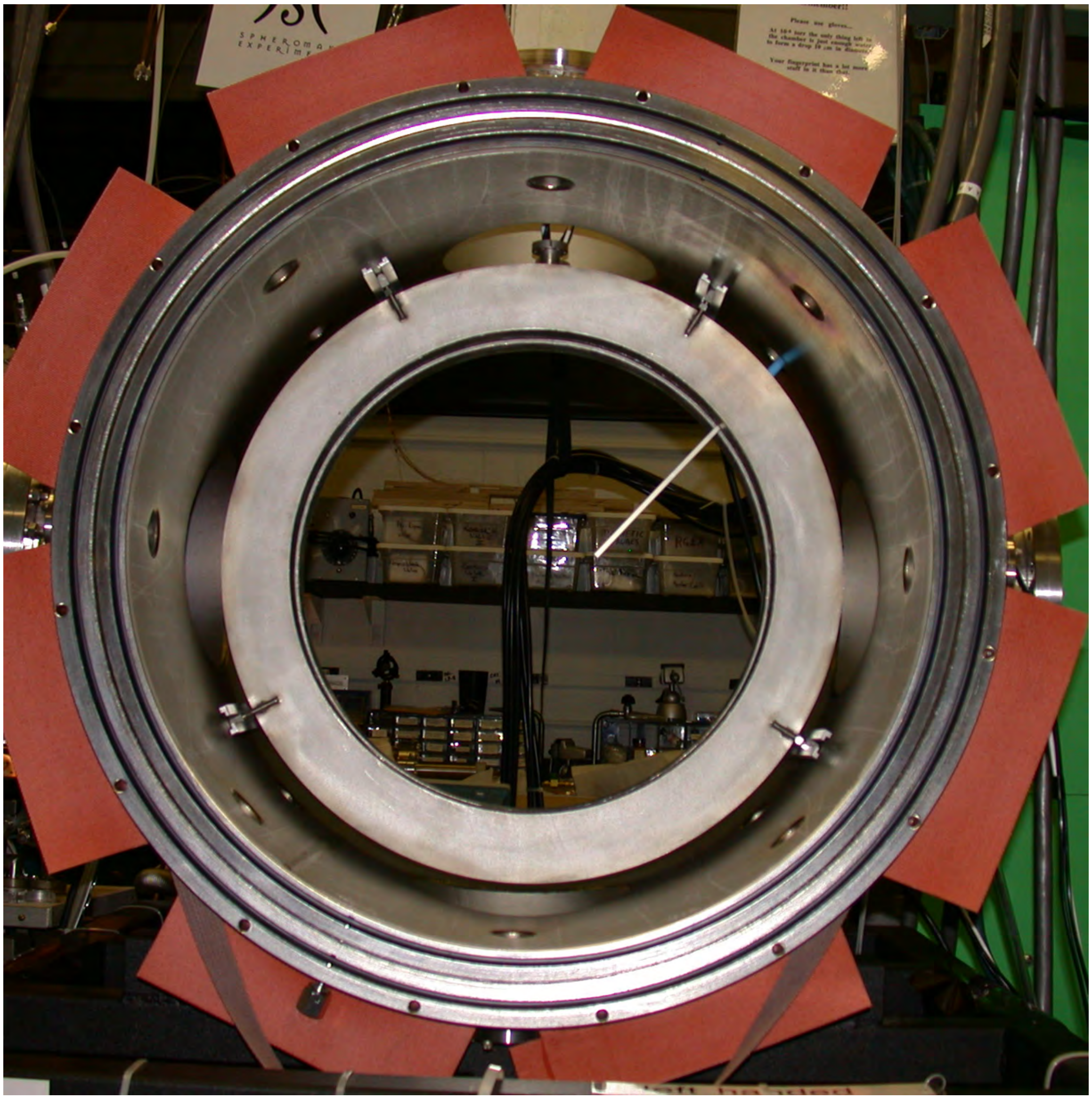

Figure 45: A photo of the RCC's installed in the vacuum chamber. A Hall probe is protruding into the field region of the RCC's.

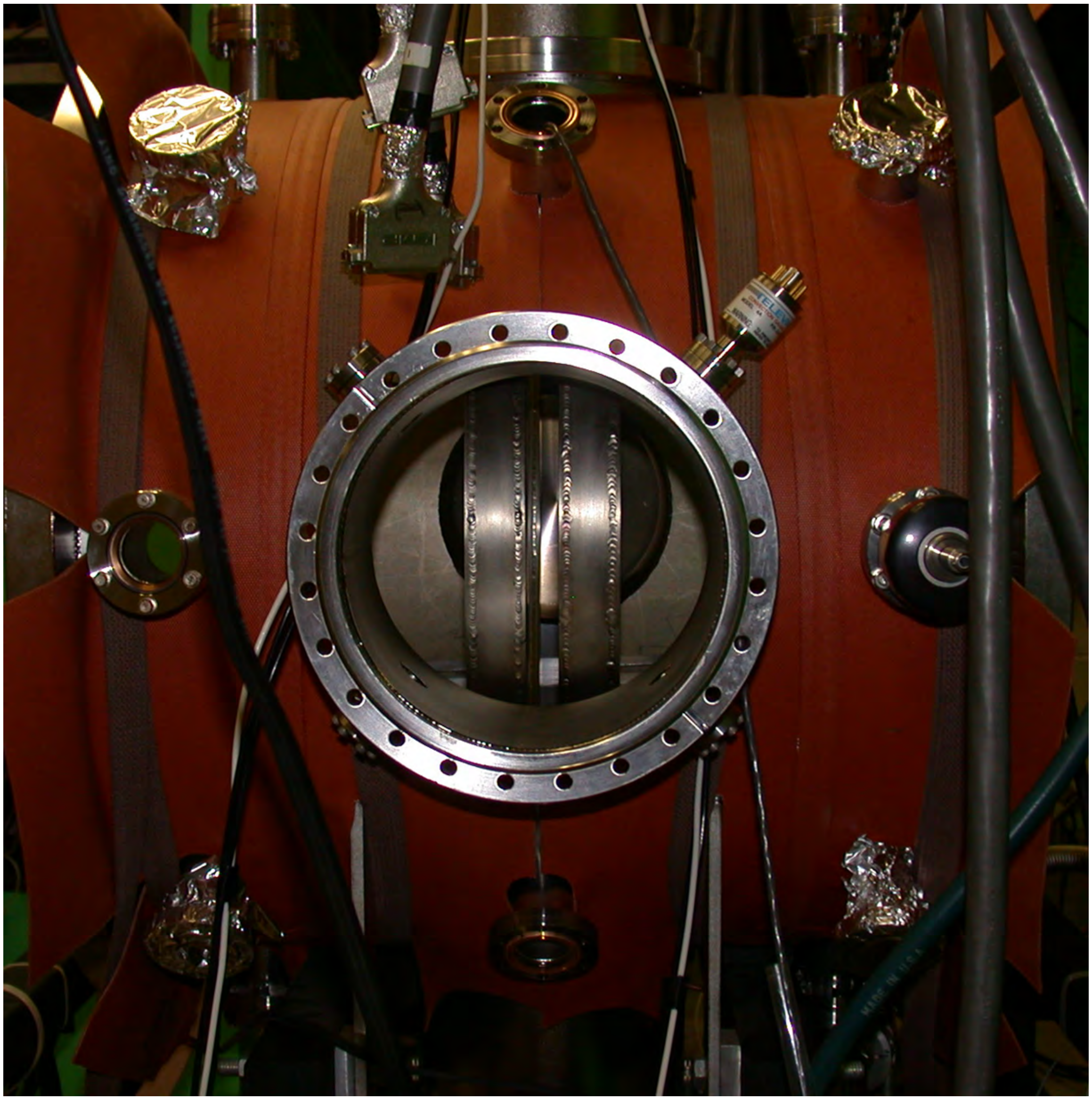

Figure 46: A side view of the reconnection control coils installed in the SSX vacuum chamber.

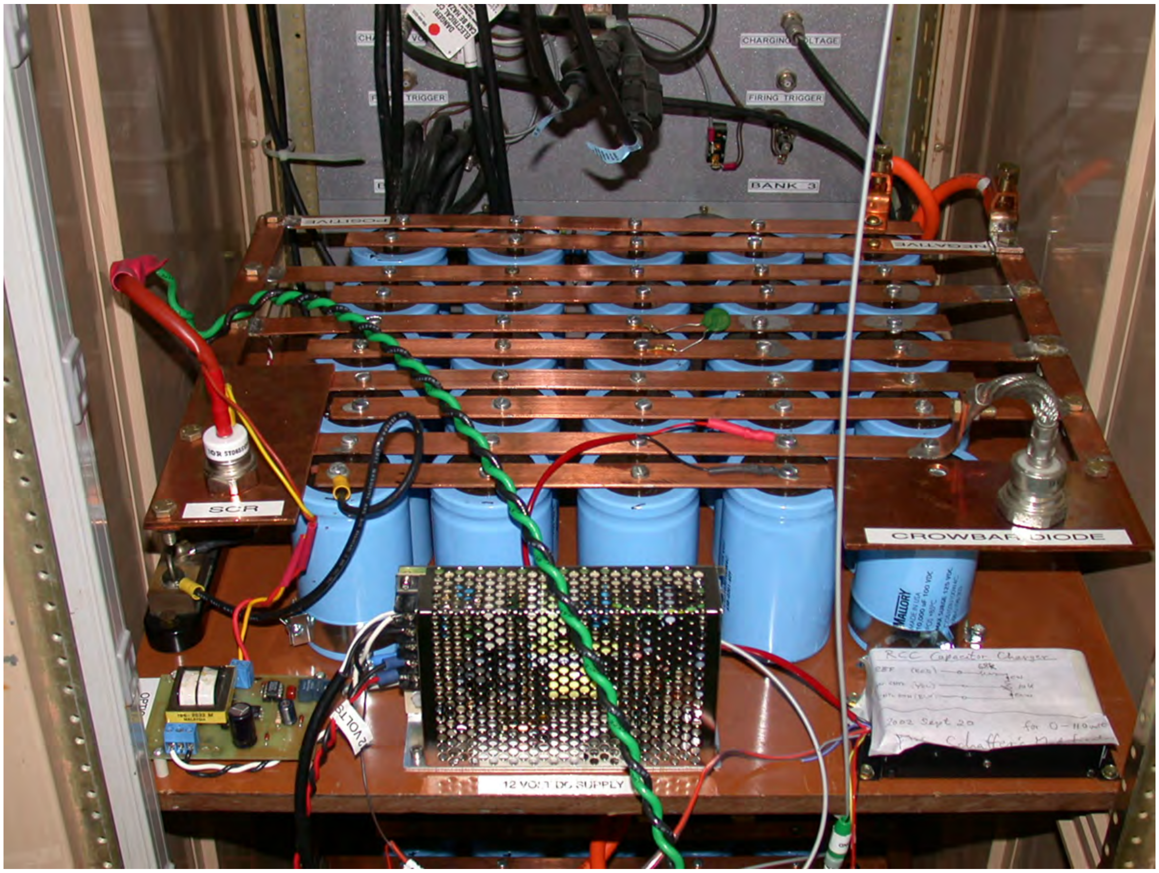

Figure 47: One of the two RCC capacitor banks. The capacitors (blue cylinders) linear charging power supply (metal box, front center) and optoelectonic converter (front left) are visible.

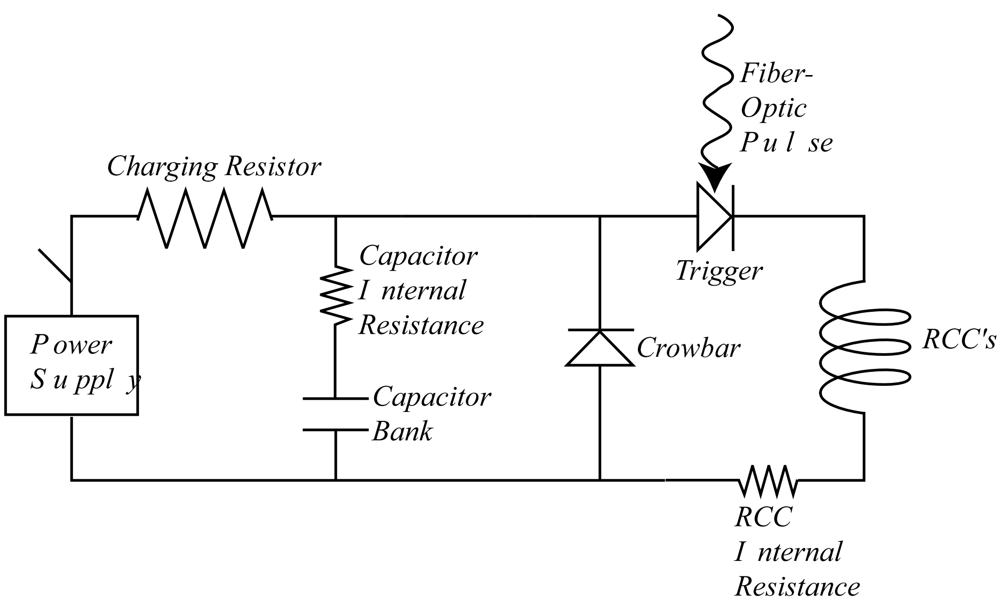

Figure 48: A circuit diagram for the RCC's and their power supply.

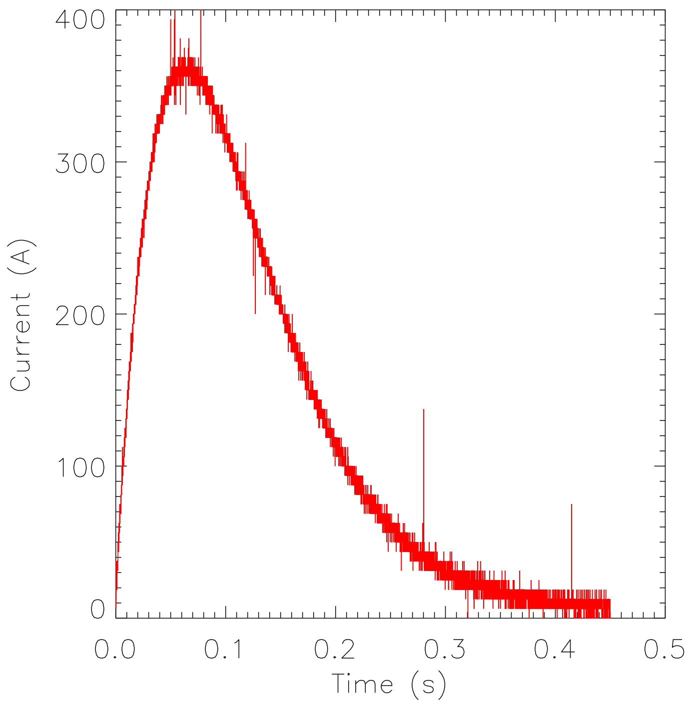

Figure 49: The current in the RCC's is plotted as a function of time. The initial voltage is 100 V.

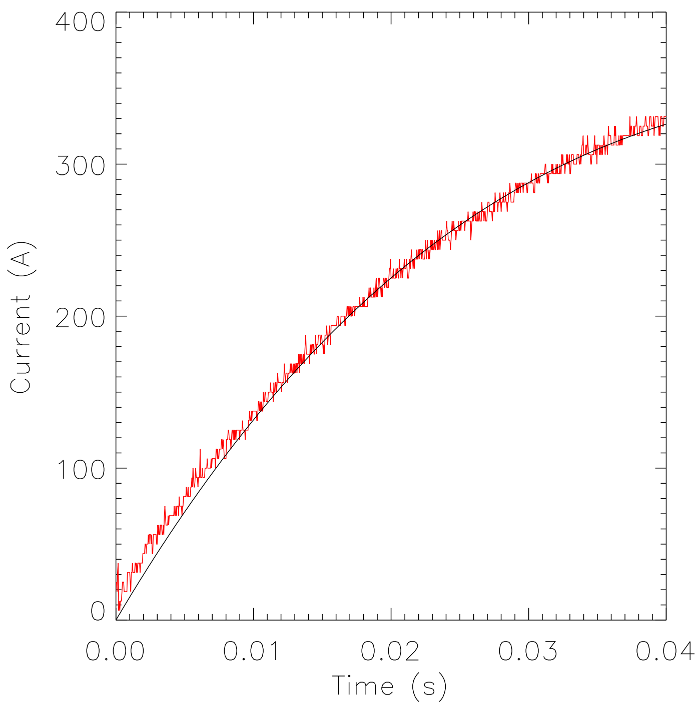

Figure 50: The measured current in the RCCs during the initial part of the pulse is shown. The analytical function with parameters optimized to fit the data is superimposed. It was found that the RCC circuit has a resistance of 0.2 Ω and an inductance of 6.5 mH to within 10 percent.

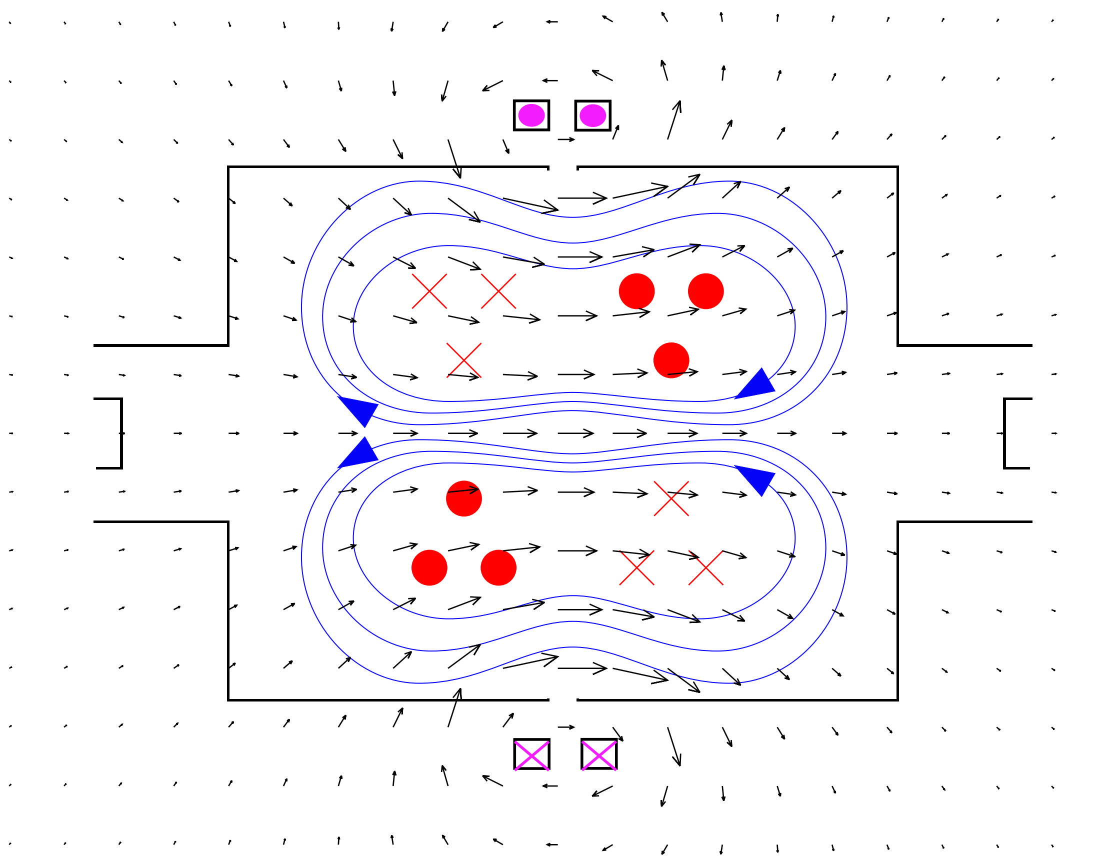

Figure 51: The vacuum magnetic field produced by two current carrying hoops of infinitesimal cross-section with dimensions approximately those of the RCC's. Also shown are the flux conservers and an artistic rendition of the FRC field lines.

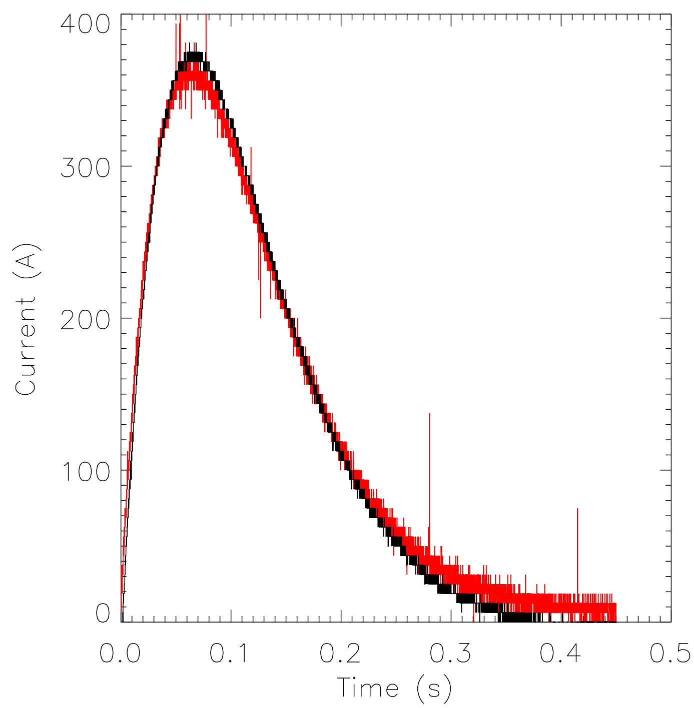

Figure 52: A plot of one component of the magnetic field at a location near the RCC's and the RCC current waveform in the case without the flux conservers. The magnetic field is nearly proportional to the current, as expected.

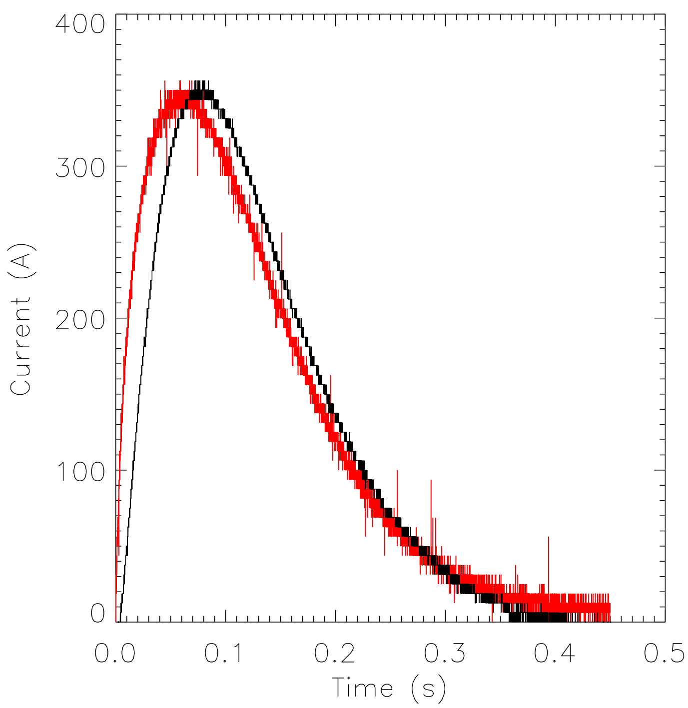

Figure 53: A plot of one component of the magnetic field at a location near the RCC's and the RCC current waveform in the case with the flux conservers. There is a temporal offset between the magnetic field and the current due to the effect of the highly conductive flux conservers.

6.6 Grad-Shafranov Equilibrium Solver

A Grad-Shafranov equilibrium solver written by J. A. Leuer of General Atomics was used to compare magnetics data with different Grad-Shafranov equilibria [38]. The form of the Grad-Shafranov equation used in the code is

$$-R^2\mu_0 p' - ff' = -\mu_0 R J_\phi. \tag{154}$$

Pressure p and poloidal current $f = RB_\phi$ are functions of the poloidal flux ψ, and $'$ means $\frac{d}{d\psi}$. The above equation is solved using the finite element partial differential equation tools in Matlab. The computational domain is bounded by a right circular cylinder flux-conserver, and symmetry is imposed about the midplane. A set of specified current loops impresses a frozen flux into the conserver, including the flux due to the stuffing coils and the reconnection control coils. Equilibria are generated by specifying the dependences of p' and ff' on ψ: $p' \propto \psi^{pexp}$ and $ff' \propto \psi^{fexp}$ inside the bounding separatrix (the separatrix is at $\psi = 0$), and $p = f = 0$ outside it. The parameter bp, called the "beta" parameter, is used to specify the relative weights of p' and ff' in the Grad-Shafranov equation. The Grad-Shafranov solver has been used to compare measured and simulated flux profiles as discussed below in the results section.

7 Results

According to the principles of Fourier analysis, any function of θ can be expanded in the form

$$f = c + a_1 \cos\theta + b_1 \sin\theta + a_2 \cos 2\theta + b_2 \sin 2\theta + ... \tag{155}$$

The constant multiplying θ in the above equation is the mode number, m. If the function is evaluated at intervals of $\frac{\pi}{2}$ and we consider only the m=0 and m=1 terms, we obtain

$$f(0) = c + a_1 \tag{156}$$
$$f(\frac{\pi}{2}) = c + b_1 \tag{157}$$
$$f(\pi) = c - a_1 \tag{158}$$
$$f(\frac{3\pi}{2}) = c - b_1. \tag{159}$$

The coefficients c, a_1 and b_1 can be obtained by adding together various combinations of these equations:

$$c = \frac{f(0) + f(\frac{\pi}{2}) + f(\pi) + f(\frac{3\pi}{2})}{4} \tag{160}$$
$$a_1 = \frac{f(0) - f(\pi)}{2} \tag{161}$$
$$b_1 = \frac{f(\frac{\pi}{2}) - f(\frac{3\pi}{2})}{2} \tag{162}$$

The magnetics data was analyzed using the above procedure of Fourier analysis. Each component of the magnetic field, $B_r(r,\theta,z)$, $B_\theta(r,\theta,z)$ and $B_z(r,\theta,z)$, was expanded up to the first fourier mode in θ, the toroidal angle, just as the function f was above. Higher order modes were neglected in the approximation since the magnetic probes were distributed symmetrically at four toroidal locations and therefore higher order experimental resolution was lacking. The three components of the $m = 0$ part of the magnetic field are given by $c_r(r,z)$, $c_\theta(r,z)$ and $c_z(r,z)$. The three components of the $m = 1$ part of the magnetic field are given by $a_{1r}\cos\theta + b_{1r}\sin\theta$, $a_{1\theta}\cos\theta + b_{1\theta}\sin\theta$ and $a_{1z}\cos\theta + b_{1z}\sin\theta$.

If the plasma configuration resulting from the merger of two counter-helicity spheromaks in SSX-FRC is in Grad-Shafranov equilibrium, then it will be axisymmetric. Therefore, it is reasonable to examine the $m = 0$ component of the magnetic field, which is obtained by averaging the field over θ. Fig. 55 shows the m=0 component of the magnetic field at 62.4 μs, at which point the spheromak/FRC hybrid seems close to its equilibrium configuration. This shot had a relatively modest RCC field of 70 G on axis. Plots (a) and (b) in Fig. 55 show the projection of the magnetic field onto the $r - z$ plane at two different azimuthal angles. Plots (c), (d) and (e) in Fig. 55 show the projection of the magnetic field onto $r - \phi$ plane at three axial locations. Red arrows are 2-D projections of the field measured on one $r - z$ plane whereas blue arrows are projections of the field measured on the $r - z$ plane that is perpendicular to the first. The black arrows indicate that one of the two probes used for the particular projection was broken and interpolation was used. The green arrows indicate that a probe orthogonal to the plane of the projection was broken. (Since the probes do not point exactly in the r, θ or z direction and a calibration procedure was used to extract B_r, B_θ and B_z, the green arrows are not totally free of the influence of interpolation.) The geometrical relationships between the field points in plots (a) and (b) and those in plots (c), (d) and (e) are defined in Fig. 54. The $+z$ direction is also defined in Fig. 54. In plots (a) and (b), reversal of the magnetic field approximately two thirds of the way between the geometric axis and the flux conserver wall is evident at each probe stalk, which is consistent with a spheromak or FRC. Plot (d) shows the magnetic field measured at the midplane, where very little toroidal field exists. In the midplane region where reconnection occurs, the spheromak magnetic field is transformed to an FRC magnetic field without a toroidal component. Substantial toroidal field is present at the end planes, making those regions spheromak-like. This toroidal flux has not yet come into contact with anti-parallel flux at which point it reconnects. The toroidal field in the end planes is axially antisymmetric, as expected since the FRC is formed from two spheromaks with antiparallel toroidal fields.

There must be currents circulating around the two regions of oppositely directed toroidal fields. It follows that there is radial current at the midplane, as shown in Fig. 56. The radial current is due to the $\nabla \times \vec{B}$ due to the antiparallel toroidal magnetic fields. The toroidal magnetic fields and the associated currents are sustained after the end of the poloidal flux reconnection period, but the mechanism for the sustenance is unclear. Another issue is that the radial current must be flowing across flux surfaces, which violates a condition of Grad-Shafranov equilibrium. The current must not flow across the flux surfaces since, by Eq. 95, current is a function of flux.

The full magnetic data set at the same time as in Fig. 55 is plotted in Fig. 57. The data in Fig. 57 closely resemble those in Fig. 55, which indicates that the $m = 0$ mode dominates although other modes are present.

Approximately 1 mW of flux is added to the plasma by the stuffing flux coils during spheromak formation. However, as is evident in Fig. 58, the poloidal flux at the end planes reaches 3-4 mW immediately. This constitutes a significant magnification of the flux from the plasma gun. The midplane flux takes somewhat longer to grow, but it finally reaches a value comparable to the peak value at the end planes. Such a delay is consistent with the reconnection of the poloidal field of the two spheromaks at the midplane and the change in topology to an FRC in which the field is axially oriented at the midplane, as shown in Fig. 20. The delay in the growth of the midplane flux can be used to calculate the reconnection rate. The reconnection rate is given by the normalized quantity $\frac{\dot{\psi}}{v_A BL}$ where v_A is the Alfvèn speed and L is a charcteristic length given by $2\pi r_{null}$ where r_{null} is the radius of the magnetic null point. In this experiment, the reconnection rate is approximately 0.04. The midplane and end-plane flux all decay at about the same rate.

Due to the limitations of the magnetic probe resolution, it is not clear whether the bundles of anti-symmetric toroidal flux on the end planes are private (i.e. linked by separate poloidal flux) as in the Grad-Shafranov equilibrium with non-zero RCC field or public as in the Omelchenko results. However, the fact that the midplane poloidal flux reaches a value comparable to the peak end plane poloidal flux while antisymmetric bundles of toroidal flux persist on the end planes suggests that the regions of toroidal flux are not private. If they were, the midplane poloidal flux would be less because the poloidal field lines curve around rather than passing through the midplane.

The radial flux profiles for all three axial planes are also shown in Fig. 59. r_1 and r_2 are the radial positions of the peak flux at the end and middle planes respectively and r_s is the radial position at which the flux function vanishes, i.e. the separatrix. $\frac{r_1}{r_s} = 0.60$ and $\frac{r_2}{r_s} = 0.74$. Eqs. 141 and 121 predict that the peak flux should occur at $0.71 r_s$ for an FRC and at $0.62 r_s$ for a spheromak, which is another indication that the plasma at the midplane is FRC-like and the plasma at the end plane is spheromak-like.

The radial flux profiles can be readily compared with output from the Grad-Shafranov equilibrium solver discussed above. Fig. 60 displays the flux profile at the midplane for run 2 on 12-4-02 at 52.8 μs. There was no RCC current for this run. The figure also displays flux profiles based on the output of the solver for two cases: $\beta_p = 0.1, pexp = 1., fexp = 1.$ and $\beta_p = 0.2, pexp = 1.5, fexp = 1$. The influence of the magnetic field due to the plasma guns was included in this model. The location of the flux peak in the measured profile was estimated by mentally fitting the three points surrounding the peak to a parabola. The justification for this mental fitting procedure is that the peaks of all the simulated flux profiles appear parabolic. Furthermore, there is a region sufficiently close to any extremum that is parabolic. The full width half maximum (FWHM) of the flux profile measurement was estimated and it is indicated on the plot. Finally, the upper and lower limits of the portion of the flux profile above 0.5 were determined. These four parameters (peak location, FWHM, upper and lower limits) were compared with the corresponding values for the simulated profile for several different sets of values for the input parameters. Two of the best fits are displayed along with the data in Fig. 60. The simulated output matches the measurement reasonably well. However, the flux function is only measured at eight radial positions at each plane of probes, so there is substantial uncertainty in the four parameters used to characterize the measured flux profile.

The same procedure was used to compare three more flux profiles with simulation output. The endplane profiles corresponding to the midplane profile discussed above (run 2 on 12-4-02 at 52.8 μs) are displayed in Fig. 61. The midplane and endplane profiles for run 13 on 12-4-02 at 52.8 μs are shown in Figs. 62 and 63 respectively. In the two endplane figures (Figs. 61 and 63), the measured endplane profiles are compared with the equilibria that best fit the corresponding midplane profiles. The simulated flux peaks in the endplane figures are at a greater radial location than the flux peaks of the measured profiles. The discrepancy between measurement and simulation for the endplanes can be explained by the spheromak like character of the plasma in that region: the higher level of toroidal field at the endplanes results in a lower value of β and a lesser peak flux radius.

The purpose of fitting the flux profiles to the simulation output was to try to determine global plasma parameters such as β. When the pressure and magnetic field vary throughout the plasma (as in SSX-FRC), the pressure at the magnetic axis (peak pressure) and the magnetic field at the edge of the plasma are used to compute β. The magnetic field at the edge of the hybrid has been measured, but there are no pressure diagnostics in SSX-FRC. Therefore, we must resort to comparison of the magnetics data with simulation in order to determine β. The simulation has bp as one of its input parameters, not the physical β. The values for physical β for each of the seven cases used in the flux profile fits were calculated by Michael Schaffer of General Atomics and are displayed in the table below.

bp	pcoef	fcoef	I_{tot} [kA]	peak flux [mWb]	B_z(0,0) [T]	p(mx) [Pa]	β
0.4	1.0	1	103.2	5.01	0.169	2025	0.509
0.4	0.5	1	109.8	4.79	0.164	2338	0.588
0.2	1.5	1	111.9	5.40	0.205	911.1	0.229
0.1	1.0	1	119.5	5.46	0.218	552.5	0.139
0.1	0.5	1	121.1	5.38	0.214	705.2	0.177
0.05	2.0	1	121.8	5.58	0.228	191.2	0.048
0.05	1.0	1	122.3	5.54	0.226	279.9	0.070

The simulation inputs were chosen so that the edge field was 0.1 T for each of the seven cases. This value for the edge field agrees roughly with the measured edge field (within a factor of two.) In fact, the last magnetic probe is halfway into a hole in the flux conserver. The true edge field is approximately twice the field measured by the last magnetic probe. β was calculated by dividing the maximum plasma pressure by the magnetic pressure corresponding to 0.1 T. As displayed in the table, the value of β at the midplane ranges from 0 to 0.6. These low values are surprising considering the lack of toroidal field at the midplane. These β values indicate that the midplane region is far from the FRC regime ($\beta \approx 1.0$). However, the plasmas at the endplanes apparently have values for β that are still lower since the flux peaks occur at a lesser radius (as noted above.)

The energy density in various components of the magnetic field is shown in Fig. 64. After the formation of the spheromaks, there is a period of exponential decay of the m=0, poloidal component of the magnetic field at the end planes (which appears linear on this log plot). The exponential decay suggests that the magnetic field of the configuration is decaying resistively in this epoch. Also note that the midplane m=0 toroidal component magnetic energy remains low and the growth of the midplane m=0 poloidal component magnetic energy is delayed. These observations are consistent with the observations noted above: a lack of toroidal flux and a poloidal flux that is comparable to that of the end planes. At about 50 μs, the increase in m=0 poloidal magnetic energy at the midplane ceases, indicating that the rate of resistive decay of this component of energy has matched the growth due to reconnection (labeled "matched rates" in the figure.) At about 70 μs, the decay in toroidal and poloidal magnetic energy becomes non-exponential. The non-exponential decay occurs at the same time as a growth in the m=1 component of the energy density (labeled "begin tilt" in figure.) The simultaneity of these two processes suggests that there is a global motion of the plasma, such as a tilt instability, that transfers magnetic energy from the m=0 mode to the m=1 mode.

The sudden increase in m=1 magnetic energy shown in Fig. 64 suggests that the hybrid CT begins to tilt at about 60 μs. Therefore, it makes sense to look for a coherent plasma configuration in the m=1 component of the field after 60 μs. In fact, the m=1 component at 88 μs is consistent with that of a tilted CT (Fig. 65). The geometric axis of the CT is perpendicular to the plane of the page in plot (a) and the toroidal field of the tilted CT is visible. In plot (b), the axis of the CT is vertical in the plane of the page. The left and center probes in plot (b) show upward and downward radial field lines respectively, as one would expect if the tilted CT has some poloidal field. It is unclear why the magnetic field points towards the corner of the flux conserver in the lower right-hand corner of plot (b) and towards the center in the upper right-hand corner of plot (b). The direction of the majority of the field vectors in plots (c) and (e) are shown by the long black arrows. Note that the long black arrow in (c) has nearly the opposite direction in (e), as one would expect since the toroidal field of the tilted CT wraps around the CT's geometric axis, which is parallel to the line of red probes in plots (c)-(e).

Scans of the RCC field demonstrate that the RCC succeeds in restricting reconnection of the spheromaks. When reconnection occurs, the topology of the field lines changes. As shown in Fig.

66, the magnetic field lines go from being horizontally connected to vertically connected. In the case of the two spheromaks colliding at the center of the SSX chamber, the anti-parallel, radial fields of the spheromaks reconnect and then point along the axis of the flux conserver. The relative degree of reconnection is indicated by the relative amount of poloidal flux at the midplane. It is clear from Fig. 67 that the peak poloidal flux has an inverse relationship with the RCC field. Furthermore, the poloidal flux survives longer with a lower RCC field.

Substantial anti-parallel toroidal field exists in the end planes even without any RCC field. It is unclear why the spheromaks do not completely merge so that there is no toroidal field in the final configuration, especially considering the attractive force between the parallel currents of the two spheromaks. The degree of reconnection, as measured by the peak poloidal flux, seems to have little effect on the tilt stability of the hybrid. There is no RCC field level in which no tilt is observed.

8 Conclusion and Summary

This thesis contributes to the understanding of high-beta, slightly elongated CT equilibria. A hybrid spheromak/FRC plasma configuration was produced by merging two counterhelicity spheromaks and the magnetic structure was studied using a distributed array of magnetic probes. It was found that the midplane region of the hybrid is FRC-like (higher beta and no toroidal field) while the endplane regions are spheromak-like (lower beta and anti-parallel toroidal fields). The measured flux profiles were compared with the simulated flux profiles to try and get an idea of the plasma parameters at the midplane. The discrepancy between the radius of the peak flux at the endplanes in the measurement and the simulation indicates that the hybrid is not in Grad-Shafranov equilibrium. The existence of radial current at the midplane that flows across flux surfaces is a further violation of Grad-Shafranov equilibrium.

The results in this thesis contrast with those of Ono *et al* in that the tilt instability was observed and the toroidal field did not fully annihilate in SSX-FRC. The central conductor in the experimental apparatus of Ono *et al* may explain the lack of tilting, but the source of the discrepancy in the toroidal field observations is unclear. While the residual toroidal magnetic field indicates that the toroidal fields never fully reconnect regardless of the RCC field, the amount of reconnected poloidal field clearly decreases as the RCC field increases. The RCC field has no discernible effect on the stability of the hybrid spheromak/FRC configuration.

Future work on SSX-FRC will involve further comparison of the magnetics data with the equilibrium simulation. The code has been modified to accept different values of β in the midplane region and at the endplanes so that the hybrid spheromak/FRC character of the equilibrium can be better modeled. The code has also been modified to output magnetic vector fields so that they can be directly compared with magnetic data. Flux functions are integrated quantities, so some resolution is lost when comparing them to determine equilibrium "fits". Finally, through a collaboration with Elena Belova of Princeton Plasma Physics Laboratory, output from the equilibrium simulation is being fed into a dynamical simulator to investigate how the equilibrium evolves in time.

9 Acknowledgments

The author would like to thank those who contributed to this project. It was a privilege to benefit from the devotion and skillful guidance of my advisors, Michael Brown and Chris Cothran. Michael Schaffer contributed a great deal to my understanding of Grad-Shafranov theory and simulation.

The Grad-Shafranov solver was written by J.A. Leuer. The experiment benefited from the deft craftsmanship of Jim Haldeman and Steve Palmer. Rachel Sapiro assembled a significant fraction of the magnetic probes. Several fruitful conversations with John Boccio, Abram Falk and Matt Landreman were had. This work was financially supported by the US Department of Energy, Office of Fusion Energy Sciences.

References

[1] P. M. Bellan. From the forthcoming *Fundamentals of Plasma Physics*.

[2] P. M. Bellan. *Spheromaks*. Imperial College Press, London, 2000.

[3] E. V. Belova et al. Numerical study of global stability of oblate field-reversed configurations. *Physics of Plasmas*, 6(4):1267–1277, April 2001.

[4] W. H. Bennett. Magnetically self-focussing streams. *Physical Review*, 45:890–897, June 1934.

[5] A. Bondeson et al. Tilting instability of a cylindrical spheromak. *Phys. Fluids*, 24(9):1682–1688, September 1981.

[6] M. R. Brown. Experimental studies of magnetic reconnection. *Physics of Plasmas*, 6:1717, 1999.

[7] M. R. Brown et al. Energetic particles from three-dimensional magnetic reconnection events in the swarthmore spheromak experiment. *Physics of Plasmas*, 9:2077, 2002.

[8] M. R. Brown et al. Experimental observation of energetic ions accelerated by three-dimensional magnetic reconnection in a laboratory plasma. *Astrophysical Journal*, 577:L63, 2002.

[9] C.D. Cothran et al. Partial and complete spheromak merging at ssx: 3d studies of reconnection and frc formation. *Physics of Plasmas*, 2003. in press.

[10] S. Cowley. Unpublished lecture notes: NUF 2000 lecture.

[11] B. Dasgupta et al. Formation of a field-reversed configuration by coalescence of spheromaks. *Transactions of Fusion Technology*, 27:374–377, 1995.

[12] Y. Ono et al. Experimental investigation of three-dimensional magnetic reconnection by use of two colliding spheromaks. *Phys. Fluids B*, 5(10):3691–3701, 1993.

[13] Y. Ono et al. New relaxation of merging spheromaks to a field reversed configuration. *Nuclear Fusion*, 39(11Y):2001–2008, 1999.

[14] A. Falk. Dynamics of field-reversed configuration in ssx, 2003. Senior Honors Thesis, Swarthmore College.

[15] C. Geddes. Spheromak equilibrium studies on ssx, 1997. Senior Honors Thesis, Swarthmore College.

[16] C. G. R. Geddes et al. *Physics of Plasmas*, 5(4):1027, April 1998.

[17] E. Hameiri et al. Turbulent relaxation of compressible plasmas. *Phys. Fluids*, 25(10):1855, October 1982.

[18] J.H. Hammer. Mhd tilting modes for nearly spherical compact toroids with arbitrary plasma pressure. *Nucl. Fusion*, 21(4):488, 1981.

[19] D. W. Hewett. *Nuclear Fusion*, 24:349, 1984.

[20] R. R. Parker J. G. Cordey, R. J. Goldston. Progress toward a tokamak fusion reactor. *Physics Today*, pages 22–30, January 1992.

[21] J. D. Jackson. *Classical Electrodynamics*. John Wiley and Sons, New York, second edition, 1975.

[22] D.A. Kitson and P.K. Browning. *Plasma Phys Control Fusion*, 32:1265, 1990.

[23] S.O. Knox et al. *Phys Rev Lett*, 56(8):842, 1986.

[24] T. W. Kornack et al. Experimental observation of correlated magnetic reconnection and alfvénic ion jets. *Physical Review E*, 58:R36, 1998.

[25] M. Landreman. The three-dimensional structure of magnetic reconnection in ssx, 2003. Senior Honors Thesis, Swarthmore College.

[26] M. Landreman et al. Review of Scientific Instruments (in press).

[27] Z. W. Ma and A. Bhattacharjee. Hall magnetohydrodynamic reconnection: The Geospace Environment Modeling challenge. *Journal of Geophysical Research*, 106:3773, 2001.

[28] H.S. McLean et al. Plasma diagnostics for the sustained spheromak physics experiment. *Review of Scientific Instruments*, 72(1):556, January 2001.

[29] H.S. McLean et al. Suppression of mhd fluctuations leading to improved confinement in a gun-driven spheromak. *Physical Review Letters*, 88(12), March 2002.

[30] R. D. Milroy and J. U. Brackbill. *Phys. Fluids*, 29:1184, 1986.

[31] R. D. Milroy et al. *Phys. Fluids B*, 1:1225, 1989.

[32] Y. A. Omelchenko. Kinetic simulations of the formation and stability of the field-reversed configuration. *Physics of Plasmas*, 7(5):1443–1451, May 2000.

[33] Y. A. Omelchenko. Nonlinear stability of field-reversed configurations with self-generated toroidal field. *Physics of Plasmas*, 8(10):4463–4469, October 2001.

[34] Y. Ono. Slow formation of field-reversed configuration by use of two merging spheromaks. *Transactions of Fusion Technology*, 27:369, April 1995.

[35] P.B. Parks and M.J. Schaffer. Analytical equilibrium and interchange stability of single- and double- axis field-reversed configurations inside a cylindrical cavity. in press.

[36] M. N. Rosenbluth and M. N. Bussac. *Nuclear Fusion*, 19:489, 1979.

[37] M. J. Schaffer. Exponential taylor states in circular cylinders. *Phys. Fluids*, 30(1):160, January 1987.

[38] M. J. Schaffer. Advances in novel frc plasmas. In *Proceedings, U.S./Japan Workshop on Physics of Compact Toroid Plasmas*, February 2002.

[39] M.A. Shay et al. Alfvenic collisionless magnetic reconnection and the hall term. *JOURNAL OF GEOPHYSICAL RESEARCH*, 106(A3):3759, March 2001.

[40] L.C. Steinhauer and A. Ishida. Relaxation of a two-specie magnetofluid. *Physical Review Letters*, 79(18):3423, November 1997.

[41] P. A. Sturrock. *Plasma Physics*. Cambridge University Press, Cambridge, 1994.

[42] M. Tuszewski et al. Observations of tilt instabilities in field-reversed configurations of a confined plasma. *Physical Review Letters*, 66(6):711–714, February 1991.

[43] M. Tuszewski and B.L. Wright. Observation of field-reversed configurations with spheromak magnetic field profiles. *Physical Review Letters*, 63(20):2236, November 1989.

[44] M. G. Tuszewski. Field-reversed configurations without toroidal field. *Nuclear Fusion*, 28(11):2033–2092, November 1988.

[45] T.-H. Watanabe. Magnetohydrodynamic simulation on co- and counter-helicity merging of spheromaks and driven magnetic reconnection. *Physics of Plasmas*, 4(5):1297, May 1997.

[46] M. Yamada et al. Magnetic reconnection of plasma toroids with cohelicity and counterhelicity. *Physical Review Letters*, 65(6):721–724, 1990.

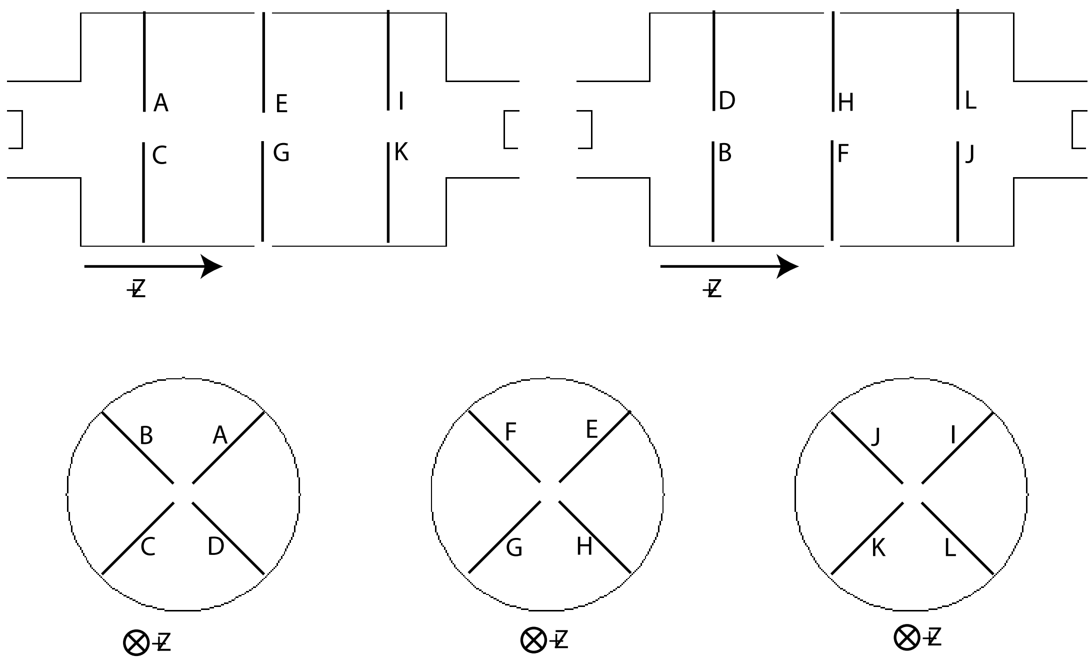

Figure 54: The figure above defines the $+\hat{z}$ direction in subsequent plots of magnetic field vectors. The correspondence between probe stalks in the side view (top) and axial view (bottom) is also displayed.

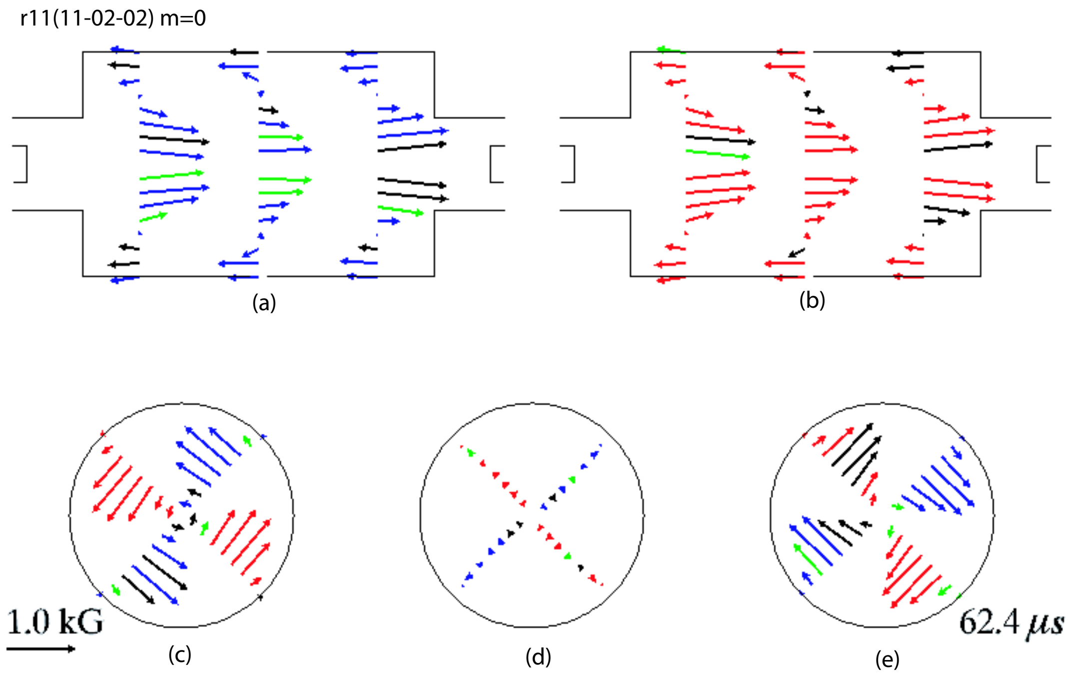

Figure 55: The symmetric component of the magnetic field is projected onto different planes in this figure. The poloidal field of an FRC is evident in plots (a) and (b). The residual antiparallel toroidal fields are shown in plots (c) and (d). There is little residual toroidal field at the midplane [plot (d)].

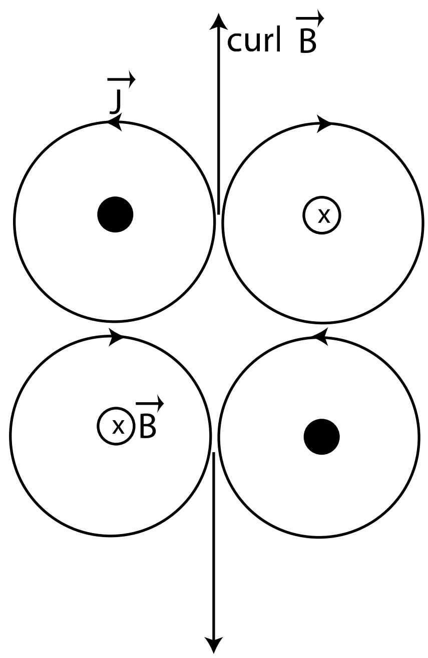

Figure 56: The circulating current gives rise to the oppositely directed toroidal fields. The curl in $\vec{B}$ due to oppositely directed toroidals field gives rise to the radial current at the midplane.

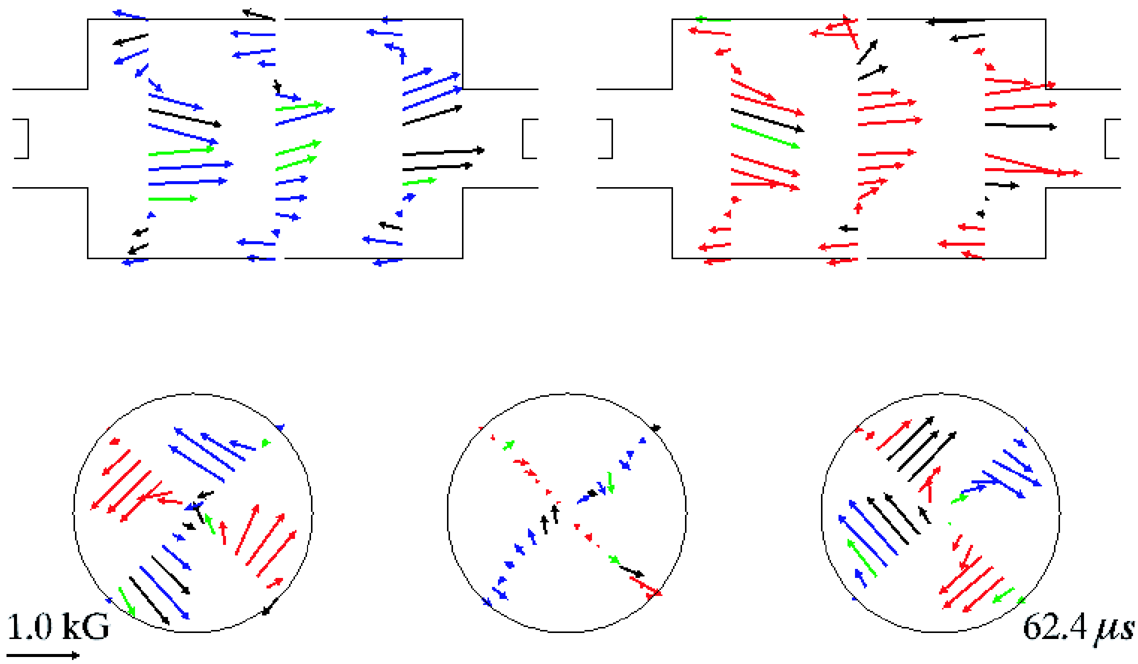

Figure 57: The full magnetic field is projected onto different planes in the figure above. Comparison with the symmetric (m=0) component of the field shows that the total magnetic field is dominated by the symmetric component.

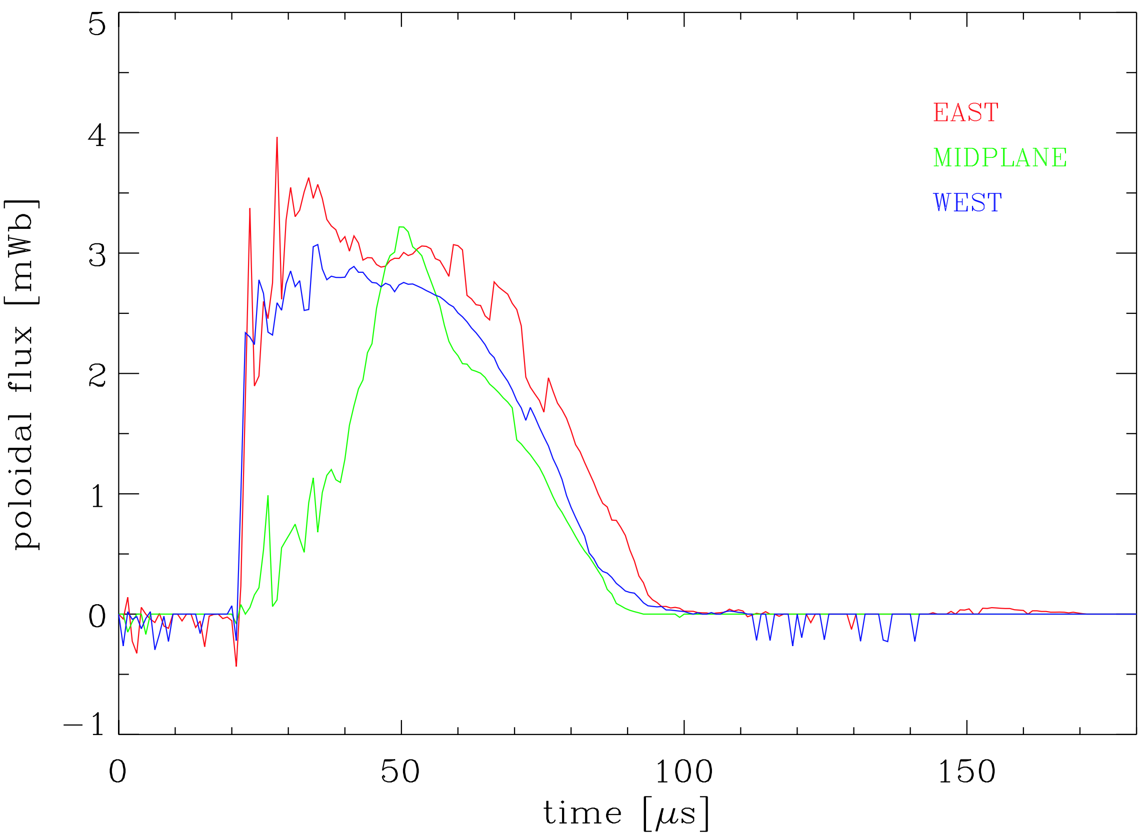

Figure 58: The poloidal flux as a function of time at the three planes where the magnetic field was measured. There is a delay in the growth of the midplane flux compared with the growth of the east and west plane flux. There is a significant magnification in the flux from the plasma gun.

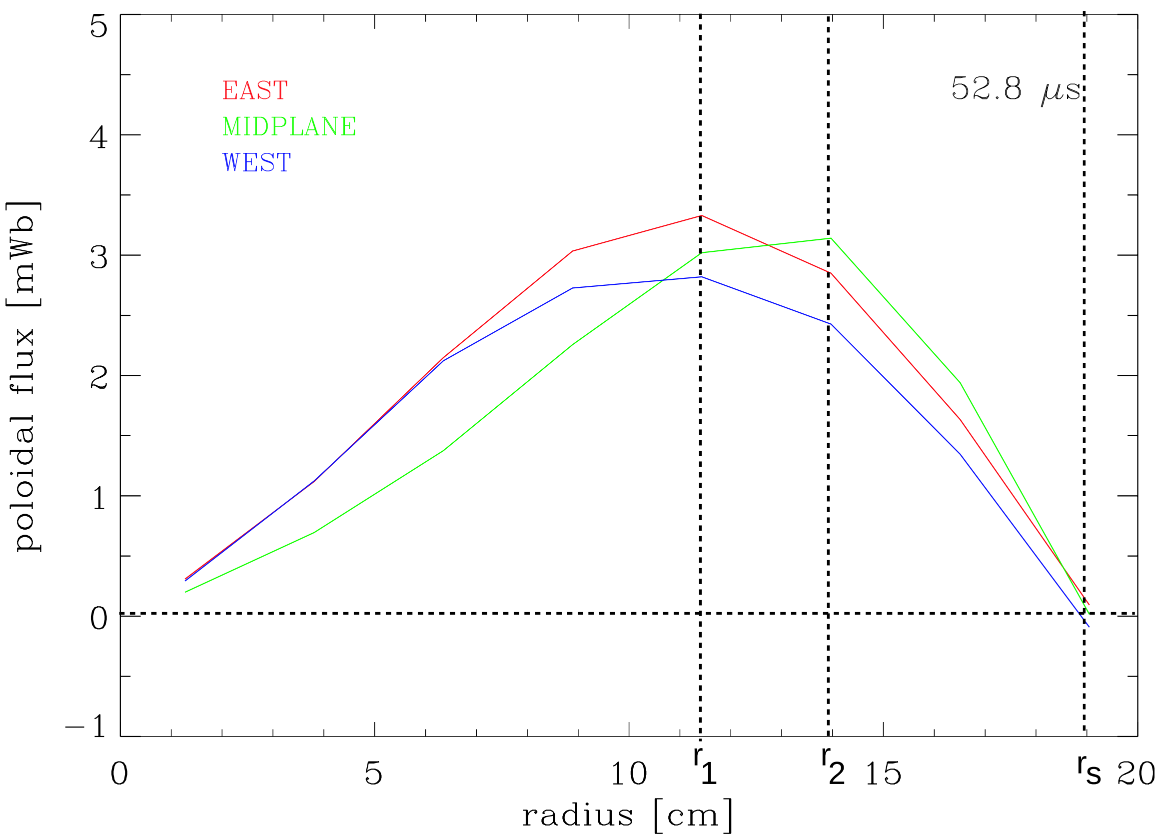

Figure 59: The flux functions are plotted as a function of radius at the three planes where the magnetic field was measured. The East and West flux peaks are at a lesser radius compared with the radius of the midplane flux peak, which indicates that the East and West regions are spheromak like whereas the midplane region is FRC like.

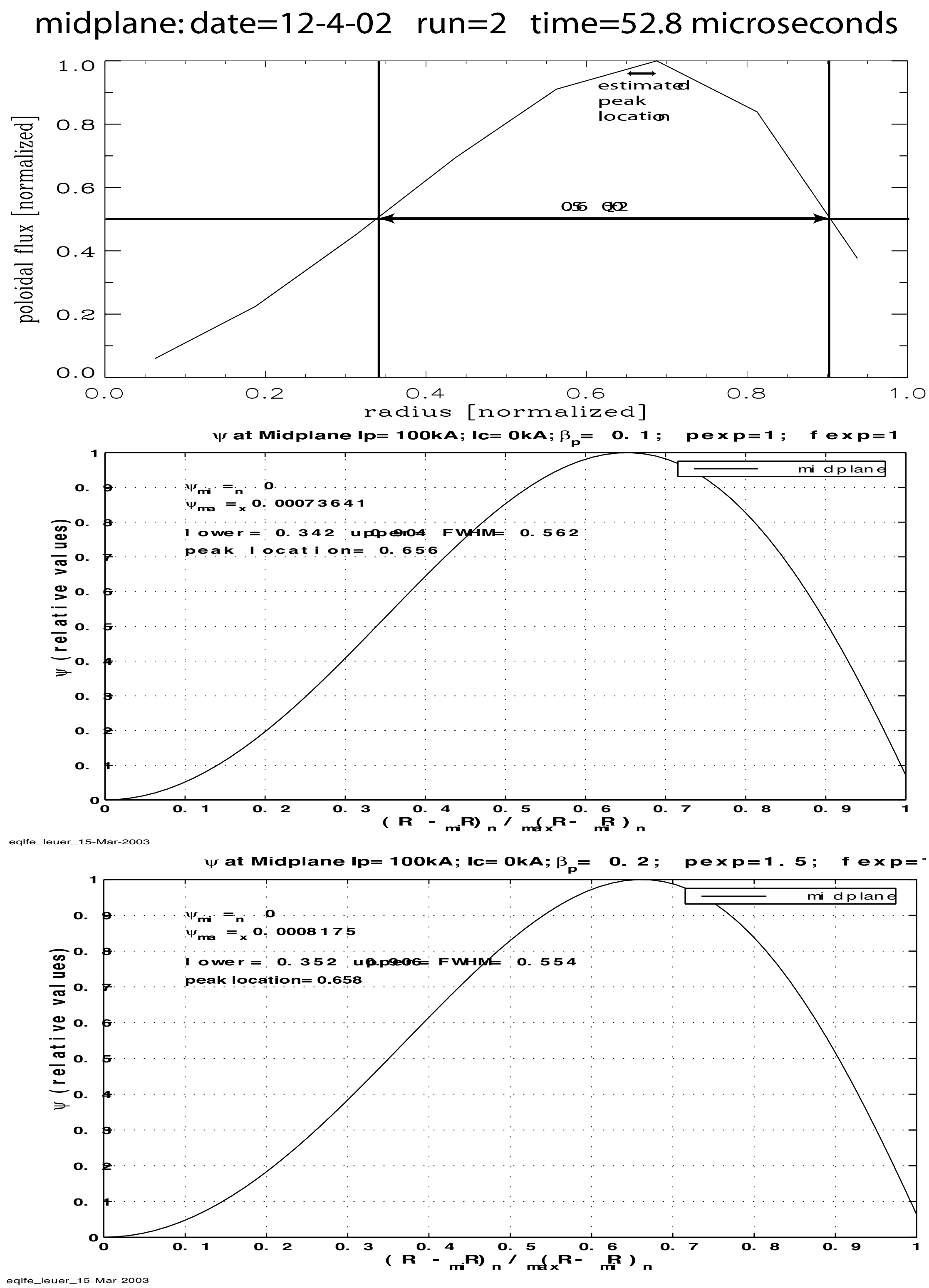

Figure 60: A comparison between measured and simulated midplane flux profiles for the plasma in its hybrid equilibrium configuration. The simulation cases were chosen to best fit the locations of the peak flux and the FWHM for the experimental measurement.

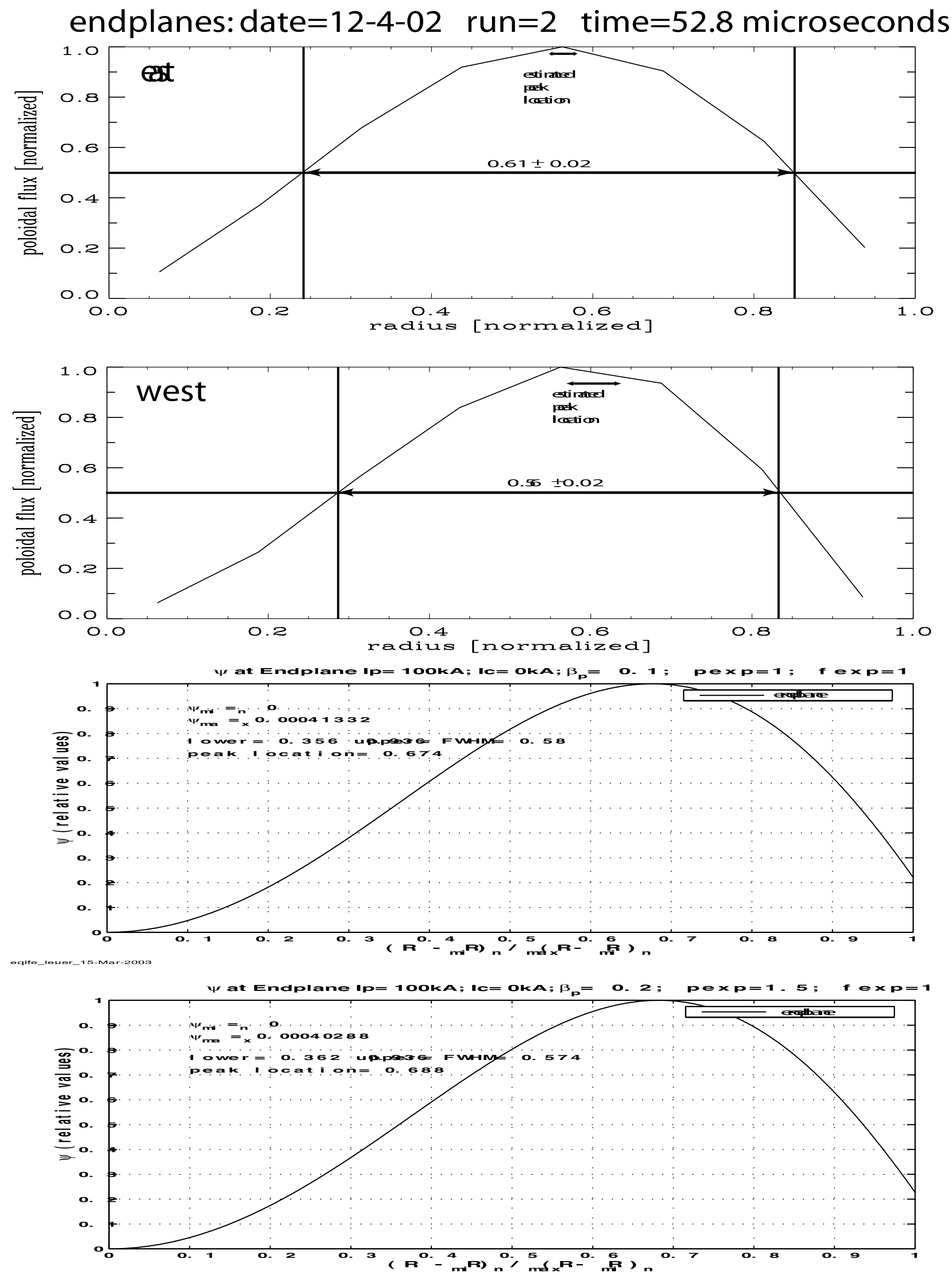

Figure 61: A comparison between measured and simulated East and West flux profiles for the plasma in its hybrid equilibrium configuration. The simulation cases are the same as those that best fit the midplane profiles in the previous figures. The simulation profiles displayed in this figure are in fact calculated at the location of the East and West probe planes.

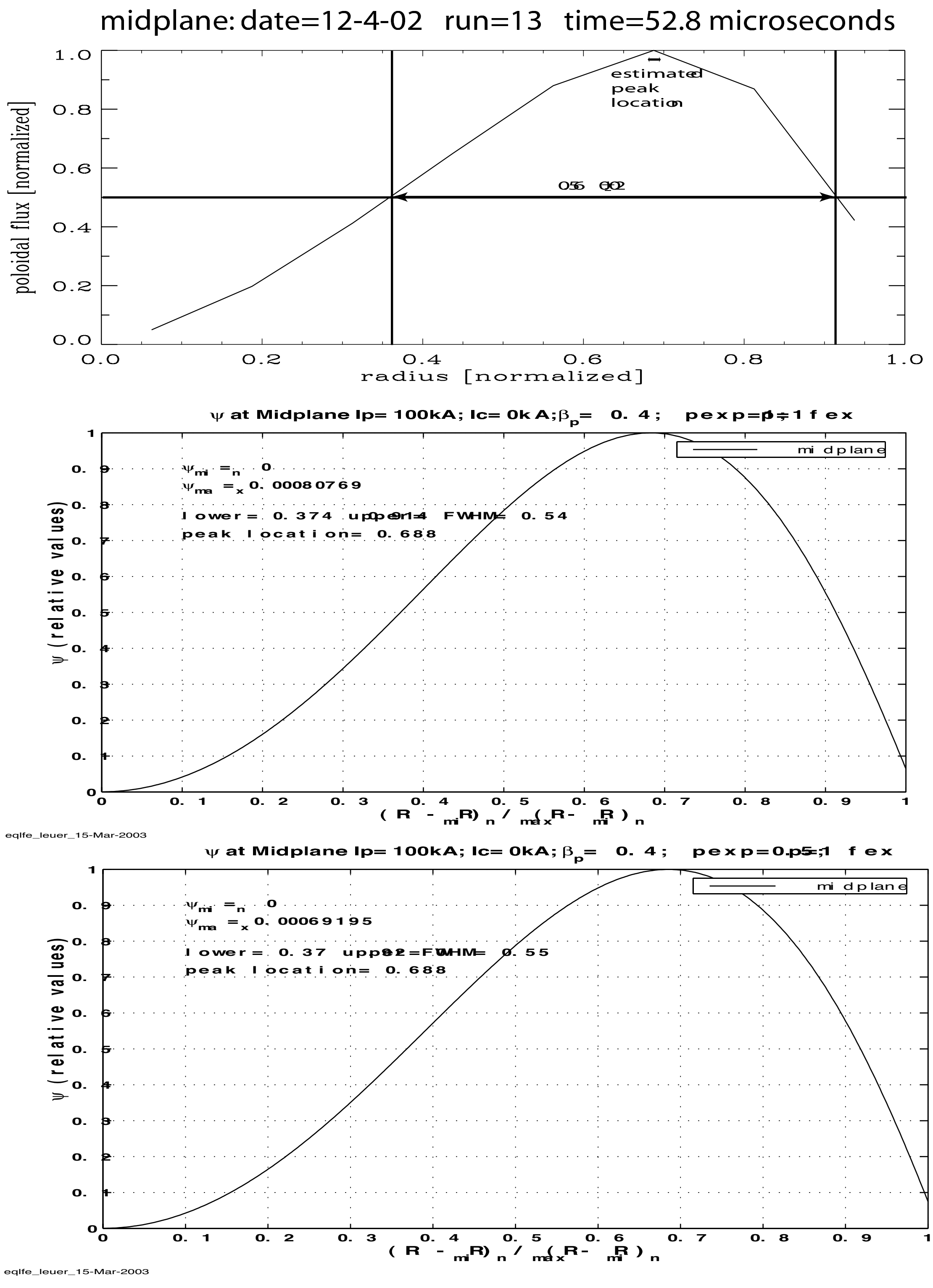

Figure 62: A comparison between measured and simulated midplane flux profiles for the plasma in its hybrid equilibrium configuration. The simulation cases were chosen to best fit the locations of the peak flux and the FWHM for the experimental measurement.

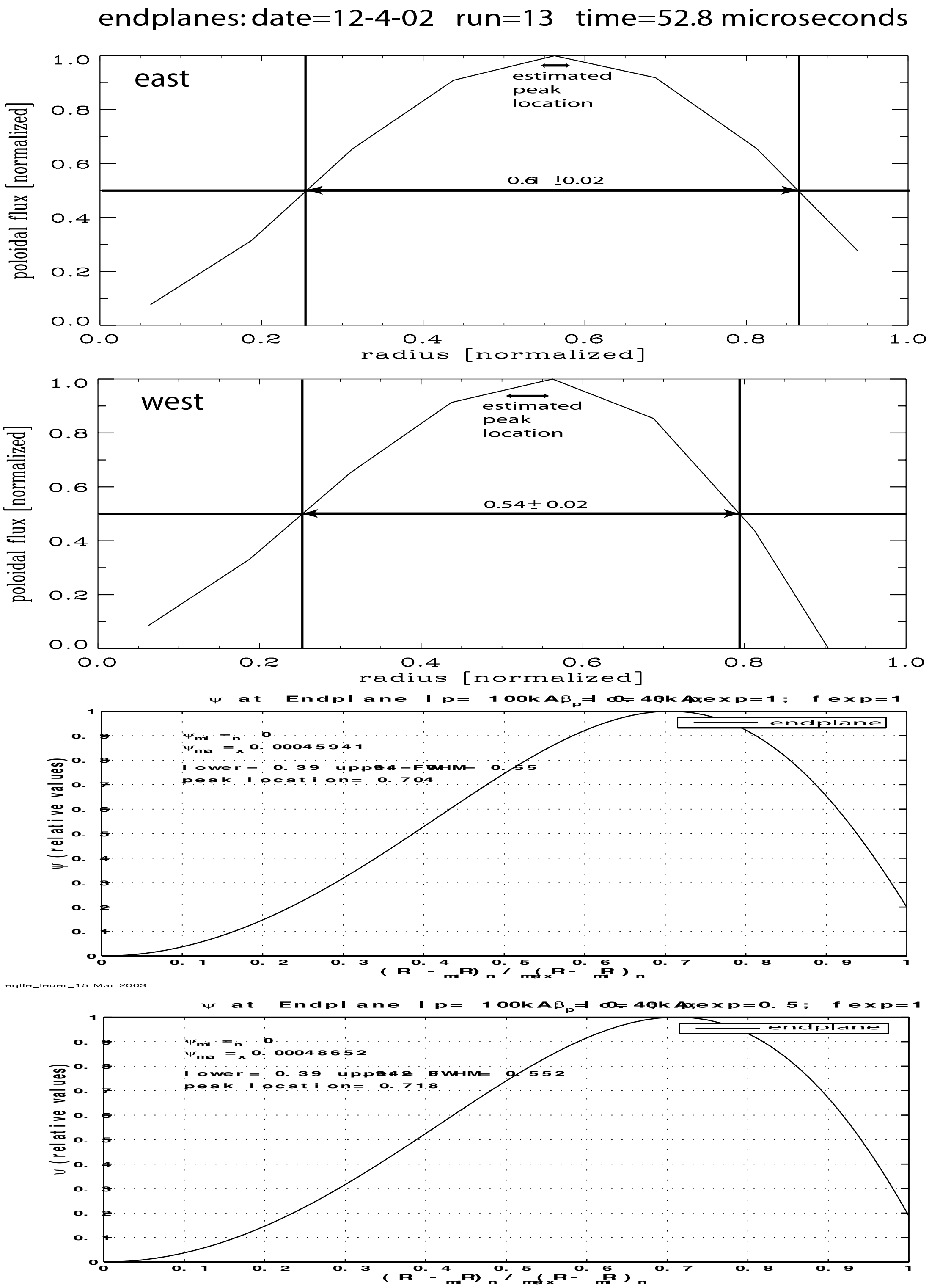

Figure 63: A comparison between measured and simulated East and West flux profiles for the plasma in its hybrid equilibrium configuration. The simulation cases are the same as those that best fit the midplane profiles in the previous figures. The simulation profiles displayed in this figure are in fact calculated at the location of the East and West probe planes.

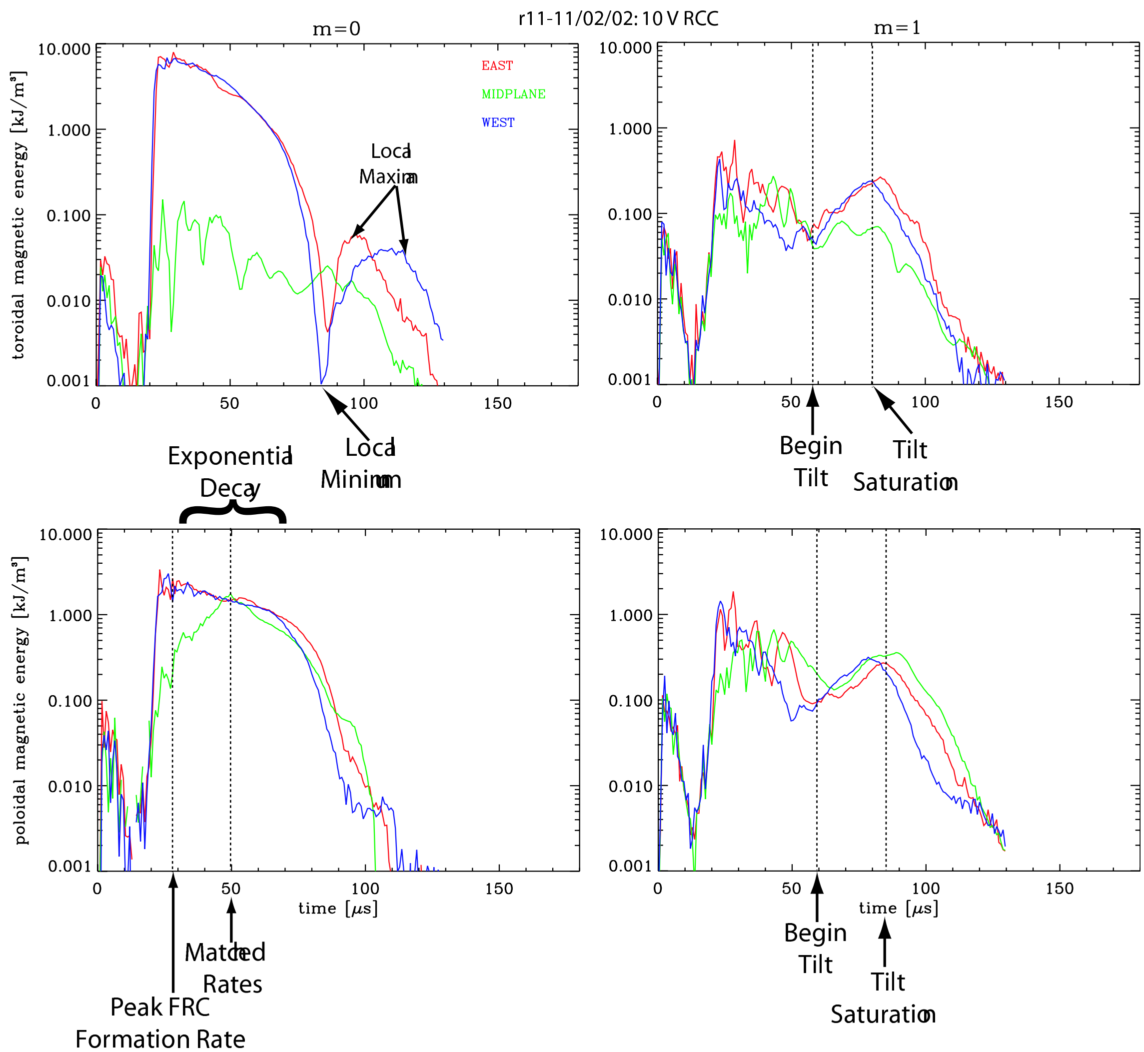

Figure 64: Various components of the magnetic energy density at each of the three planes where the field was measured are plotted as functions of time above. Various epochs in the evolution of the spheromak/FRC hybrid are indicated.

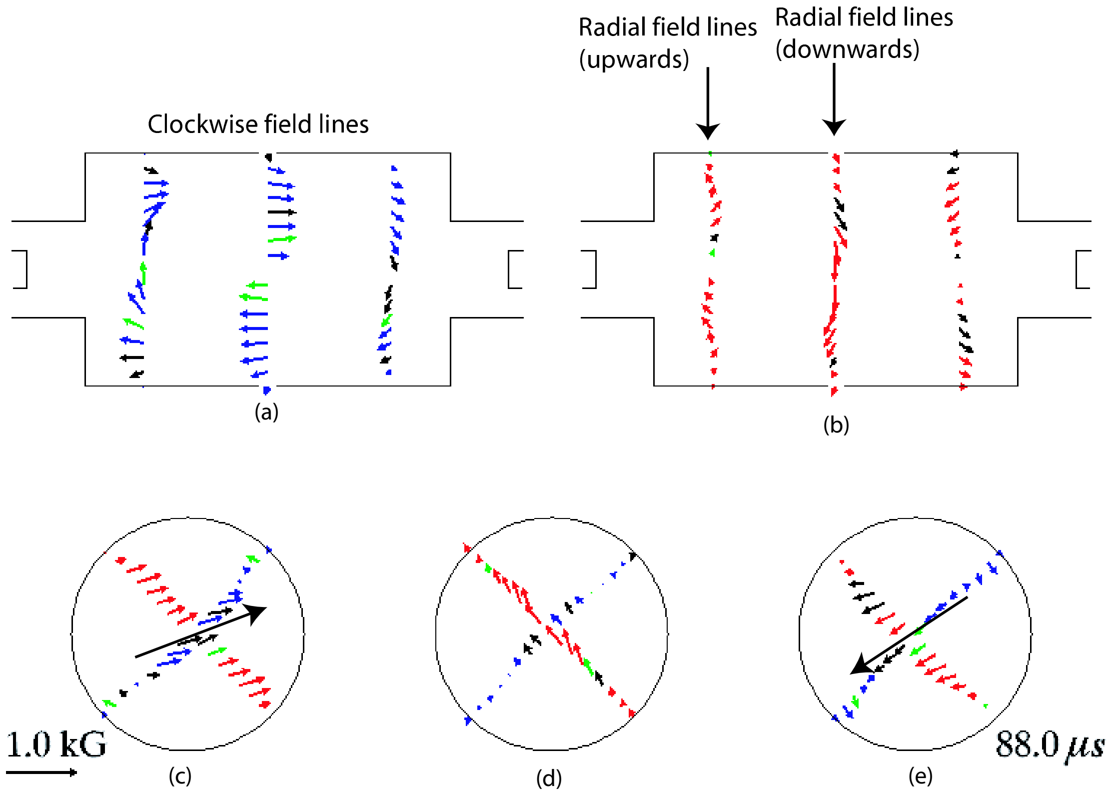

Figure 65: The anti-symmetric (m=1) component of the magnetic field is plotted above. The field is consistent with that of a tilted CT. The long black arrows in plots (c) and (e) indicated the general direction of the magnetic field vector projections in those plots.

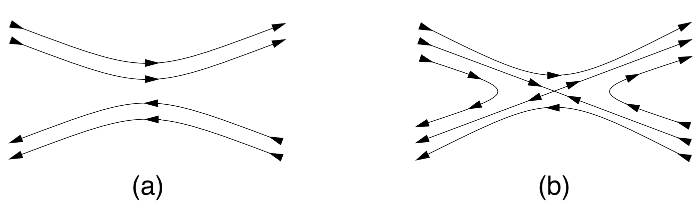

Figure 66: The change in the topology of magnetic field lines due to reconnection.

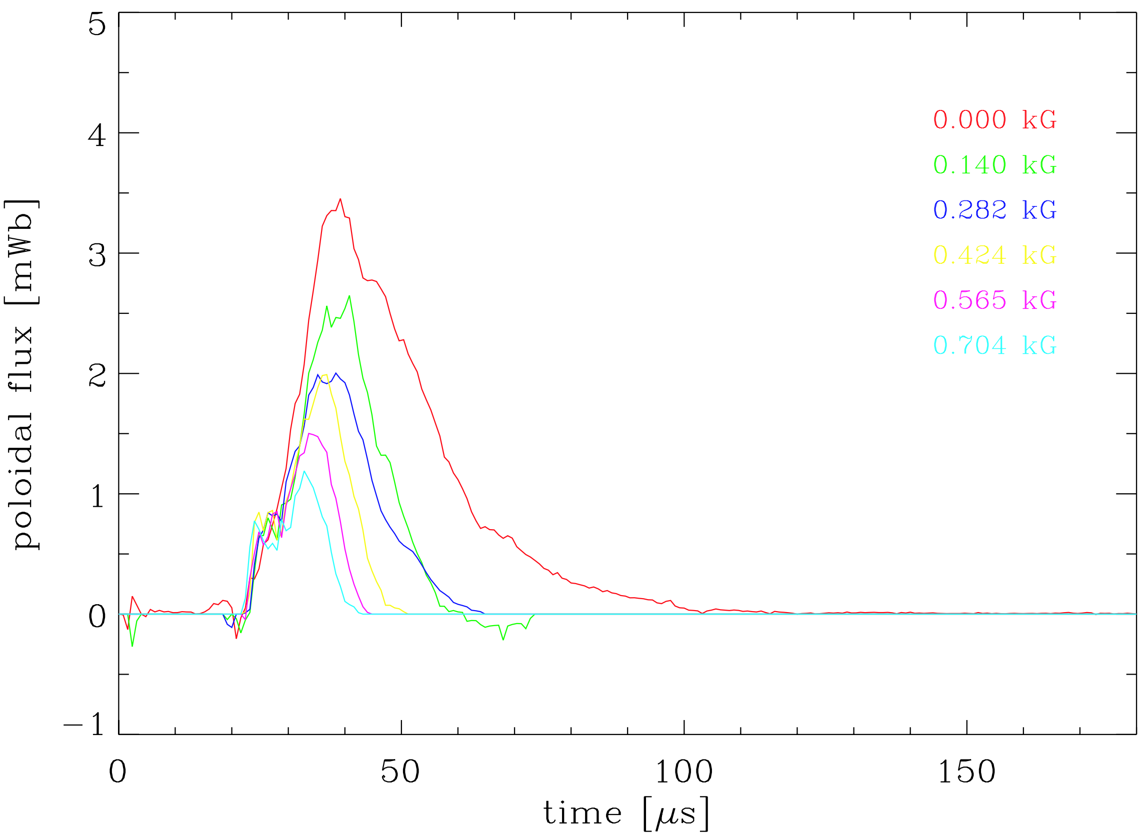

Figure 67: Plots of the peak poloidal flux for various values of the external magnetic field imposed by the reconnection control coil. The external field limits the peak poloidal flux because it limits the extent to which the two colliding spheromaks merge.